

A CHEMOPROTEOMIC TECHNIQUE FOR THE IDENTIFICATION OF
PROTEINS REGULATED BY COENZYME A

A Dissertation

Presented to the Faculty of the Graduate School
of Cornell University

In Partial Fulfillment of the Requirements for the Degree of
Doctor of Philosophy

by

Ornella Daisha Nelson

December 2018

© 2018 Ornella Daisha Nelson

A CHEMOPROTEOMIC TECHNIQUE FOR THE IDENTIFICATION OF PROTEINS REGULATED BY COENZYME A

Ornella Daisha Nelson, Ph.D.

Cornell University 2018

Coenzyme A (CoA) is found in all living organisms and is involved in numerous cellular biochemical reactions. CoA and its derivatives function as cofactors in many cellular pathways and are involved in protein regulation through post-translational modifications as well as competitive and allosteric interactions. Deregulation of CoA has implications in various human diseases including cancer, diabetes and neurodegeneration.

Given the importance of CoA, I synthesized a biotin-tagged CoA probe to identify CoA-binding proteins. Interestingly, my chemical proteomic approach identified several metabolic enzymes that are not known to utilize CoA. I biochemically validated the top hit, mitochondrial malic enzyme 2 (ME2), as a CoA-binding protein.

ME2 is a NAD(P)-dependent enzyme that converts malate to pyruvate and at the same time generates NAD(P)H. ME2 plays an important role in numerous cellular processes including: proliferation, insulin secretion, senescence, glutamine metabolism and reactive oxygen species (ROS) homeostasis. I found that ME2 binds CoA tightly and, through mutation studies, identified the CoA-binding site of ME2. By screening various CoA species, I discovered a specific CoA molecule can dramatically increase ME2 enzymatic activity. Furthermore, I determined that the identified CoA molecule promotes ME2 tetramer formation and may have a role in relieving oxidative stress.

This work demonstrates that cofactor-based chemical proteomic strategies work well to identify novel protein interactions. Expansion of this technique may prove useful in better understanding cellular regulation.

BIOGRAPHICAL SKETCH

Ornella Daisha Nelson is originally from the twin island Republic of Trinidad and Tobago. Her interest in Chemistry began in high school at San Juan Government Secondary School, Trinidad. In 2012, she earned a Bachelor of Science degree in Chemistry from Cameron University in Lawton, Oklahoma. While there, she worked under the guidance of Dr. E. Ann Nalley synthesizing dyes for solar cell testing. She also participated in two National Science Foundation Research Experiences for Undergraduates at the University of California, Irvine and Pennsylvania State University. She joined the Department of Chemistry and Chemical Biology at Cornell University in August 2012 working in Dr. Hening Lin's group. She was awarded the Chemistry Biology Interface Grant in 2013, which was funded by the National Institute of Health (NIH), and the Provost Diversity Fellowship in 2018. She won the Chemistry Department Bauer Award in 2016 and was inducted into the Edward A. Bouchet Graduate Honor Society in 2017. Her thesis entitled "A Chemoproteomic Technique for the Identification of Proteins Regulated by Coenzyme A" was supervised by Dr. Hening Lin.

Dedicated to
my parents,
Susan Jerome-Nelson and Fitzroy Nelson, Jr.
AND
my grandparents,
Sheila Jerome 08/1943 - 04/2018
Vashti Nelson 04/1923 - 06/1999
Fitzroy Nelson, Sr. 06/1926 - 05/2011

ACKNOWLEDGMENTS

First, I would like to thank my advisor, Dr. Hening Lin for the amazing opportunity to work in his lab. I thank him for helping me become a better scientist. I am grateful for his guidance and advice over the years. I also appreciate the wide range of projects he has allowed me to work on; these skills and techniques will be invaluable as I move forward in my career. I also thank my committee members, Professor Yimon Aye and Professor Brian Crane for their helpful suggestions.

I thank all my fellow Lin lab members, past and present, for their countless scientific discussion and suggestions. A special thank you to Dr. Sushabhan Sadhukhan, who taught me mammalian cell culture techniques and frequently gave me research advice. Thank you to Dr. Zhewang Lin and Dr. Zhi Li for teaching me cloning and protein purification.

I thank Sara Xayarath Hernandez, Anitra M. Douglas-McCarthy and Alyssa Lopez from the Office of Inclusion and Student Engagement (OISE) for their commitment to diversity, inclusion and the creation of safe spaces for graduate students. I also thank Anitra for allowing me to be a Graduate Student Ambassador. Thank you to all my Cornell friends who became like family, you know who you are! A special thank you to my CaribbIthacan family for making Ithaca NY, feel like home.

I thank Dr. E. Ann Nally for being an amazing mentor at Cameron University, Lawton, OK. I thank all my teachers in Trinidad, especially my Chemistry teachers, Opal Hem-Lee and Lucretia Gabriel, for inspiring me to pursue Chemistry.

Lastly, I owe my greatest amount of gratitude to my amazing family. I thank you for all your love, support and encouragement. I love each of you so much! Thank you for being on this journey with me, I could not have gotten here without you.

TABLE OF CONTENTS

	Page
Biographical sketch	v
Dedication	vi
Acknowledgements	vii
Table of Contents	viii
List of Figures	xi
List of Tables	xiii
Chapter 1: Introduction	
Coenzyme A	1
The mitochondrial NAD-dependent malic enzyme	6
References	9
Chapter 2: A Chemoproteomic Approach Identifies Malic Enzyme 2 as a Coenzyme A-disulfide regulated protein	
Abstract	12
Introduction	13
Results	14
Discussion	26
Methods and Materials	27
References	39
Chapter 3: Conclusions and Future Directions	
Conclusions	41

Future Directions	42
References	44
Appendix A: Preliminary Investigation of other enzymes identified in Biotin-Coenzyme A Proteomics	
Introduction	45
Results	46
Discussion	49
Methods and Materials	49
References	52
Appendix B: Metabolomics-assisted proteomics identifies SIRT5 as an important regulator of heart function	
Abstract	53
Introduction	54
Results	56
Discussion	76
Methods and Materials	79
References	96
Appendix C: Identification of proteins capable of metal reduction from the proteome of the Gram-positive bacterium <i>Desulfotomaculum reducens</i> MI-1 using an NADH-based activity assay	
Abstract	99
Introduction	100

Results	102
Discussion	120
Methods and Materials	126
References	137
Permission for reproduction	140

LIST OF FIGURES

1.1	Structure of CoA and two CoA derivative, acetyl-CoA and succinyl-CoA	1
1.2	<i>de novo</i> CoA biosynthesis	2
1.3	The enzymatic reaction and structure of ME2	8
2.1	Biotin-CoA Synthesis	15
2.2	A chemical proteomic approach identified ME2 as a potential Coenzyme A-binding protein	18
2.3	ME2 binds CoA-SH in vitro	19
2.4	ME2 is allosterically activated by CoA-S-S-CoA in vitro	22
2.5	Mechanism by which CoA-S-S-CoA allosterically activates ME2	23
2.6	Proposed model of allosteric activation of ME2 by CoA-S-S-CoA to relieve oxidative stress	26
A.1	Histogram showing the percentage of CoA-SH binding to NME1, NME2, and NME4	47
A.2	Histogram showing relative NME activity with and without CoA molecules	48
A.3	Histogram showing relative activity of PK/LDH with and without succinyl-CoA	48
B.1	Protein lysine succinylation occurs to the greatest extent in the heart	56
B.2	Concentration of succinyl-CoA in mouse hearts from WT and <i>Sirt5</i> KO animals	58
B.3	SIRT5 Western blot for different tissue lysates from <i>Sirt5</i> WT mouse tissues showing that the heart has the highest amount of SIRT5	59
B.4	Workflow of the dimethyl-labeling strategy for the succinylome analysis	61
B.5	Lack of SIRT5 leads to hypersuccinylation on ECHA	63

B.6	SIRT5 increases ECHA activity by desuccinylation	65
B.7	Recombinant ECHA and ECHB complex was nonenzymatically acetylated with 0.5 mM acetic anhydride for 15 min at room temperature	66
B.8	SIRT5 deficiency leads to accumulation of long-chain CoAs and decreased cardiac ATP levels	69
B.9	Relative level of long-chain CoA thioesters in <i>Sirt5</i> KO hearts compared with WT after 24 hr of fasting	70
B.10	SIRT5 deficiency causes hypertrophic cardiomyopathy	73
B.11	Body weight of <i>Sirt5</i> WT and KO male mice (8-week-old males)	74
B.12	Body weight of <i>Sirt5</i> WT and KO male mice (39-week-old males)	75
C.1	Workflow implemented to identify iron reduction candidate proteins in <i>D. reducens</i>	103
C.2	Fe(III) reduction by <i>D. reducens</i> cell suspensions grown on sulfate reduction	104
C.3	Identification of iron reduction activity in the soluble proteome of <i>D. reducens</i> .	107
C.4	Identification of iron reduction activity in the insoluble proteome of <i>D. reducens</i>	111
C.5	Purification and Characterization of Dred_2421	113
C.6	Iron reduction by Dred_2421	114
C.7	Iron reduction by Dred_1685–1686 complex	116
C.8	Co-expression and purification of Dred_1685 and Dred_1686	117
C.9	Cr(VI) reduction by Dred_2421 and Dred_1685–1686 complex	119
C.10	U(VI) reduction by Dred_2421 and Dred_1685–1686 complex	119
C.11	Reoxidation of reduced U(VI) provides evidence for U(VI) reduction	120

LIST OF TABLES

2.1	SILAC Sample#1 Results	16
2.2	SILAC Sample#2 Results	17
2.3	Detection of CoA-S-S-CoA and CoA-SH in A549 cell lysate	24
2.4	Detection of CoA-S-S-CoA and CoA-SH in control and ME2 KD A549 cell lysates	25
2.5	Detection of CoA-S-S-CoA and CoA-SH in mitochondria isolated from control and ME2 KD A549 cells	25
A.1	List of nucleoside-diphosphate kinases identified in the biotin-CoA proteomics and their corresponding heavy/light ratios	46
C.1	Recovery of iron reduction activity in protein fractions	105
C.2	Proteins identified from excised iron-reduction active gel bands	109
C.3	Iron reduction activity in heterologously expressed proteins	114

phosphopantetheine. In mammals, the fourth and fifth steps are catalyzed by one enzyme, CoA synthase, which has both phosphopantetheine adenylyltransferase and dephospho-CoA kinase activity to form CoA. In bacteria however, the second and third steps are catalyzed by one enzyme, while the fourth and fifth steps are done by two separate enzymes¹. Overall, the *de novo* biosynthesis of CoA requires four equivalents of adenosine triphosphate (ATP), one of which provides the adenosine monophosphate (AMP) structure in CoA (**Figure 1.2**).

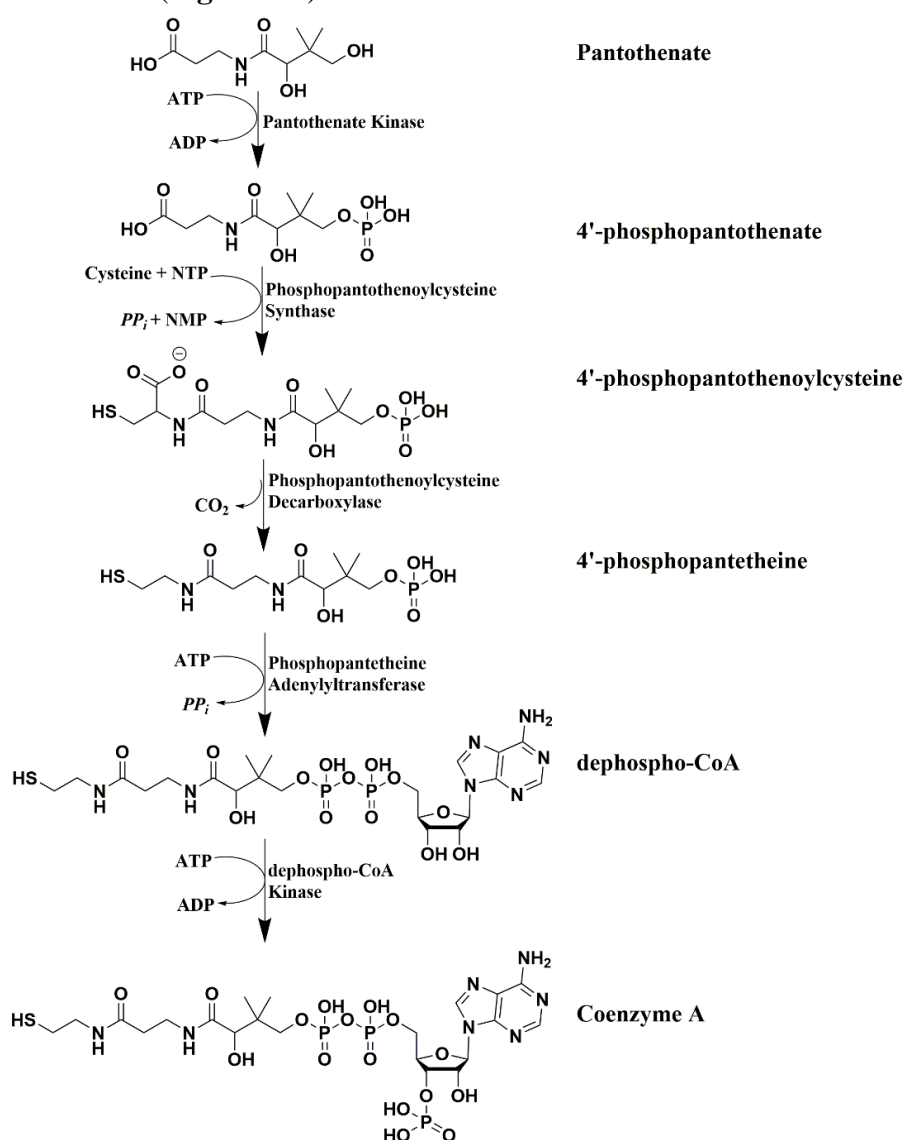


Figure 1.2 *de novo* CoA biosynthesis

Recently, in addition to *de novo* biosynthesis, alternative strategies for obtaining CoA have been reported. Impaired CoA biosynthesis through pantothenate kinase depletion in *Drosophila melanogaster* S2 cells led to reduced intracellular CoA levels and decreased protein acetylation^{4,5}. These observed reductions were alleviated by the addition of CoA to culture media^{4,5}. Extracellular ectonucleotide pyrophosphatases (ENPPs) cleave the external CoA into 4'-phosphopantetheine and 3',5'-ADP. This 4'-phosphopantetheine is stable in media and crosses the cell membrane for subsequent CoA biosynthesis⁵. This mechanism was also observed in cultured mammalian cells, including mouse and human cells⁵.

Pantothenate kinase depletion is a model for investigating neurodegenerative disease^{4,5}. Mutations in one isoform of the human pantothenate kinase (PANK2) causes a type of hereditary disease called Neurodegeneration with Brain Iron Accumulation (NBIA)⁶. Recently, mutations in the human CoA synthase (COASY), the last step of *de novo* CoA biosynthesis, have also been linked to NBIA⁷. These diseases are referred to as pantothenate kinase-associated neurodegeneration (PKAN) and COASY protein-associated neurodegeneration (CoPAN) respectively. Individuals with NBIA develop progressive speech, movement and cognitive impairments⁸.

CoA is needed in many metabolic pathways. The first step of the tricarboxylic acid (TCA) cycle, catalyzed by citrate synthase, involves the condensation of oxaloacetate and acetyl-CoA to form citrate. Two other enzymes in the TCA cycle utilize CoA for catalysis, therefore contributing to the generation of chemical energy for cellular function. The β -oxidation pathway is another example where CoA is essential. CoA can also regulate some enzymes through allosteric or competitive binding. The

mitochondrial enzyme pyruvate carboxylase, which supplies oxaloacetate to the TCA cycle through carboxylation of pyruvate, is allosterically activated by acetyl-CoA⁹. As mentioned earlier, CoA can regulate pantothenate kinase through feedback inhibition, which is an example of competitive binding inhibition. CoA was also shown to directly bind and activate calcium/calmodulin-dependent protein kinase II (CaMKII), a serine/threonine kinase involved in many signaling cascades, resulting in apoptosis inhibition in frog and mouse oocytes¹⁰.

CoA is required for the synthesis of acetyl-CoA, which in turn is used by acetyltransferases as the acyl group donor for site specific lysine acetylation of proteins. Histone acetyltransferases (HATs) have been well documented in literature. The GNAT and P300/CBP HATs protein families play important roles in chromatin structure regulation as well as localization and stability of their non-nuclear protein substrates^{11,12}. Recently, mitochondrial acetyltransferases have also been reported^{13,14}. The mitochondrial acetyl-CoA acetyltransferase (ACAT1), which is involved in the ketogenesis pathway, was identified to regulate two components of the pyruvate dehydrogenase complex: pyruvate dehydrogenase E1 component α -subunit (PDHA1) and pyruvate dehydrogenase phosphatase catalytic subunit 1 (PDP1)¹⁴. ACAT1 acetylates PDHA1 and PDP1 to inhibit both enzymes¹⁴. Non-enzymatic lysine acetylation has also been proposed as a mechanism for modifying mitochondrial proteins¹⁵.

The levels and ratios of CoA and its derivatives are affected by various cellular factors such as: nutrient availability, gene expression, intracellular metabolite concentrations and other stresses¹⁶⁻²⁰. Glucose availability regulates acetyl-CoA and the

ratio of acetyl-CoA/CoA. Under high glucose conditions, acetyl-CoA concentration and NADH/NAD ratio increase leading to high protein acetylation^{16,18,19}. However, under low glucose the NADH/NAD ratio decreases which leads to higher NAD-dependent deacetylase activity, resulting in low acetylation level on proteins^{18,19}. Another source of acetyl-CoA is the β -oxidation of fatty acids in the mitochondria. Acetyl-CoA metabolism is therefore a key determinant of histone acetylation levels²¹.

Succinyl-CoA is another important intracellular metabolite. Targeted metabolomics in various mouse tissues revealed that succinyl-CoA is the most abundant acyl-CoA in the heart²². Comparative analysis of mouse tissues indicated that SIRT5-deficient heart tissue had the highest level of lysine succinylation²². SIRT5 is the NAD-dependent protein deacetylase that removes lysine succinylation from substrate proteins²³. SIRT5-deficient mice were also found to have impaired cardiac function due to hypersuccinylation of key metabolic enzymes²². Overall, lysine succinylation was established as a regulator of metabolism and heart function. Therefore, succinyl-CoA is also an important regulator in these processes. Lysine succinylation has also been reported on histones, and a histone succinyltransferase was recently identified²⁴. These and other examples indicate how CoA and its derivatives are important for cellular function.

Cofactor-based affinity probes may be a useful tool for identifying and analyzing cellular mechanisms²⁵. For example, all known acyltransferases require acyl-CoA molecules as the donors for acyl-group transfer reactions. Lysine-CoA and peptide-CoA conjugates are acetyltransferase inhibitors that have been used to capture and identify potential acetyltransferases by mass spectrometry²⁶⁻²⁸. A similar technique could be

applied to identify CoA-binding proteins, with the anticipation that some CoA-binding proteins could be candidate protein lysine acyltransferases. This thesis explores a chemoproteomic technique for identifying CoA-binding proteins and examines a novel CoA regulated enzyme.

1.2 The mitochondrial NAD-dependent malic enzyme

The family of malic enzymes catalyze the oxidative decarboxylation of L-malate to pyruvate using the cofactor NAD or NADP (**Fig. 1.3A**)²⁹. The enzyme family requires the presence of a divalent cation such as magnesium (Mg^{2+}) or manganese (Mn^{2+}) and the reaction occurs in two steps. First, L-malate is converted to oxaloacetate and then the decarboxylation of oxaloacetate produces pyruvate and carbon dioxide³⁰. Malic enzymes are highly conserved and play important roles in many organisms³¹⁻³³.

In mammals, there are three isoforms of malic enzyme: the cytosolic NADP-dependent malic enzyme (ME1), the mitochondrial NAD-dependent malic enzyme (ME2) and the mitochondrial NADP-dependent malic enzyme (ME3)³⁴. Interestingly, ME2 is the only isoform that can use both NAD and NADP for catalysis (**Fig. 1.3B**). ME2 is implicated in numerous cellular processes including: proliferation, insulin secretion, senescence, glutamine metabolism and reactive oxygen species (ROS) homeostasis^{33,35-39}. The knockdown of ME2 induces cellular senescence where cells can no longer divide³⁵. Depletion of ME2 decreases the cellular NADPH levels, resulting in elevated ROS levels and activation of the tumor suppressor p53, which can lead to cell death^{35,36}. ME2 knockdown has also been reported to decrease amino acid-stimulated insulin secretion³⁹.

The ME2 monomer is approximately 63 kilodaltons (kDa) when the mitochondrial transit peptide is removed. Each ME2 monomer has two NAD binding sites. Only one has catalytic activity, the active site, and the other site is the exo-NAD site^{29,40}. The biological function of the exo-NAD site is unknown^{29,30,40}. ME2 crystal structures in complex with ATP, show ATP can bind both the active and exo-NAD sites⁴¹. Structurally, ME2 is a tetramer that is a dimer of dimers³⁰. The dimer interface associates stronger than the tetramer interface^{30,40}. Purified ME2 reportedly exists as a mixture of tetramers and dimers^{41,42}. Mutagenesis studies at the tetramer interface indicated that ME2 dimers have activity, but the tetramer is the more active form of ME2⁴². ME2 kinetics revealed a high K_m value for malate due to malate-binding cooperativity. Malate can bind at the active site as well as the dimer interface⁴³.

ME2 has a complex regulatory system: it exhibits cooperative binding with respect to L-malate, it is allosterically activated by fumarate, and is competitively inhibited by ATP⁴³. Fumarate binds at the dimer interface and diminishes ME2 cooperative-binding of L-malate. This is consistent with the proposed function of ME2 in glutaminolysis²⁹. Fumarate is upstream of malate in the pathway, and increased fumarate would activate ME2 to promote energy production. Similarly, an excess of ATP would down-regulate glutaminolysis through inhibition of ME2, since ATP is a competitive inhibitor of ME2. This thesis identifies and discusses a new ME2 activator and its role in relieving oxidative stress.

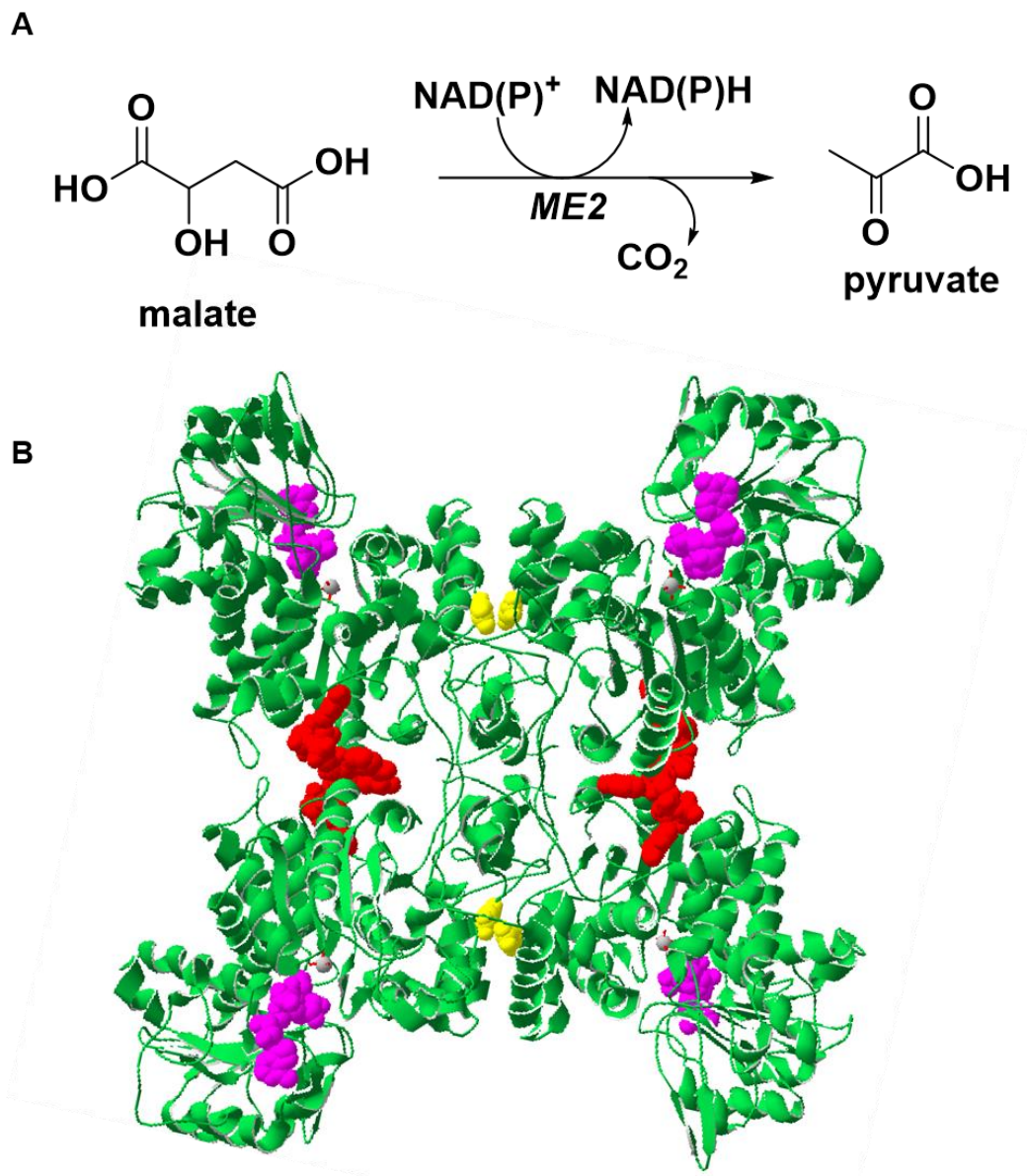


Figure 1.3 The enzymatic reaction and structure of ME2: (A) Enzymatic reaction of ME2. (B) Crystal structure of human ME2 (PDB ID code: 1PJ3). The active site NAD molecules are shown in purple and the exo-site NAD molecules are shown in red. The bound fumarate molecules are shown in yellow and the manganese ions are shown in grey sphere. The protein structure picture was generated using Swiss PDB Viewer.

REFERENCES

1. Leonardi, R., Zhang, Y. M., Rock, C. O. & Jackowski, S. Coenzyme A: Back in action. *Prog. Lipid Res.* **44**, 125–153 (2005).
2. Begley, T. P., Kinsland, C. & Strauss, E. The biosynthesis of coenzyme A in bacteria. *Vitam. Horm.* **61**, 157–171 (2001).
3. Subramanian, C. *et al.* Allosteric regulation of mammalian pantothenate kinase. *J. Biol. Chem.* **291**, 22302–22314 (2016).
4. Siudeja, K. *et al.* Impaired Coenzyme A metabolism affects histone and tubulin acetylation in *Drosophila* and human cell models of pantothenate kinase associated neurodegeneration. *EMBO Mol. Med.* **3**, 755–766 (2011).
5. Srinivasan, B. *et al.* Extracellular 4'-phosphopantetheine is a source for intracellular coenzyme A synthesis. *Nat. Chem. Biol.* **11**, 784–792 (2015).
6. Zhou, B. *et al.* A novel pantothenate kinase gene (PANK2) is defective in Hallervorden-Spatz syndrome. *Nat. Genet.* **28**, 345–349 (2001).
7. Dusi, S. *et al.* Exome sequence reveals mutations in CoA synthase as a cause of neurodegeneration with brain iron accumulation. *Am. J. Hum. Genet.* **94**, 11–22 (2014).
8. Tsuchiya, Y. *et al.* Protein CoAlation: a redox-regulated protein modification by coenzyme A in mammalian cells. *Biochem. J.* **474**, 2489–2508 (2017).
9. Adina-Zada, A. *et al.* Allosteric regulation of the biotin-dependent enzyme pyruvate carboxylase by acetyl-CoA. *Biochem. Soc. Trans.* **40**, 567–572 (2012).
10. McCoy, F. *et al.* Metabolic Activation of CaMKII by Coenzyme A. *Mol. Cell* **52**, 325–339 (2013).
11. Jiang, W. *et al.* Acetylation Regulates Gluconeogenesis by Promoting PEPCK1 Degradation via Recruiting the UBR5 Ubiquitin Ligase. *Mol. Cell* **43**, 33–44 (2011).
12. Lin, R. *et al.* Acetylation stabilizes ATP-citrate lyase to promote lipid biosynthesis and tumor growth. *Mol. Cell* **51**, 506–518 (2013).
13. Scott, I., Webster, B. R., Li, J. H. & Sack, M. N. Identification of a molecular component of the mitochondrial acetyltransferase programme: a novel role for GCN5L1. *Biochem. J.* **443**, 655–661 (2012).
14. Fan, J. *et al.* Tyr Phosphorylation of PDP1 Toggles Recruitment between ACAT1 and SIRT3 to Regulate the Pyruvate Dehydrogenase Complex. *Mol. Cell* **53**, 534–548 (2014).
15. James, A. M. *et al.* Non-enzymatic N-acetylation of Lysine Residues by AcetylCoA Often Occurs via a Proximal S-acetylated Thiol Intermediate Sensitive to Glyoxalase II. *Cell Rep.* **18**, 2105–2112 (2017).
16. Shi, L. & Tu, B. P. Acetyl-CoA and the regulation of metabolism: Mechanisms and consequences. *Current Opinion in Cell Biology* **33**, 125–131 (2015).
17. Pietrocola, F., Galluzzi, L., Bravo-San Pedro, J. M., Madeo, F. & Kroemer, G. Acetyl coenzyme A: A central metabolite and second messenger. *Cell Metabolism* **21**, 805–821 (2015).
18. Lin, H., Su, X. & He, B. Protein lysine acylation and cysteine succination by intermediates of energy metabolism. *ACS Chem. Biol.* **7**, 947–960 (2012).

19. Guarente, L. Sirtuins, aging, and metabolism. *Cold Spring Harb. Symp. Quant. Biol.* **76**, 81–90 (2011).
20. Martinez, D. L., Tsuchiya, Y. & Gout, I. Coenzyme A biosynthetic machinery in mammalian cells. *Biochem. Soc. Trans.* **42**, 1112–7 (2014).
21. Lee, J. V. *et al.* Akt-dependent metabolic reprogramming regulates tumor cell Histone acetylation. *Cell Metab.* **20**, 306–319 (2014).
22. Sadhukhan, S. *et al.* Metabolomics-assisted proteomics identifies succinylation and SIRT5 as important regulators of cardiac function. *Proc. Natl. Acad. Sci.* **113**, 1–6 (2016).
23. Du, J. *et al.* Sirt5 Is a NAD-Dependent Protein Lysine Demalonylase and Desuccinylase. *Science (80-.)*. **334**, 806–810 (2011).
24. Wang, Y. *et al.* KAT2A coupled with the α -KGDH complex acts as a histone H3 succinyltransferase. *Nature* **552**, 273–277 (2017).
25. Evans, M. J. & Cravatt, B. F. Mechanism-based profiling of enzyme families. *Chemical Reviews* **106**, 3279–3301 (2006).
26. Lau, O. D. *et al.* HATs off: selective synthetic inhibitors of the histone acetyltransferases p300 and PCAF. *Mol. Cell* **5**, 589–595 (2000).
27. Montgomery, D. C., Sorum, A. W. & Meier, J. L. Chemoproteomic profiling of lysine acetyltransferases highlights an expanded landscape of catalytic acetylation. *J. Am. Chem. Soc.* **136**, 8669–8676 (2014).
28. Montgomery, D. C. *et al.* Global Profiling of Acetyltransferase Feedback Regulation. *J. Am. Chem. Soc.* **138**, 6388–6391 (2016).
29. Xu, Y., Bhargava, G., Wu, H., Loeber, G. & Tong, L. Crystal structure of human mitochondrial NAD(P)⁺-dependent malic enzyme: A new class of oxidative decarboxylases. *Structure* **7**, 877–889 (1999).
30. Chang, G. G. & Tong, L. Structure and Function of Malic Enzymes, A New Class of Oxidative Decarboxylases. *Biochemistry* **42**, 12721–12733 (2003).
31. Valenti, V. & Pupillo, P. Activation Kinetics of NAD-Dependent Malic Enzyme of Cauliflower Bud Mitochondria. *Plant Physiol* **68**, 1191–1196 (1981).
32. Tronconi, M. A., Maurino, V. G., Andreo, C. S. & Drincovich, M. F. Three different and tissue-specific NAD-malic enzymes generated by alternative subunit association in *Arabidopsis thaliana*. *J. Biol. Chem.* **285**, 11870–11879 (2010).
33. Ren, J.-G., Seth, P., Everett, P., Clish, C. B. & Sukhatme, V. P. Induction of Erythroid Differentiation in Human Erythroleukemia Cells by Depletion of Malic Enzyme 2. *PLoS One* **5**, e12520 (2010).
34. Hsieh, J. Y., Chen, M. C. & Hung, H. C. Determinants of nucleotide-binding selectivity of malic enzyme. *PLoS One* **6**, (2011).
35. Jiang, P., Du, W., Mancuso, A., Wellen, K. E. & Yang, X. Reciprocal regulation of p53 and malic enzymes modulates metabolism and senescence. *Nature* **493**, 689–693 (2013).
36. Ren, J.-G. *et al.* Knockdown of malic enzyme 2 suppresses lung tumor growth, induces differentiation and impacts PI3K/AKT signaling. *Sci. Rep.* **4**, 5414 (2014).

37. Hsieh, J.-Y. *et al.* A small-molecule inhibitor suppresses the tumor-associated mitochondrial NAD(P)⁺-dependent malic enzyme (ME2) and induces cellular senescence. *Oncotarget* **6**, 20084–98 (2015).
38. Dey, P. *et al.* Genomic deletion of malic enzyme 2 confers collateral lethality in pancreatic cancer. *Nature* **542**, 119–123 (2017).
39. Pongratz, R. L., Kibbey, R. G., Shulman, G. I. & Cline, G. W. Cytosolic and mitochondrial malic enzyme isoforms differentially control insulin secretion. *J. Biol. Chem.* **282**, 200–207 (2007).
40. Tao, X., Yang, Z. & Tong, L. Crystal structures of substrate complexes of malic enzyme and insights into the catalytic mechanism. *Structure* **11**, 1141–1150 (2003).
41. Hsu, W., Hung, H., Tong, L. & Chang, G. Dual Functional Roles of ATP in the Human Mitochondrial Malic Enzyme †. 7382–7390 (2004).
42. Hsieh, J. Y., Chen, S. H. & Hung, H. C. Functional roles of the tetramer organization of malic enzyme. *J. Biol. Chem.* **284**, 18096–18105 (2009).
43. Hsieh, J. Y., Liu, G. Y., Chang, G. G. & Hung, H. C. Determinants of the dual cofactor specificity and substrate cooperativity of the human mitochondrial NAD(P)⁺-dependent malic enzyme: Functional roles of glutamine 362. *J. Biol. Chem.* **281**, 23237–23245 (2006).

CHAPTER 2

A CHEMOPROTEOMIC APPROACH IDENTIFIES MALIC ENZYME 2 AS A COENZYME A-DISULFIDE REGULATED PROTEIN

Abstract

Coenzyme A (CoA) is an important cofactor involved in numerous cellular biochemical reactions. We synthesized a biotin-tagged CoA probe to identify CoA-binding proteins using a chemical proteomic approach. Surprisingly, several metabolic enzymes that are not reported to utilize CoA were identified as top hits. We biochemically validated mitochondrial malic enzyme 2 (ME2) as a CoA-binding protein. ME2 is an NAD(P)-dependent enzyme that converts malate to pyruvate and simultaneously generates NAD(P)H. This enzyme plays important roles in lipogenesis and reactive oxygen species homeostasis. ME2 binds CoA with low μM affinity but binding of reduced CoA (CoA-SH) does not dramatically change its activity. By screening various CoA molecules, we discovered the oxidized dimer form of CoA, CoA-disulfide (CoA-S-S-CoA), significantly activates ME2 activity. CoA-SH and CoA-S-S-CoA bind to the previously established exo-NAD-binding site of ME2, promotes ME2 tetramer formation, and increases its enzymatic activity. Our work establishes that ME2 uses bound CoA-SH to sense oxidative stress and regulate ME2 activity.

Introduction

Coenzyme A (CoA) is an essential cofactor required for cellular metabolism in all living organisms. More than 100 different metabolic reactions utilize CoA as an acyl group carrier and carbonyl-activating group^{1,2}. Furthermore, CoA and its derivatives can regulate protein function through post-translational modifications and competitive or allosteric interactions. For example, various acyl-CoA molecules are known to acylate protein lysine, cysteine, or N-terminal glycine residues^{4-9,13}. The mitochondrial enzyme pyruvate carboxylase, which supplies oxaloacetate to the tricarboxylic acid (TCA) cycle through carboxylation of pyruvate, is allosterically activated by acetyl-CoA³. The levels and ratios of CoA and its derivatives are affected by various cellular factors such as nutrient availability, gene expression, intracellular metabolite concentrations and other stresses⁴⁻⁸. Changes in the CoA pool have been associated with various human diseases including cancer, diabetes and neurodegeneration⁹⁻¹⁵.

Given the important functions of various CoA molecules, we decided to use a chemical proteomic approach to identify CoA-binding proteins in mammalian cells. This work was partly driven by the recent identification of various acyl lysine modifications on proteins that may require acyl-CoA molecules as donors for the acyl group. We anticipated that some CoA-binding proteins could be candidate protein lysine acyltransferases. Therefore, we synthesized a biotin-CoA molecule to identify CoA-binding proteins. Surprisingly, the top protein hit, mitochondrial NAD-dependent malic enzyme (ME2), does not utilize CoA in its enzymatic reaction. ME2 belongs to a family of oxidative decarboxylases that convert L-malate to pyruvate in the presence of NAD or NADP^{16,17}. The family of malic enzymes play important roles in a wide range of

organisms¹⁸⁻²⁰. In mammals, ME2 is one of three malic enzyme isoforms and is the only isoform that can use both NAD and NADP for catalysis²¹. ME2 also has a complex regulatory system: it exhibits cooperative binding with respect to L-malate, is allosterically activated by fumarate and is competitively inhibited by adenosine triphosphate (ATP)²². ME2 has been implicated in numerous cellular processes such as proliferation, senescence, and reactive oxygen species (ROS) homeostasis^{20,23-26}. Depletion of ME2 modulated senescence through the activation of the tumor suppressor p53, NADP/NADPH ratios, and ROS. Therefore, ME2 is important for cellular metabolism, so we decided to validate ME2 as a CoA-binding protein and investigate the physiological function of ME2 binding to CoA. Interestingly, we discovered that ME2 uses the bound CoA to sense oxidative stress to regulate its activity.

Results

Identification of CoA-binding proteins using biotin-CoA

To identify CoA-binding proteins, we synthesized a biotin-tagged CoA probe (biotin-CoA) for use in quantitative proteomic studies. Synthesis of biotin-CoA began by producing an alkyne-tagged pantetheine analogue which was synthesized and purified as previously reported (**Fig. 2.1A**)^{27,28}. The pantetheine analogue, in the presence of ATP, was then processed by three CoA biosynthesis enzymes from *E. coli*, pantothenate kinase (CoaA), phosphopantetheine adenylyltransferase (CoaD) and dephospho-CoA kinase (CoaE), to form the alkyne-tagged CoA analogue. Biotin-azide was then attached to the CoA analogue by copper-catalyzed click chemistry (**Fig. 2.1B**).

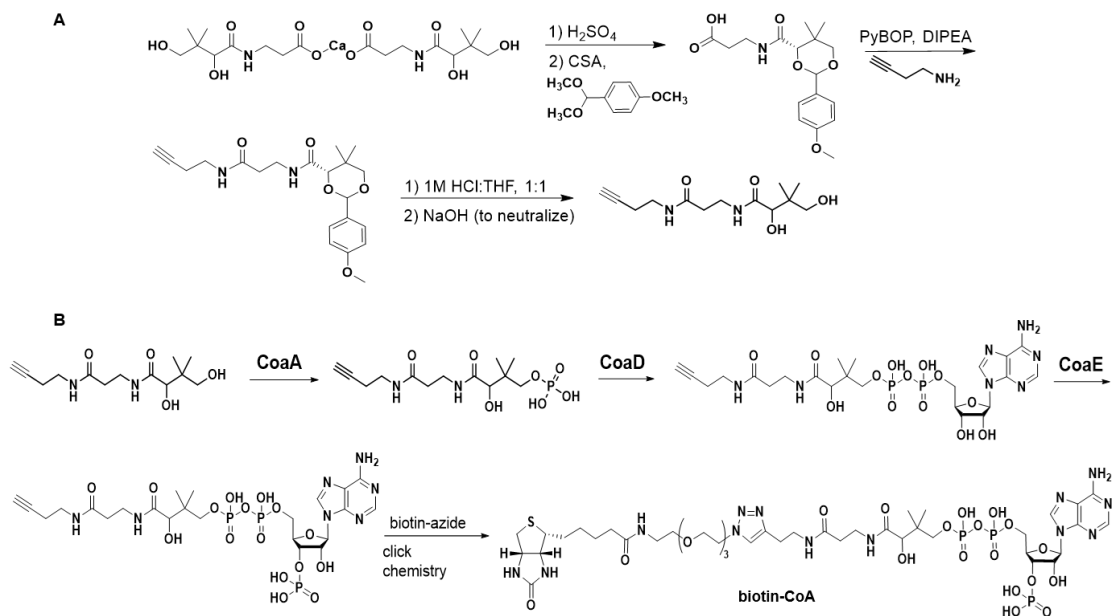


Figure 2.1: Biotin-CoA Synthesis: (A) Synthetic route for alkyne pantetheine analogue. **(B)** Biosynthesis followed by click chemistry for biotin-CoA

Utilizing the biotin-CoA probe, we performed two SILAC (stable isotope labeling by amino acids in cell culture) experiments in human embryonic kidney (HEK) 293T cells (**Fig. 2.2A**). For one of the experiments, we incubated heavy-labelled lysate with biotin-CoA and light-labelled lysate with biotin-azide to enrich CoA-binding proteins in the heavy-labelled sample. For the other SILAC experiment, we incubated both heavy-labelled and light-labelled lysates with biotin-CoA but added a 10-fold excess of reduced CoA (CoA-SH) to the light-labelled lysate to compete the biotin-CoA interactions. Both experiments enriched CoA-binding proteins in the heavy-labelled samples for proteomic analysis. Over 250 proteins were identified in each experiment (**Table 2.1 & 2.2**), and we analyzed the data based on heavy/light (H/L) ratios, number of unique peptides, and protein scores (**Fig. 2.2B**). This chapter is focused on the top protein identified, mitochondrial NAD-dependent malic enzyme (ME2). We also tested other hits for CoA binding and consequent activity changes (**Appendix A on Page 45**).

Accession	Description	Score	# Unique Peptides	Heavy/Light
Q32Q12	HCG2001850, isoform CRA_a	157.1	2	500.0
P23368	NAD-dependent malic enzyme, mitochondrial	19.4	6	500.0
Q9Y3I0	tRNA-splicing ligase RtcB homolog	5.5	2	500.0
B3KN02	cDNA FLJ13106 fis, clone NT2RP3002455, highly similar to DnaJ homolog subfamily C member 13	4.6	2	500.0
B5MD38	Trifunctional enzyme subunit beta, mitochondrial	2.8	1	500.0
Q9H369	PRO1633	2.8	1	500.0
A6NKC6	Retinitis pigmentosa 1-like 1 protein	2.4	1	500.0
P23284	Peptidyl-prolyl cis-trans isomerase B	2.1	1	500.0
F5H1Y3	Flap endonuclease 1 (Fragment)	1.8	1	293.2
O00746	Nucleoside diphosphate kinase, mitochondrial	25.0	5	99.9
Q9NUF9	Nucleoside diphosphate kinase (Fragment)	4.9	2	99.2
P15531	Nucleoside diphosphate kinase A	96.1	1	29.1
Q05DV5	ZC3HAV1 protein (Fragment)	14.8	4	9.5
B4DNK4	Pyruvate kinase	28.9	6	6.4
Q9H009	Nascent polypeptide-associated complex subunit alpha-2	3.7	1	5.6
Q6E433	Activated RNA polymerase II transcription cofactor 4 (Fragment)	7.3	2	3.4
B3KX15	cDNA FLJ44468 fis, clone UTERU2026025, moderately similar to SPLICING FACTOR, ARGININE/SERINE-RICH 2	2.2	1	2.1
Q75M91	Putative uncharacterized protein CGI-59 (Fragment)	2.8	1	1.9
J3KN60	Electron transfer flavoprotein subunit alpha, mitochondrial	3.1	1	1.6
B5BUB1	RuvB-like 1 (Fragment)	5.9	2	1.5
P11177	Pyruvate dehydrogenase E1 component subunit beta, mitochondrial	2.1	1	1.4
Q9BVA1	Tubulin beta-2B chain	142.6	1	1.4
P17858	6-phosphofructokinase, liver type	3.5	1	1.3
J3KTN1	Clathrin heavy chain 1 (Fragment)	9.3	2	1.3
P04350	Tubulin beta-4A chain	132.6	1	1.3
Q96AG4	Leucine-rich repeat-containing protein 59	2.7	1	1.3
H3BPA9	Nuclear pore complex protein Nup93 (Fragment)	2.3	1	1.3

Table 2.1 SILAC Sample#1 Results: Heavy-labelled lysate (biotin-CoA) and light-labelled lysate (biotin-azide). Proteins with H/L \geq 1.2 shown

Accession	Description	Score	# Unique Peptides	Heavy/Light
P23368	NAD-dependent malic enzyme, mitochondrial	37.1	7	500.0
B7Z7Q5	cDNA FLJ53385, highly similar to Excitatory amino acid transporter 4	3.0	1	500.0
Q9NUF9	Nucleoside diphosphate kinase (Fragment)	3.1	1	5.9
Q05DV5	ZC3HAV1 protein (Fragment)	6.1	2	5.7
O00746	Nucleoside diphosphate kinase, mitochondrial	36.7	5	5.2
Q32Q12	HCG2001850, isoform CRA_a	161.9	2	4.6
P15531	Nucleoside diphosphate kinase A	128.5	1	4.6
B2R4P2	cDNA, FLJ92164, highly similar to Homo sapiens peroxiredoxin 1 (PRDX1), mRNA	2.7	1	2.3
B2R7M3	cDNA, FLJ93510, highly similar to Homo sapiens JTV1 gene (JTV1), mRNA	5.7	2	2.3
B3KN02	cDNA FLJ13106 fis, clone NT2RP3002455, highly similar to DnaJ homolog subfamily C member 13	5.1	1	2.0
Q9Y277	Voltage-dependent anion-selective channel protein 3	14.6	3	2.0
Q5H928	3-hydroxyacyl-CoA dehydrogenase type-2	2.2	1	1.6
B4DP70	cDNA FLJ51017, highly similar to ATP-dependent RNA helicase DDX1 (EC 3.6.1.-) (Fragment)	1.8	1	1.5
Q9UNM1	Chaperonin 10-related protein (Fragment)	2.1	1	1.5
F8W1N5	Nascent polypeptide-associated complex subunit alpha (Fragment)	2.8	1	1.5
H7C4C8	T-complex protein 1 subunit theta (Fragment)	2.3	1	1.3

Table 2.2 SILAC Sample#2 Results: Heavy-labelled lysate (biotin-CoA) and light-labelled lysate (biotin-CoA + 10-fold excess of CoA-SH). Proteins with H/L \geq 1.2 shown

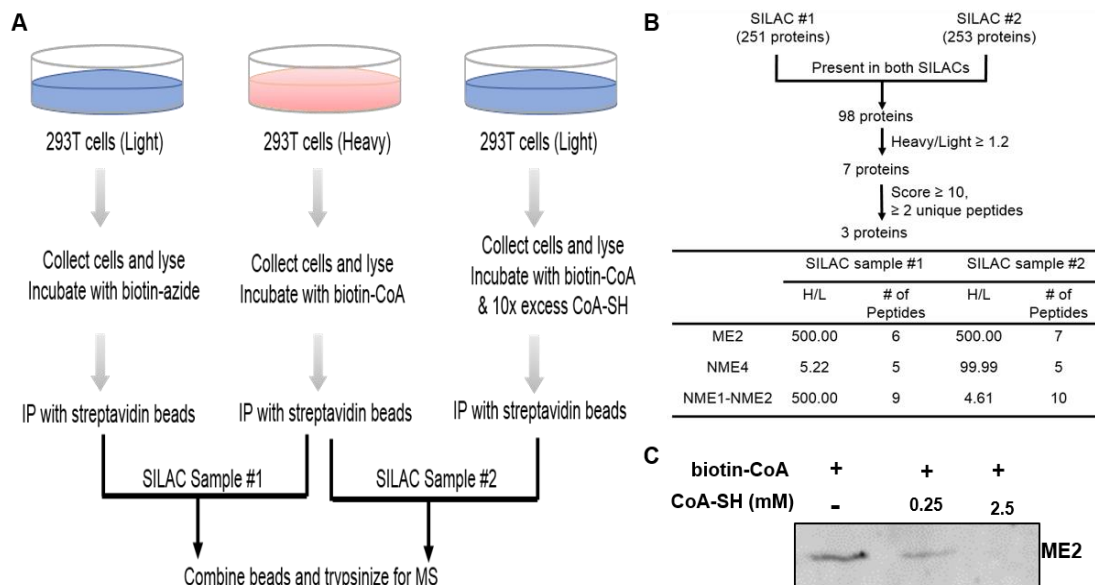


Figure 2.2: A chemical proteomic approach identified ME2 as a potential Coenzyme A-binding protein. (A) Schematic overview of the SILAC experiments to identify CoA-binding proteins. **(B)** SILAC results data analysis and filter. **(C)** Affinity-based capture of endogenous ME2 by biotin-CoA. Aliquots of the same lysate were used, and right lanes show capture experiments in the presence of increasing CoA-SH concentration.

Malic Enzyme 2 binds CoA-SH

To verify the SILAC data, HEK 293T cell lysate was aliquoted and incubated with biotin-CoA in the absence or presence of CoA-SH, followed by streptavidin bead pull down and anti-ME2 immunoblotting. Biotin-CoA immunoprecipitated endogenous ME2 and increasing CoA-SH concentration resulted in reduced ME2 binding, indicating that CoA-SH competes with biotin-CoA for ME2 (**Fig. 2.2C**). Using recombinant human ME2 purified from *E. coli*, thermal shift assays revealed that CoA-SH stabilizes ME2 *in vitro*, further confirming ME2 can bind CoA-SH (**Fig. 2.3A**).

The reported crystal structure of ME2 (PDB: 1PJ3) revealed two NAD-binding sites: the active site and the exo-NAD site²⁹. We hypothesized that the exo-NAD site could bind CoA because NAD and CoA share structural similarity. Three arginine

residues (R197, R542 and R556) in the exo-NAD site are important for NAD binding (**Fig. 2.3B**). These positively charged arginine residues interact with the negatively charged phosphate groups on NAD. To test whether the exo-NAD site is the CoA-binding site, we generated two ME2 mutants: R197E and R197E/R556E. Introduction of these negatively charged residues should result in electrostatic repulsion and therefore decreased binding of CoA. We incubated biotin-CoA with recombinant wildtype (WT), R197E and R197E/R556E ME2 followed by streptavidin bead pull down and Coomassie blue analysis. Only WT ME2 was effectively pulled down by biotin-CoA, indicating that these mutations in the exo-NAD site reduce CoA binding by ME2 (**Fig. 2.3C**).

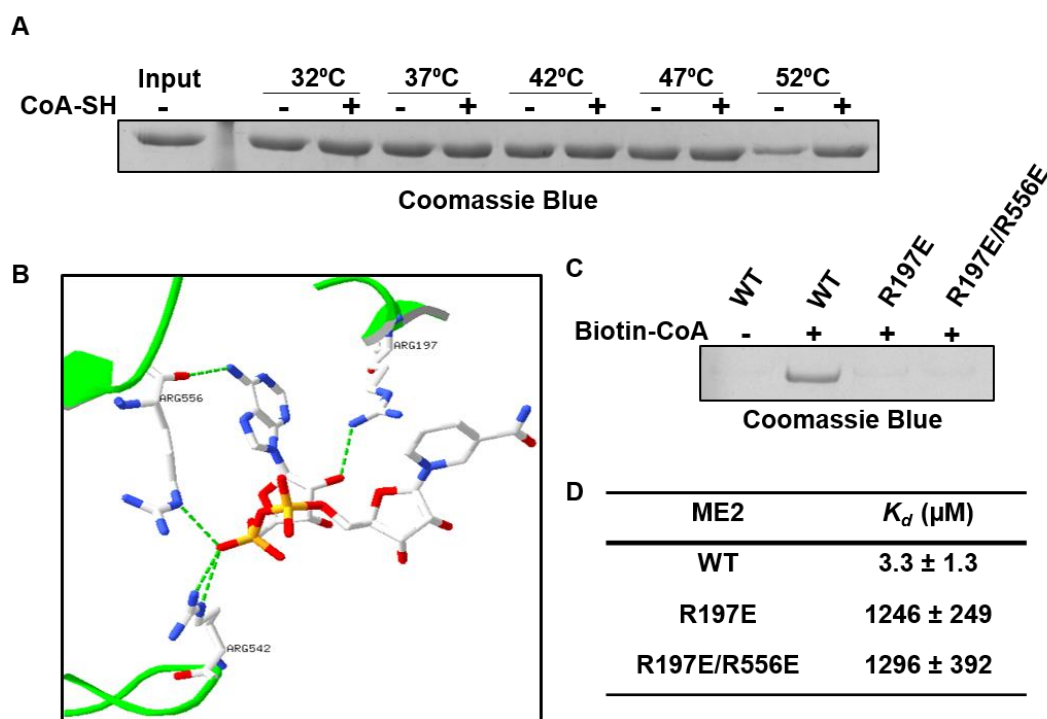


Figure 2.3: ME2 binds CoA-SH *in vitro*. (A) Thermal shift assay showing that ME2 was stabilized by CoA-SH (0.5 mM). (B) Crystal structure of exo-NAD site in human ME2 in complex with NAD (PDB ID code: 1PJ3). The three arginine residues involved in NAD binding are shown. The protein structure picture was generated using Swiss PDB Viewer. (C) Mutations in ME2 exo-NAD site reduced affinity-based capture by Biotin-CoA. (D) Mutations in ME2 exo-NAD site reduced CoA-SH binding.

We then used another binding assay to estimate the binding affinity of ME2 for CoA-SH. In this assay, WT, R197E or R197E/R556E ME2 was incubated with CoA-SH then filtered with a 10 kDa membrane. CoA-SH bound to ME2 remained on the membrane while unbound CoA-SH passed through the membrane. The CoA fraction bound (CFB) could then be used to calculate K_d . The estimated K_d of WT ME2 for CoA-SH was $3.3 \pm 1.3 \mu\text{M}$, R197E was $1246 \pm 249 \mu\text{M}$ and R197E/R556E was $1296 \pm 392 \mu\text{M}$ (**Fig. 2.3D**). The observed increase in estimated K_d values for ME2 mutants confirm significant reduction in CoA-SH binding. Thus, the exo-NAD site is the CoA-binding site of ME2.

As previously mentioned, ME2 is one of three malic enzymes in humans. Protein BLAST alignment indicate the other malic enzymes (ME1 and ME3) both have 56% identity to ME2, but the three arginine residues important for CoA-SH binding are not conserved in ME1 or ME3. Therefore, CoA binding is unique to ME2.

ME2 is activated by CoA-S-S-CoA

Next, we asked whether binding of CoA regulates ME2 activity. We incubated WT ME2 in the presence of NAD, with or without 100 μM CoA-SH or other CoA molecules, for 5 min then initiated the reaction by adding 1 mM of L-malate. The formation of NADH from NAD was monitored at 340 nm and the relative activities were determined. CoA-SH showed very little effect (~20%) on the activity of ME2. Similarly, various acyl-CoA molecules we tested did not affect the activity of ME2 much.

Examining the reported ME2 structure, we noticed in the active tetramer form of ME2 that two exo-NAD sites from two neighboring ME2 subunits are next to one

another. If each of the sites can be occupied by a CoA molecule, a covalently linked CoA dimer, such as CoA-disulfide (CoA-S-S-CoA), could potentially bind and promote the formation of ME2 tetramer. Therefore, we tested whether CoA-S-S-CoA could promote ME2 activity. Indeed, 100 μ M of CoA-S-S-CoA increased ME2 activity 2-fold (**Fig. 2.4A**). Next, we varied the concentration of CoA-S-S-CoA and observed lower concentrations led to even higher ME2 activity, with maximum ME2 activity achieved at 10 μ M (**Fig. 2.4B**).

The most studied allosteric activator of ME2 is fumarate^{22,29,30}. Fumarate is reported to diminish the ME2 cooperative binding of L-malate²². Previous studies used a range of 2-5 mM fumarate for ME2 activity studies, so we used 4 mM for our study^{22,29-31}. To compare the relative activation of ME2, we used a fixed enzyme concentration in the presence of CoA-S-S-CoA, fumarate or both. Activation by 10 μ M CoA-S-S-CoA was 4-fold greater than control compared to 2-fold greater for 4 mM fumarate. Also, the combination of CoA-S-S-CoA and fumarate did not further increase the activation compared to CoA-S-S-CoA alone (**Fig. 2.4C**).

Next, we measured the kinetic parameters of ME2. In the presence of CoA-S-S-CoA, the $K_{m(NAD)}$ for ME2 decreased by 3.70-fold compared to the 1.25-fold reduction with fumarate (**Fig. 2.4D**). The $k_{cat(NAD)}$ for ME2 increased 1.54-fold with CoA-S-S-CoA, which was similar to the 1.63-fold increase with fumarate. The $k_{cat(malate)}$ for ME2 with CoA-S-S-CoA and fumarate were comparable, with an increase of 1.26-fold with CoA-S-S-CoA and 1.36-fold with fumarate (**Fig. 2.4E**). Due to L-malate cooperative binding, ME2 demonstrates sigmoidal kinetics with respect to L-malate resulting in a large $K_{m(malate)}$. As previously reported, fumarate activation shifts the kinetics from

sigmoidal to hyperbolic and reduces $K_m(\text{malate})$. We observed the same effect with CoA-S-S-CoA activation, but our data showed $K_m(\text{malate})$ decreased by 3.67-fold with CoA-S-S-CoA and 1.79-fold with fumarate (**Fig. 2.4E**). These kinetic results confirm CoA-S-S-CoA is a significantly better ME2 activator than fumarate.

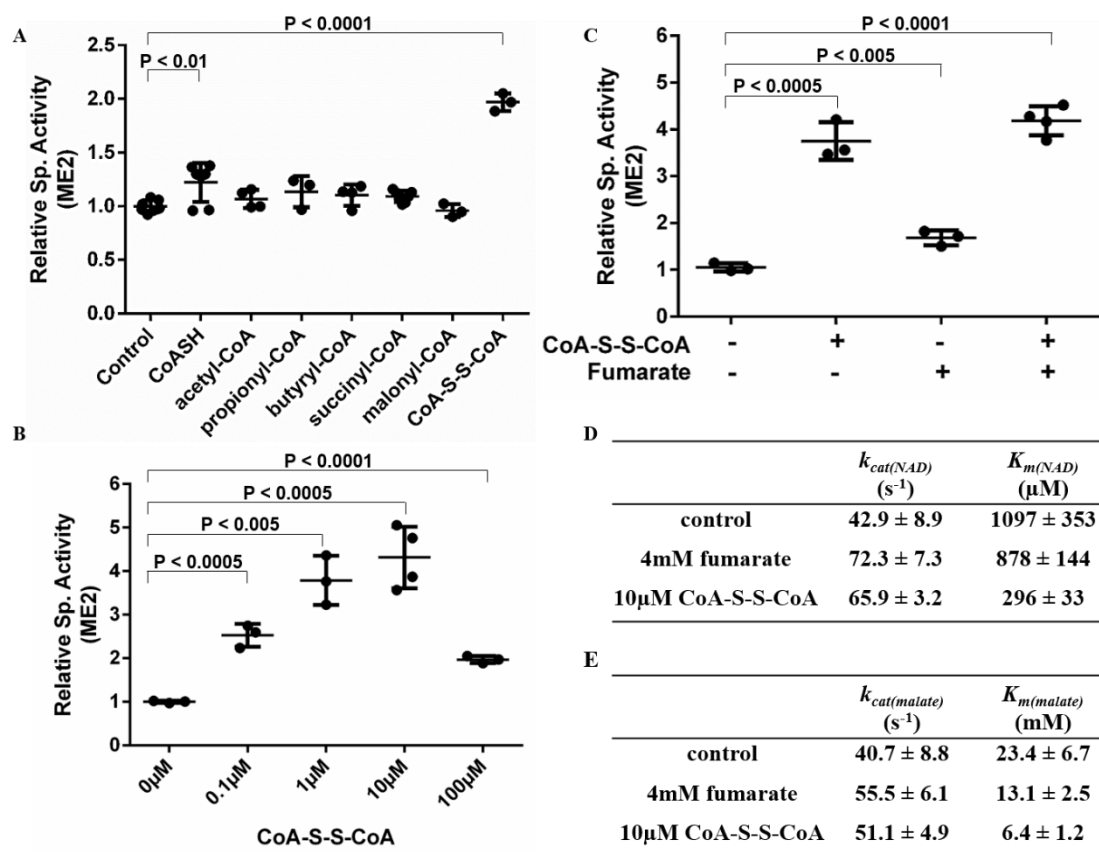


Figure 2.4. ME2 is allosterically activated by CoA-S-S-CoA *in vitro*. (A) Relative ME2 activity in the presence of various CoA molecules (100 μM). CoA-S-S-CoA resulted in a 2-fold increase in activity. (B) ME2 activation by CoA-S-S-CoA is dose-dependent with maximum activation at 10 μM . (C) CoA-S-S-CoA (10 μM) activation is greater than the activation by traditional allosteric activator fumarate (4 mM). All assays were initiated by the addition of 1mM L-malate. (D and E) Kinetic study of ME2 with and without activators varying (D) NAD and (E) L-malate concentrations.

CoA-S-S-CoA binds to the exo-NAD site to promote ME2 tetramer formation

To confirm ME2 activation was due to CoA-S-S-CoA binding to the exo-NAD site, we examined the effect of CoA-S-S-CoA on the activity of the ME2 mutants that

cannot bind CoA efficiently. CoA-S-S-CoA increased the activity of WT ME2, but not the R197E or R197E/R556E mutants (**Fig. 2.5A**), further confirming CoA-S-S-CoA binds to the exo-NAD site of ME2 to promote its activity.

Recombinant ME2 reportedly exists as a mixture of dimers and tetramers at neutral pH, with the tetramer being the more active form³². Given CoA-S-S-CoA binds at the tetramer interface, we hypothesized that CoA-S-S-CoA activates ME2 by promoting tetramer formation. To explore this, we used the protein cross-linker, disuccinimidyl suberate (DSS), to examine the oligomerization state of ME2 in the presence and absence of CoA-S-S-CoA. In the absence of CoA-S-S-CoA, WT and R197E ME2 had similar ratios of tetramer and dimer, indicating the exo-NAD site mutation did not affect ME2 oligomerization. For WT ME2 in the presence of CoA-S-S-CoA, the level of dimers decreased, and tetramers increased, compared to the sample without CoA-S-S-CoA (**Fig. 2.5B**). For R197E ME2, the ratios of dimer and tetramer were not affected by CoA-S-S-CoA. These results collectively demonstrate that CoA-S-S-CoA binds the exo-NAD site and promotes the tetramer formation of ME2 to increase its activity.

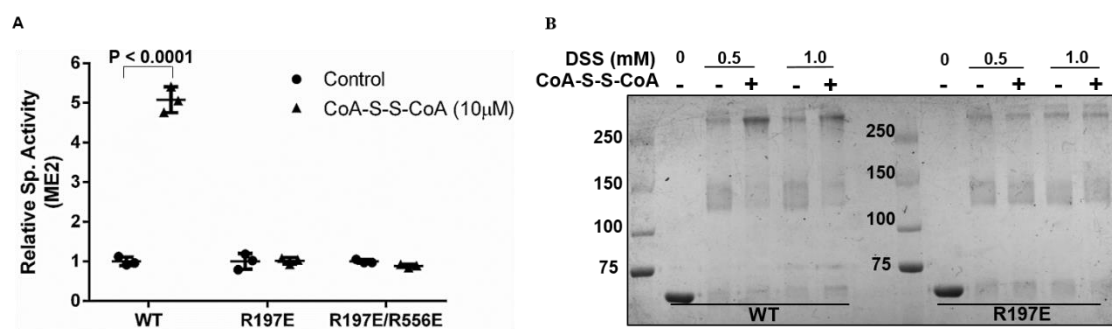


Figure 2.5: Mechanism by which CoA-S-S-CoA allosterically activates ME2. (A) CoA-S-S-CoA (10 μ M) activates wild-type ME2 but not ME2 mutants (B) Cross-linking assay showed that CoA-S-S-CoA promotes tetramerization of ME2.

CoA-S-S-CoA is present in mammalian cells

Our data suggest CoA-S-S-CoA can activate ME2 to regulate NADPH production (Fig. 2.6). Since the presence CoA-S-S-CoA in mammalian cells has not been reported, we first looked for this metabolite in A549 lung cancer cells. Indeed, we were able to detect CoA-S-S-CoA by LC-MS (Table 2.3). Next, we examined the effect of ME2 knockdown on the ratio of CoA-S-S-CoA to CoA-SH. Interestingly, ME2 knockdown decreased the CoA-S-S-CoA/CoA-SH ratio (Table 2.4). Given that ME2 is a mitochondrial enzyme, we reasoned that it regulates CoA-S-S-CoA in the mitochondria. To test this idea, we measured the abundance of CoA-S-S-CoA in mitochondria from control and ME2 knockdown cells. CoA-S-S-CoA was undetected in ME2 knockdown cells, suggesting that ME2 facilitates the formation of CoA-S-S-CoA in the mitochondria (Table 2.5).

Compounds	m/z	Z	A549	
			RT (min)	Peak area
CoA-S-S-CoA	765.10209	2	7.63	1.11×10^4
	509.73230	3	7.63	3.86×10^3
Sum				1.50×10^4
CoA-SH	766.10807	1	7.19	4.56×10^3
	382.55011	2	7.19	7.83×10^4
Sum				8.30×10^4
d ₃ Acetyl CoA	811.13678	1	7.74	4.25×10^4
	405.06448	2	7.74	3.30×10^4
CoA-S-S-CoA/CoA-SH				1.81×10^{-1}

Table 2.3. Detection of CoA-S-S-CoA and CoA-SH in A549 cell lysate. d₃-acetyl-CoA was added to samples as an internal positive control.

Compounds	m/z	Z	CTL KD		ME2 KD	
			RT (min)	Peak area	RT (min)	Peak area
CoA-S-S-CoA	765.10209	2	7.74	3.64×10^4	7.74	6.69×10^3
	509.73230	3	7.74	3.12×10^4	7.74	9.29×10^3
Sum				6.76×10^4		1.60×10^4
CoA-SH	766.10807	1	7.37	6.97×10^3	7.37	4.56×10^3
	382.55011	2	7.37	2.67×10^5	7.37	1.78×10^5
Sum				2.74×10^5		1.82×10^5
d ₃ Acetyl CoA	811.13678	1	7.88	1.23×10^4	7.88	2.03×10^4
	405.06448	2	7.88	3.49×10^5	7.88	4.14×10^5
CoA-S-S-CoA/CoA-SH				2.47×10^{-1}		8.77×10^{-2}

Table 2.4. Detection of CoA-S-S-CoA and CoA-SH in control and ME2 KD A549 cell lysates. d₃-acetyl-CoA was added to samples as an internal positive control.

Compounds	m/z	Z	CTL KD-mito		ME2 KD-mito	
			RT (min)	Peak area	RT (min)	Peak area
CoA-S-S-CoA	765.10209	2	7.63	3.84×10^3	7.63	0.00
	509.73230	3	7.63	8.03×10^2	7.63	0.00
Sum				4.65×10^3		0.00
CoA-SH	766.10807	1	7.19	3.22×10^2	7.19	1.87×10^3
	382.55011	2	7.19	1.43×10^5	7.19	1.57×10^4
Sum				1.43×10^5		1.75×10^4
d ₃ Acetyl CoA	811.13678	1	7.74	7.65×10^4	7.74	2.03×10^5
	405.06448	2	7.74	5.86×10^5	7.74	4.14×10^5
CoA-S-S-CoA/CoA-SH				3.24×10^{-2}		0.00

Table 2.5. Detection of CoA-S-S-CoA and CoA-SH in mitochondria isolated from control and ME2 KD A549 cells. d₃-acetyl-CoA was added to samples as an internal positive control.

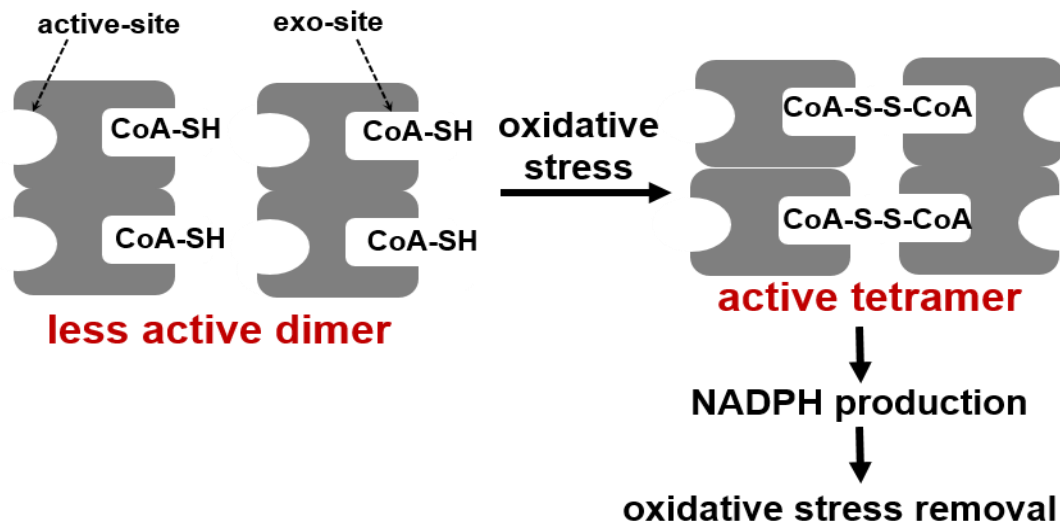


Figure 2.6: Proposed model of allosteric activation of ME2 by CoA-S-S-CoA to relieve oxidative stress

Discussion

CoA-disulfide (CoA-S-S-CoA) is present in certain bacterial and archaeal species which use reduced CoA (CoA-SH) as a replacement for glutathione³³. The presence of CoA-S-S-CoA in mammalian cells, to our best knowledge, has not been reported before. Our data indicate that CoA-S-S-CoA can be generated in the mitochondria of mammalian cells expressing ME2. Therefore, we hypothesize that CoA-S-S-CoA can serve as a signaling molecule to activate ME2 to increase NADPH production and thus reduce cellular oxidative stress. As seen in **Fig. 2.6**, when the less active dimers of ME2 experience oxidative stress, CoA-S-S-CoA forms and stabilizes the most active form of ME2, the tetramer. To investigate this model, experiments examining the effects WT or mutant ME2 have on mitochondrial NADPH/NADP ratios in cells subjected to oxidative stress must be done.

CoA-SH and CoA-S-S-CoA bind ME2 at a site previously shown, by crystal

structure analysis, to bind NAD(P) and ATP^{17,29,30}. Binding of CoA-S-S-CoA promotes ME2 tetramer formation. Thus, CoA-S-S-CoA essentially serves as a molecular glue to hold together this tetrameric form of ME2. The CoA-binding site of ME2 has several conserved arginine residues that are important for recognizing the negatively charged phosphates of CoA. Among the three isoforms of malic enzymes in humans, only ME2 has these conserved arginine residues and can respond to CoA-S-S-CoA. This is consistent with our proteomic data which identified only ME2, not ME1 or ME3, as a CoA-binding protein. This distinct regulation of ME2 suggests it is important for cellular oxidative stress and may explain why its deletion leads to severe biological defects^{20,23-26}.

Notably, this interesting finding, that CoA-S-S-CoA is a signaling molecule that turns on mitochondrial ME2, was discovered in a chemical proteomic approach to identify CoA-binding proteins. Such chemical proteomic approaches have become very popular in recent years and we note that a similar CoA chemical proteomics has been reported for identification of lysine acetyltransferases³⁴⁻³⁶. A key limiting factor in such chemical proteomic endeavors is to make sense of the data generated. Our study presented here suggests that such chemical proteomic data may hold the key to unveil the signaling functions of important metabolic cofactors.

Materials and Methods

Reagents

D-pantothenic acid hemicalcium salt (21210), p-anisaldehyde dimethyl acetal (10445), camphorsulfonic acid (C2107), 1-amino-3-butyne (715190) and azide-PEG3-biotin

(762024) were purchased from Sigma-Aldrich. Human/mouse mitochondrial malic enzyme antibody (sc-12399) and Anti-Rabbit antibody conjugated with horseradish peroxidase (sc-7074) antibodies were purchased from Cell Signaling Technology. Protease inhibitor cocktail, [$^{12}\text{C}_6$, $^{14}\text{N}_2$]-L-lysine, [$^{12}\text{C}_6$, $^{14}\text{N}_4$]-L-arginine, [$^{13}\text{C}_6$, $^{15}\text{N}_2$]-L-lysine and [$^{13}\text{C}_6$, $^{15}\text{N}_4$]-L-arginine were purchased from Sigma-Aldrich. Dialyzed FBS, FBS, DMEM, SILAC grade DMEM and RPMI media were purchased from Thermo Scientific. Ham's-F12 media was purchased from Corning. Sequencing grade modified trypsin were purchased from Promega. ECL plus western blotting detection reagent (80196) and disuccinimidyl suberate (21655) were purchased from Thermo Scientific. Sep-Pak C18 cartridge was purchased from Waters. Amicon Ultra centrifugal filter unit with ultracel-10 membrane was purchased from EMD Millipore. 2-(pyridyl)ethyl silica gel (53798), Coenzyme A- reduced (C3019) and oxidized (C2643), L-malate (M9138) and fumarate (F1506) were purchased from Sigma-Aldrich.

Biotin-CoA Synthesis

PMB-protected pantothenate²⁷: A flask with a stir bar and D-pantothenic acid hemicalcium salt (10 g, 42.0 mol) was flushed with nitrogen gas for 20 min. Anhydrous DMF (100 mL) was added followed by concentrated H_2SO_4 (1.3 mL dropwise, 42 mmol). The mixture was stirred for 15 min at room temperature. Then p-anisaldehyde dimethyl acetal (7.2 mL, 42 mmol) and camphorsulfonic acid (1 g, 4.6 mmol) were added and the reaction was stirred overnight. The reaction mixture was extracted at least three times with 75 mL ethyl-acetate and 100 mL water. The organic layers were combined and washed five times with 250 mL water, dried with Na_2SO_4 and evaporated. The resulting white solid was washed with 150 mL of cold ($-20\text{ }^\circ\text{C}$) dichloromethane to

remove any remaining p-anisaldehyde dimethyl acetal. The desired product was obtained as a white crystalline solid. ¹H-NMR (CDCl₃, 300 MHz): δ= 7.39 (d, 2H), 6.81 (d, 2H), 5.40 (s, 1H), 4.15 (s, 1H), 3.80 (s, 3H), 3.65-3.40 (m, 4H), 2.60 (t, 2H), 1.09 (s, 6H). ESI-MS [M] calcd. 336.3645 for C₂₁H₂₈N₂O₅, found 336.48.

Alkyne-tagged pantetheine analogue²⁸: To a flask flushed with nitrogen gas, PMB-protected pantothenate (434 mg, 1.28 mmol), PyBOP (732 mg, 1.41 mmol), and 1-amino-3-butyne (88mg, 1.28 mmol) were dissolved in dry dichloromethane (50 mL). Diisopropylethylamine (677 μL, 3.84 mmol) was then added, and the reaction was stirred overnight. The mixture was evaporated, and the resultant oil was purified by column chromatography (2: 1 Hex:EtOAc). The product was obtained as an oil. ¹H-NMR (300 MHz, CDCl₃) δ= 7.40 (d, 2H), 7.10 (m, 1H), 6.95 (m, 2H), 6.25 (m, 1H), 5.45 (s, 1H), 4.10 (s, 1H), 3.78 (s, 3H), 3.67 (m, 2H), 3.63-3.47 (m, 2H), 3.39-3.25 (m, 2H), 2.46 (t, 2H), 2.38 (t, 2H), 1.96 (m, 1H), 1.12 (s, 6H). The obtained product (87 mg, 0.22 mmol) was dissolved in 1M HCl:THF, 1:1 (10 mL) and stirred for 1 hr or until the starting material was gone by TLC, at which point 1M NaOH was added to neutralize the solution. The solvent was evaporated, and the product was purified by column chromatography (EtOAc to 15% MeOH-EtOAc). The desired compound was obtained as an oil. ¹H NMR (400 MHz, CDCl₃) δ 7.36 (s, 1H), 6.22 (s, 1H), 4.10 (q, 1H), 3.98 (s, 1H), 3.60 – 3.53 (m, 2H), 3.47 (d, 3H), 3.38 (qd, 2H), 2.45 (t, 2H), 2.39 (td, 3H), 1.00 (s, 3H), 0.91 (s, 3H). ESI-MS [M+Na]⁺ calcd 293.1433 for C₁₃H₂₂N₂O₄, found 293.10.

Biotin-CoA: The CoA biosynthesis enzymes, pantothenate kinase (CoaA), phosphopantetheine adenylyltransferase (CoaD) and dephospho-CoA kinase (CoaE), were purified from the *E. coli* ASKA strain library. Pantetheine analogue (5 mM in

HEPES pH 8.7 buffer) was added to a mixture of 100 mM HEPES pH 8.7, 18 mM MgCl₂, 18 mM ATP, 15 μM CoaA, 15 μM CoaD and 15 μM CoaE at 37 °C for 1 hr. The reaction was quenched with 1 eq acetonitrile (ACN) followed by centrifugation and purified by high-performance liquid chromatography (Buffer A: H₂O with 0.1% TFA, Buffer B: ACN with 0.1% TFA) to yield the CoA analogue, a white powder. ESI-MS [M+H]⁺ calcd 760.1504 for C₂₃H₃₆N₇O₁₆P₃, found 760.05. Click-chemistry was initiated by the addition of 3 mM sodium ascorbate to 2.86 mM CoA analogue, 2.76 mM biotin azide, 2 mM TBTA, and 2 mM CuSO₄ in 90 mM HEPES pH 8.7 at 37 °C for 1 hr. After centrifugation, the reaction mixture was purified by high-performance liquid chromatography (Buffer A: H₂O with 0.1% TFA, Buffer B: ACN with 0.1% TFA) to yield the Biotin-CoA, a white powder. ESI-MS [M/2+H]⁺ calcd 603.0305, found 603.12.

Stable isotope labeling with amino acids in cell culture (SILAC)

For proteomic experiments, the ‘Light’ and ‘Heavy’ human embryonic kidney (HEK) 293T cell lysates were prepared. ‘Light’ HEK 293T cells were maintained in SILAC grade DMEM media supplemented with 100 mg/L [¹²C₆, ¹⁴N₂]-L-lysine, 100 mg/L [¹²C₆, ¹⁴N₄]-L-arginine, and 10% dialyzed FBS. ‘Heavy’ HEK 293T cells were similarly maintained in SILAC grade DMEM media supplemented with 100 mg/L [¹³C₆, ¹⁵N₂]-L-lysine, 100 mg/L [¹³C₆, ¹⁵N₄]-L-arginine, and 10% dialyzed FBS. Cells were cultured in the SILAC media for eight doubling times to achieve maximum incorporation of ‘labeled’ amino acids into proteins before preparing the lysate for the proteomics experiment. After eight passages, the cells were collected and lysed using lysis buffer comprising of 50 mM HEPES pH 7.4, 150 mM NaCl, 1% NP-40, 10% glycerol, and

1% v/v protease inhibitor cocktail. After quantifying protein concentration by Bradford assay, two tubes with 3 mg 'heavy' lysate were incubated with 800 μ M Biotin-CoA and 3 mg 'light' lysate were incubated with either: (i) 800 μ M biotin-azide or (ii) 800 μ M biotin-CoA + 8 mM CoA-SH. After 30 min incubation, streptavidin beads were added and incubated for 1 hr. Supernatant was removed, and the beads were washed twice with washing buffer comprising of 50 mM HEPES pH 7.4, 150 mM NaCl, 0.2% NP-40, 10% glycerol. Each pair of samples (heavy labeled and light labeled) were mixed and then washed two more times. After washing, disulfide reduction and protein denaturation were performed in 6 M urea, 10 mM DTT, 50 mM Tris-HCl pH 8.0 at room temperature for 1 hr. Sulfhydryl alkylation was done by the addition of 40 mM iodoacetamide and incubation at room temperature for 1 hr. Alkylation was stopped with the addition of 3.8 mM DTT and incubation at room temperature for 1 hr. Samples were then diluted 7 times with 50 mM Tris-HCl pH 8.0, 1 mM CaCl₂. Trypsin digestion was initiated by the addition of 30 μ g trypsin and digestion was performed at 37 °C for 18 hr. Trypsin digestion was quenched with 0.2 % trifluoroacetic acid and the samples were desalted using Sep-Pak C18 cartridge and then lyophilized. The lyophilized peptides were dissolved in 2% ACN with 0.5% formic acid (FA) and nanoLC-MS/MS analysis was carried out on an LTQ-Orbitrap Elite mass spectrometer. Samples were loaded onto an Acclaim PepMap nano-Viper C18 trap column (5 μ m, 100 μ m x 2 cm, Thermo Dionex) for on-line desalting then separated on a C18 RP nano-column (5 μ m, 75 μ m x 50 cm, Magic C18, Bruker) at a flow rate of 0.3 μ L/min. The HPLC gradient was 5-38% ACN with 0.1% FA for 120 min. The Orbitrap was operated in positive mode with spray voltage 1.6 kV and source temperature 275 °C. Data-dependent

acquisition mode was used by one precursor ions MS survey scan from m/z 300 to 1800 at resolution 60,000 using FT mass analyzer, followed by up to 10 MS/MS scans at resolution 15,000 on 10 most intensive peaks. All data were acquired in Xcalibur 2.2 operation software package.

Validation of SILAC results

HEK 293T cells were lysed (50 mM HEPES pH 7.4, 150 mM NaCl, 1% NP-40, 10% glycerol) and 500 µg of protein lysate aliquoted into 4 tubes. Three of the tubes were incubated with 500 µM biotin-CoA for 15 min, then different concentrations of CoA-SH (0 mM, 0.25 mM, 2.5 mM) were added. Streptavidin beads were added to all four tubes and the tubes were incubated at room temperature for 30 min. Beads were washed (50 mM HEPES pH 7.4, 150 mM NaCl, 0.2% NP-40, 10% glycerol) at least four time and analysis by anti-ME2 immunoblotting was performed.

Western Blot Analysis

Protein samples were separated by SDS-PAGE and transferred to PVDF membranes. The membranes were blocked using 5% BSA in PBST (25 mM Tris-HCl, pH 7.4, 150 mM NaCl, 0.1% Tween-20) and incubated with antibodies in 5% BSA in PBST. Western blotting was detected using ECL Plus reagents and Typhon Imager.

Cell Culture

HEK 293T cells were cultured in complete DMEM medium supplemented with 10% heat-inactivated FBS. A549 cells were cultured in either RPMI or Ham-F12 media, both supplemented with 10% heat-inactivated FBS.

Construction of ME2 Plasmids

To make the cDNA library, total RNA was isolated from HEK 293T using the RNeasy

mini kit (Qiagen, 74106) according to the manufacturer's instructions. The isolated total RNA was used for the cDNA synthesis using RT-PCR. Flag-tagged ME2 (19 – 584) was PCR-amplified from HEK 293T cDNA using:

taattaatcatatgttgacataaaagaaaaaggcaagccacttatgc (forward primer) and

taattaatctcgagctaCTTATCGTCGTCATCCTTGTAATCttctgttatcacaggagggttgatg

(reverse primer with Flag-tag). ME2 was cloned into NdeI/XhoI restriction sites of

pET28a and was sequence-confirmed. Arginine-to-glutamate ME2 mutant vectors

were constructed using a quick-change site-directed mutagenesis strategy with the

following primers: R197E ME2: ggaatacggcctgatGAGtgctgccagtgtgt (forward

primer), atcaggccgtattcctgcacaagctgtatacaa (reverse primer). R556E ME2:

aaatatgtaaagaaGAGacatggcggagtgaa (forward primer), ttcttaacatattggccttgcttcaggctc

(reverse primer).

Expression and Purification of WT, R197E and R197E/R556E ME2 in *E. coli*

The sequence-confirmed pET28a plasmid was overexpressed in SoluBL-21. Cells were cultured at 37 °C in LB media with 50 µg/mL kanamycin. ME2 was purified using Ni-NTA affinity followed by size-exclusion chromatography. ME2 expression was induced by adding 200 µM isopropyl β-D-1-thiogalactopyranoside and cells were further incubated for 3 hr. Cells were collected at 11,000 g for 7 min and the cell pellet was stored at -80 °C until use. Cells were thawed and suspended in 50 mM HEPES pH 7.4, 500 mM NaCl, 30 mM imidazole, 1 mM MgCl₂, 1 mM PMSF. Cells were lysed using an EmulsiFlex-C3 cell disruptor and then centrifuged at 48,384 g for 45 min using a Beckman Coulter refrigerated floor centrifuge. The soluble fraction was loaded onto a Ni-NTA agarose column then washed with 50 mM HEPES pH 7.4, 500 mM NaCl, 30

mM imidazole, 1 mM MgCl₂. ME2 was eluted using 500 mM imidazole in wash buffer and concentrated for size-exclusion chromatography, which was performed using an ÄKTA pure chromatography system and a buffer of 50 mM HEPES pH 7.4, 500 mM NaCl, 1 mM MgCl₂. Fractions containing pure ME2 (determined by SDS/PAGE analysis) were collected, concentrated, and stored at -80 °C. All mutants of ME2 were purified similarly.

Thermal Shift Assay

In PCR tubes, 10 µM WT ME2 was mixed with or without 0.5 mM CoA-SH in a buffer of 50 mM HEPES pH 7.4, 500 mM NaCl, 1 mM MgCl₂. The tubes were then put in a PCR thermocycler with the temperature oscillating from 32 to 52 °C for different tubes. After incubation for 10 min, the samples were then transferred to 1.5 mL tubes and centrifuged at 17,000 g for 15 min to remove denatured proteins. The supernatant was analyzed by 12% SDS-PAGE and proteins were visualized by Coomassie blue staining.

Immunoprecipitation of Recombinant ME2 Proteins

WT, R197E, and R197E/R556E ME2 at 2 µM were mixed with 50 µM Biotin-CoA in a buffer containing 50 mM HEPES pH 7.4, 500 mM NaCl, 1 mM MgCl₂ for 15 min and then incubated with streptavidin beads for 30 min. Beads were washed at least three times with buffer and then then boiled in 95 °C and analyzed by 12% SDS-PAGE and Coomassie blue staining.

HPLC analysis of ME2 binding to CoA-SH

CoA-SH (50 µM) was incubated with and without 45 µM of WT, R197E, or R197E/R556E ME2 in 100 µL of buffer (50 mM HEPES pH 7.4, 500 mM NaCl, 1 mM MgCl₂) at room temperature for 30 min. The mixtures were then transferred to Amicon

Ultra-0.5 centrifugal filter units with ultracel-10 membrane. After centrifugation at 17,000 g for 20 min, 45 μ L of filtrate was used for HPLC analysis. The CoA-SH fraction bound (CFB) was calculated using the following equation:

$$CFB = \frac{A_0 - A}{A_0}$$

Where A_0 is the peak area from CoA-SH only samples and A is the peak area from CoA-SH in the presence of enzyme. The CFB was then used to estimate the dissociation constant (K_d) for WT, R197E, and R197E/R556E ME2. The one-site binding equation:

$$CFB = \frac{[E] + [CoASH] + Kd - \sqrt{([E] + [CoASH] + Kd)^2 - 4 \times [E] \times [CoASH]}}{2 \times [E]}$$

Was rearranged to calculate for K_d :

$$Kd = \frac{(CFB - 1) \times ([E] \times [CFB] - [CoASH])}{[CFB]}$$

where $[E]$ is ME2 concentration, $[CoASH]$ is CoA-SH concentration, and K_d is the dissociation constant.

ME2 Activity Assay

Enzyme activity was measured by monitoring the formation of NADH at 340 nm using a UV-visible spectrophotometer (Cary 50 UV-visible spectrophotometer; Varian). The reaction mixture contained 35 mM HEPES 7.4, 130 mM NaCl, 20 mM $MgCl_2$, 10 mM KCl, and 50 nM ME2. The mixture was incubated for 4 min at 37 $^{\circ}$ C in the presence or absence of a CoA molecule or fumarate (4 mM), then NAD was added, and the reaction was initiated by adding L-malate. All assays were done at 37 $^{\circ}$ C. For relative specific

activity assays, 1 mM NAD and 1 mM L-malate were used. CoA-SH and all acyl-CoAs were assayed at 100 μ M. CoA-S-S-CoA was tested at various concentrations with maximum activation observed at 10 μ M. The kinetics parameters were determined by using 10 mM L-malate with 0.05-1 mM NAD and 1.5 mM NAD with 0.5-20 mM L-malate. Data was analyzed using GraphPad Prism software.

Protein Cross-Linking

WT or R197E ME2 at 20 μ M was incubated with 10 μ M CoA-S-S-CoA in a buffer containing 50 mM HEPES pH 7.4, 500 mM NaCl, 1 mM $MgCl_2$ for 15 min. Crosslinking was done by the addition of 0.5 mM or 1 mM disuccinimidyl suberate (DSS) and incubation at room temperature for 30 min. The crosslinking reactions were stopped with the addition of 50 mM Tris pH 8.0 and incubation at room temperature for 15 min. Samples were analyzed by 8% SDS-PAGE and visualized by Coomassie blue staining.

Generation of ME2 Stable KD Cell Lines

ME2 shRNA lentiviral plasmids in pLKO.1-puro vector were purchased from Sigma-Aldrich. ME2 shRNA (TRCN0000294007, 3'UTR region):

CGGAGTTCTTACAGAGCTACTAAACTCGAGTTTAGTAGCTCTGTAAGAACT
TTTTTG was used. After co-transfection of ME2 shRNA plasmid, pCMV- Δ R8.2, and pMD2.G into HEK 293T cells, the medium was collected to infect A549 cells. The ME2 KD cells were selected using 2 μ g/mL puromycin in RPMI or Ham's-F12 media supplemented with 10% heat-inactivated FBS. Cells infected with lentivirus containing control shRNA plasmid were carried out similarly.

***d*₃-Acetyl-CoA Synthesis**

The synthesis of *d*₃-acetyl-CoA has been reported previously by our group³⁶ by modifying the method reported by Dils and Carey³⁸.

Extraction of CoA molecules from mammalian cells³⁷

All the extraction solutions, buffers and solvents used for the CoA extraction were pre-cooled on ice. Cells or mitochondria were spiked with 0.2 nmol of *d*₃-acetyl-CoA as an internal standard and were homogenized with 0.5 mL of methanol/water (1:1) containing 5% acetic acid (extraction buffer) using a Dounce homogenizer (30 strokes) on ice. The cell homogenates were centrifuged at 17,000 g for 15 min at 4 °C. The clear supernatant was loaded on a 3-mL ion exchange cartridge packed with 100 mg of 2-(pyridyl)ethyl silica gel. The cartridge had been pre-activated with 3 mL of methanol and then with 3 mL of extraction buffer. The ion exchange resin was washed with 2 mL of extraction buffer to remove unbound metabolites. The acyl-CoAs trapped on the silica gel cartridge were eluted twice with 0.5 mL of methanol/250 mM ammonium formate (4:1). The combined effluent was lyophilized and stored at -80 °C until LC-MS analysis.

Isolation of mitochondria from mammalian cells

Mitochondria isolation was done using the scaled down of the Shadel method³⁹. The protocol was followed as reported with the exception that all volumes used reduced by a factor of 22.

LC-MS analysis of extracted CoA molecules

The lyophilized CoA samples were re-suspended in 150 µL of 50 mM ammonium acetate pH 6.8, centrifuged at 17,000 g for 5 min and 10 µL were injected. An

UltiMate3000 RSLC (Thermo) was coupled to an OrbitrapElite mass spectrometer for metabolite separation and detection. A XTerraMS C18 column (150 mm x 2.1 mm i.d., 3.5 μ m, 155 Å) (Waters) was used with a flow rate of 200 μ L/min. The solvent A was water with 5 mM ammonium acetate pH 6.8 and solvent B was methanol. The solvent gradient was as follows: 0 min, 2% solvent B; 2 min, 2% solvent B; 4 min, 15% solvent B; 7.5 min, 95% solvent B; 17.5 min, 95% solvent B; 18 min, 2% solvent B; and 24 min, 2% solvent B. The OrbitrapElite operated in ESI negative ion FT mode with Ion Max-S API source under Xcalibur2.2. The following parameters were used: ESI voltage -4.0 kV, Sheath gas: 40 (arbitrary unit), Aux gas: 0; Sweep gas: 0, Source temperature: 325 °C, S-Lens RF level: 50%. A full scan in FTMS was set at 120,000 resolving power across 300 to 1600 (m/z) in profile mode followed by two MS/MS DDA scans acquired from 0 min to 24 min. All data were analyzed using Xcalibur2.2 software package.

REFERENCES

1. Leonardi, R., Zhang, Y. M., Rock, C. O. & Jackowski, S. Coenzyme A: Back in action. *Prog. Lipid Res.* **44**, 125–153 (2005).
1. Begley, T. P., Kinsland, C. & Strauss, E. The biosynthesis of coenzyme A in bacteria. *Vitam. Horm.* **61**, 157–171 (2001).
2. Leonardi, R., Zhang, Y. M., Rock, C. O. & Jackowski, S. Coenzyme A: Back in action. *Prog. Lipid Res.* **44**, 125–153 (2005).
3. Adina-Zada, A. *et al.* Allosteric regulation of the biotin-dependent enzyme pyruvate carboxylase by acetyl-CoA. *Biochem. Soc. Trans.* **40**, 567–572 (2012).
4. Shi, L. & Tu, B. P. Acetyl-CoA and the regulation of metabolism: Mechanisms and consequences. *Current Opinion in Cell Biology* **33**, 125–131 (2015).
5. Pietrocola, F., Galluzzi, L., Bravo-San Pedro, J. M., Madeo, F. & Kroemer, G. Acetyl coenzyme A: A central metabolite and second messenger. *Cell Metabolism* **21**, 805–821 (2015).
6. Lin, H., Su, X. & He, B. Protein lysine acylation and cysteine succination by intermediates of energy metabolism. *ACS Chem. Biol.* **7**, 947–960 (2012).
7. Guarente, L. Sirtuins, aging, and metabolism. *Cold Spring Harb. Symp. Quant. Biol.* **76**, 81–90 (2011).
8. Martinez, D. L., Tsuchiya, Y. & Gout, I. Coenzyme A biosynthetic machinery in mammalian cells. *Biochem. Soc. Trans.* **42**, 1112–7 (2014).
9. Siudeja, K. *et al.* Impaired Coenzyme A metabolism affects histone and tubulin acetylation in *Drosophila* and human cell models of pantothenate kinase associated neurodegeneration. *EMBO Mol. Med.* **3**, 755–766 (2011).
10. Srinivasan, B. *et al.* Extracellular 4'-phosphopantetheine is a source for intracellular coenzyme A synthesis. *Nat. Chem. Biol.* **11**, 784–792 (2015).
11. Zhou, B. *et al.* A novel pantothenate kinase gene (PANK2) is defective in Hallervorden-Spatz syndrome. *Nat. Genet.* **28**, 345–349 (2001).
12. Tsuchiya, Y. *et al.* Protein CoAlation: a redox-regulated protein modification by coenzyme A in mammalian cells. *Biochem. J.* **474**, 2489–2508 (2017).
13. Lee, J. V. *et al.* Akt-dependent metabolic reprogramming regulates tumor cell Histone acetylation. *Cell Metab.* **20**, 306–319 (2014).
14. Reibel, D. K., Wyse, B. W., Berkich, D. A. & Neely, J. R. Regulation of coenzyme A synthesis in heart muscle: effects of diabetes and fasting. *Am. J. Physiol. - Hear. Circ. Physiol.* **240**, H606–H611 (1981).
15. Jackowski, S. & Leonardi, R. Deregulated coenzyme A, loss of metabolic flexibility and diabetes. *Biochem. Soc. Trans.* **42**, 1118–22 (2014).
16. Xu, Y., Bhargava, G., Wu, H., Loeber, G. & Tong, L. Crystal structure of human mitochondrial NAD(P)⁺-dependent malic enzyme: A new class of oxidative decarboxylases. *Structure* **7**, 877–889 (1999).
17. Chang, G. G. & Tong, L. Structure and Function of Malic Enzymes, A New Class of Oxidative Decarboxylases. *Biochemistry* **42**, 12721–12733 (2003).
18. Valenti, V. & Pupillo, P. Activation Kinetics of NAD-Dependent Malic Enzyme of Cauliflower Bud Mitochondria. *Plant Physiol* **68**, 1191–1196 (1981).
19. Tronconi, M. A., Maurino, V. G., Andreo, C. S. & Drincovich, M. F. Three different and tissue-specific NAD-malic enzymes generated by alternative subunit association in *Arabidopsis thaliana*. *J. Biol. Chem.* **285**, 11870–11879 (2010).
20. Ren, J.-G., Seth, P., Everett, P., Clish, C. B. & Sukhatme, V. P. Induction of

- Erythroid Differentiation in Human Erythroleukemia Cells by Depletion of Malic Enzyme 2. *PLoS One* **5**, e12520 (2010).
21. Hsieh, J. Y., Chen, M. C. & Hung, H. C. Determinants of nucleotide-binding selectivity of malic enzyme. *PLoS One* **6**, (2011).
 22. Hsieh, J. Y., Liu, G. Y., Chang, G. G. & Hung, H. C. Determinants of the dual cofactor specificity and substrate cooperativity of the human mitochondrial NAD(P)⁺-dependent malic enzyme: Functional roles of glutamine 362. *J. Biol. Chem.* **281**, 23237–23245 (2006).
 23. Jiang, P., Du, W., Mancuso, A., Wellen, K. E. & Yang, X. Reciprocal regulation of p53 and malic enzymes modulates metabolism and senescence. *Nature* **493**, 689–693 (2013).
 24. Ren, J.-G. *et al.* Knockdown of malic enzyme 2 suppresses lung tumor growth, induces differentiation and impacts PI3K/AKT signaling. *Sci. Rep.* **4**, 5414 (2014).
 25. Hsieh, J.-Y. *et al.* A small-molecule inhibitor suppresses the tumor-associated mitochondrial NAD(P)⁺-dependent malic enzyme (ME2) and induces cellular senescence. *Oncotarget* **6**, 20084–98 (2015).
 26. Dey, P. *et al.* Genomic deletion of malic enzyme 2 confers collateral lethality in pancreatic cancer. *Nature* **542**, 119–123 (2017).
 27. Beld, J., Cang, H. & Burkart, M. D. Visualizing the chain-flipping mechanism in fatty acid biosynthesis. *Angew. Chemie* **53**, 14456–14461 (2014).
 28. Mercer, A. C., Meier, J. L., Hur, G. H., Smith, A. R. & Burkart, M. D. Antibiotic evaluation and in vivo analysis of alkynyl Coenzyme A antimetabolites in *Escherichia coli*. *Bioorganic Med. Chem. Lett.* **18**, 5991–5994 (2008).
 29. Tao, X., Yang, Z. & Tong, L. Crystal structures of substrate complexes of malic enzyme and insights into the catalytic mechanism. *Structure* **11**, 1141–1150 (2003).
 30. Hsu, W., Hung, H., Tong, L. & Chang, G. Dual Functional Roles of ATP in the Human Mitochondrial Malic Enzyme †. 7382–7390 (2004).
 31. Hsieh, J.-Y., Liu, J.-H., Fang, Y.-W. & Hung, H.-C. Dual roles of Lys(57) at the dimer interface of human mitochondrial NAD(P)⁺-dependent malic enzyme. *Biochem. J.* **420**, 201–209 (2009).
 32. Hsieh, J. Y., Chen, S. H. & Hung, H. C. Functional roles of the tetramer organization of malic enzyme. *J. Biol. Chem.* **284**, 18096–18105 (2009).
 33. Mallett, T. C. *et al.* Structure of coenzyme A-disulfide reductase from *Staphylococcus aureus* at 1.54 Å resolution. *Biochemistry* **45**, 11278–11289 (2006).
 34. Lau, O. D. *et al.* HATs off: selective synthetic inhibitors of the histone acetyltransferases p300 and PCAF. *Mol. Cell* **5**, 589–595 (2000).
 35. Montgomery, D. C., Sorum, A. W. & Meier, J. L. Chemoproteomic profiling of lysine acetyltransferases highlights an expanded landscape of catalytic acetylation. *J. Am. Chem. Soc.* **136**, 8669–8676 (2014).
 36. Montgomery, D. C. *et al.* Global Profiling of Acetyltransferase Feedback Regulation. *J. Am. Chem. Soc.* **138**, 6388–6391 (2016).
 37. Sadhukhan, S. *et al.* Metabolomics-assisted proteomics identifies succinylation and SIRT5 as important regulators of cardiac function. *Proc. Natl. Acad. Sci.* **113**, 1–6 (2016).
 38. Dils, R. & Car, E. M. 210, 371 (1970). 2 E. M. Carey and R. Dils., **1**, (1973).
 39. Clayton, D. A. & Shadel, G. S. Isolation of mitochondria from tissue culture cells. *Cold Spring Harb. Protoc.* **2014**, 1109–1111 (2014).

CHAPTER 3

CONCLUSIONS AND FUTURE DIRECTIONS

Conclusions

CoA is an important molecule found in all living organisms. Various enzymes require CoA for their catalytic functions in different metabolic pathways. In Chapter 2, I synthesized a CoA-analogue, biotin-CoA, and used it in quantitative proteomics to identify CoA-binding proteins. The mitochondrial NAD-dependent malic enzyme (ME2), previously unknown to bind or utilize CoA for its enzymatic activity, was a top hit. Using various *in-vitro* binding assays, I validated ME2 as a CoA-binding protein. I also identified the CoA-binding site by mutagenesis and showed that binding of the oxidized dimer form of CoA, CoA-disulfide (CoA-S-S-CoA), dramatically increased the activity of ME2. The source of this activation was due to increased tetramer formation, which lowered the K_m for both enzyme substrates, L-malate and NAD.

My data indicated that CoA-S-S-CoA can be generated in the mitochondria of mammalian cells expressing ME2. I propose that when the less active dimers of ME2 experience oxidative stress, CoA-S-S-CoA is formed and the most active form of ME2, the tetramer, is stabilized. Therefore CoA-S-S-CoA can serve as a signaling molecule that activates ME2 to increase NADPH production and thus reduce cellular oxidative stress. Along with the novel mechanism of ME2 activation, this work is the first report of the presence of CoA-S-S-CoA in human cells.

Future Directions

To better understand the physiological role of ME2 activation by CoA-S-S-CoA, the proposed model should be validated. This can be achieved by examining the effects WT or R197E/R556E ME2 have on mitochondrial NADPH/NADP ratios in cells subjected to oxidative stress. I expect the mitochondrial NADPH/NADP ratio in cells expressing R197E/R556E ME2 to be lower than cells expressing WT ME2.

The Chapter 2 study gave us confidence that novel proteins regulated by CoA molecules can be successfully identified using this chemical proteomics strategy. In biotin-CoA SILAC experiments, several other enzymes previously not known to bind or utilize CoA were identified. The success of this ME2 work suggest that additional hits may also be regulated by CoA molecules and thus would be interesting to study in the future. These enzymes include multiple members of the nucleoside-diphosphate kinases (NDPK) family of enzymes such as: NME1, NME1-NME2, and NME4. NDPK enzymes catalyze the transfer of a terminal phosphate group from a nucleoside triphosphate (NTP) to a different nucleoside diphosphate (NDP) and are linked to many cellular processes¹. Validation and further study of the identified enzymes could allow a better understanding of cellular metabolism as it relates to small metabolite regulation **(See Appendix A on Page 45)**.

In my proteomic method, I used relatively harsh washing conditions to only identify tightly bound proteins. Milder washing might help capture some of the weaker, yet important CoA-protein interactions such as the potential protein lysine acyltransferases. In addition, performing biotin-CoA proteomics on isolated mitochondria would help in identifying mitochondrial acyltransferases.

Given the discoveries made with biotin-CoA, identifying proteins that bind to and are regulated by other metabolites may also be worth pursuing. This may lead to more discoveries of novel cellular regulatory mechanisms. Some metabolites of interest include: s-adenosyl methionine (SAM), nicotinamide adenine dinucleotide (NAD), and nicotinamide adenine dinucleotide phosphate (NADP). SAM is a substrate for various enzymes involved in amino acid metabolism and methylation reactions. NAD and NADP are required substrates for many important metabolic enzymes. For example, the NAD-dependent protein deacetylase enzyme family, Sirtuins, function in aging, cancer, diabetes, and other diseases; therefore NAD also regulate those processes^{2,3}. Metabolites are essential for metabolism and may have currently unknown regulatory roles in cells.

REFERENCES

1. Peuchant, E. *et al.* Metastasis suppressor NM23 limits oxidative stress in mammals by preventing activation of stress-activated protein kinases / JNKs through its nucleoside diphosphate kinase activity. *Fed. Am. Soc. Exp. Biol.* **31**, 1531–1546 (2017).
2. Pirinen, E., Lo Sasso, G. & Auwerx, J. Mitochondrial sirtuins and metabolic homeostasis. *Best Pract. Res. Clin. Endocrinol. Metab.* **26**, 759–770 (2012).
3. Guarente, L. Sirtuins, aging, and metabolism. *Cold Spring Harb. Symp. Quant. Biol.* **76**, 81–90 (2011).

APPENDIX A
PRELIMINARY INVESTIGATION OF OTHER ENZYMES IDENTIFIED IN
BIOTIN-COENZYME A PROTEOMICS

Introduction

The nucleoside-diphosphate kinases (NDPK) family of enzymes catalyze the transfer of a terminal phosphate group from a nucleoside triphosphate (NTP) to a different nucleoside diphosphate (NDP)¹. NDPKs are linked to many cellular processes, including: differentiation, proliferation, cell migration, and apoptosis. NME1, for example, is a known metastasis suppressor and is implicated in oxidative stress protection^{1,2}. Four of the top CoA-binding proteins identified from our biotin-CoA proteomics were from the NDPK enzyme family (**Table A.1**).

The identified proteins NME1 (accession P15531) and NME1-NME2 (accession Q32Q12) are cytosolic proteins, while NME4 (accession O00746) is localized to the mitochondria. NME1-NME2 is a fusion protein, with 40% of the protein sequence matching most of NME1, starting from the N-terminus of NME1 and approximately 50% the protein sequence aligning with 100% of NME2 (accession P22392). We hypothesized that proteomic identification would not be able to distinguish NME1-NME2 from NME2, so purification of recombinant NME1 and NME2 but not the fusion protein was done. NME1, NME2, and NME4 were tested for CoA binding and activity changes in response to CoA.

Accession	Description	SILAC #1	SILAC #2
		Heavy/light	Heavy/Light
O00746	Nucleoside diphosphate kinase, mitochondrial GN=NME4	99.994	5.216
Q9NUF9	Nucleoside diphosphate kinase (Fragment) GN=c371H6.2	99.187	5.889
Q32Q12	HCG2001850, isoform CRA_a, GN=NME1- NME2	500.000	4.606
P15531	Nucleoside diphosphate kinase A, GN=NME1	29.141	4.570

Table A.1: List of nucleoside-diphosphate kinases identified in the biotin-CoA proteomics and their corresponding heavy/light ratios.

Results

We used recombinant human NME purified from *E. coli* to test NME binding of CoA. We incubated NME1, NME2 and NME4 with CoA-SH, then filtered with a 10 kDa membrane. CoA-SH bound to NME remained on the membrane while unbound CoA-SH passed through the membrane. The percentage bound is an indication of CoA binding. All NME proteins tested were shown to bind CoA-SH (**Fig. A.1**).

Next, we tested whether CoA binding regulates NME activity. We used a coupled reaction for detecting NME activity. NME generates ADP from ATP, then a reaction with pyruvate kinase (PK) occurs followed by lactate dehydrogenase (LDH) to monitor activity by NADH depletion (**Fig. A.2A**). 8-azido-ADP was used for these NME assays because NME can utilize it as a substrate but not PK. We incubated NME in the presence of phosphoenolpyruvate, NADH, PK/LDH and 8-azido-ADP, with or without 1 mM CoA-SH or 1 mM succinyl-CoA molecules for 5 min then initiated the

reaction by adding ATP. The formation of NAD from NADH was monitored at 340 nm and the relative activities were determined (**Fig. A.2B-D**). CoA-SH showed no effect on the activity and succinyl-CoA caused a slight decrease in activity. We also tested the effect of succinyl-CoA on PK/LDH coupled activity and saw no change in activity (**Figure A.3**).

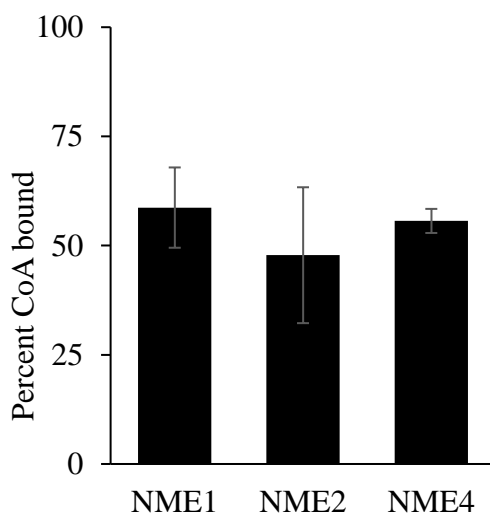


Figure A.1: Histogram showing the percentage of CoA-SH binding to NME1, NME2, and NME4. Binding percentage was determined using 10 kDa cut-off concentrators and HPLC analysis. Error bars indicate standard deviations from the averages of at least two replicates.

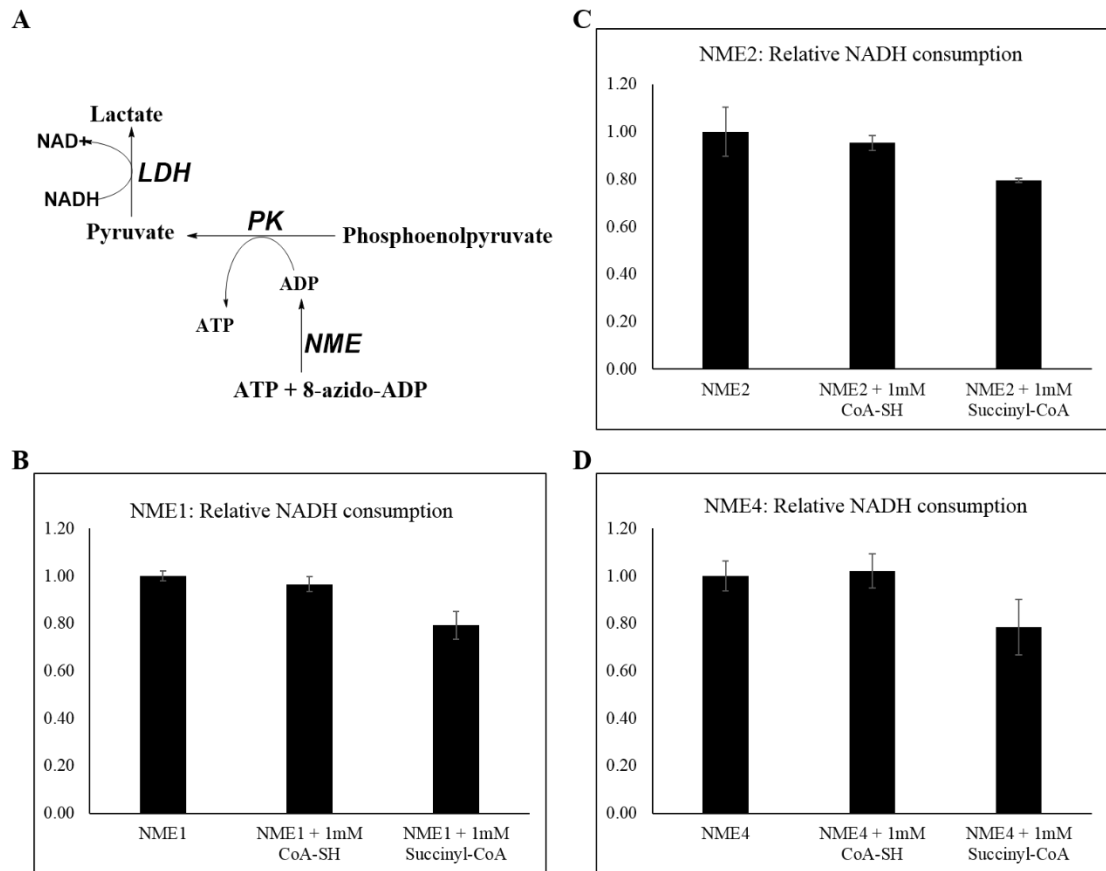


Figure A.2: Histogram showing relative NME activity with and without CoA molecules. (A) The coupled reaction for detecting NME activity. **(B-D)** Histogram showing relative activity with or without 1 mM CoA-SH or 1 mM succinyl-CoA for **(B)** NME1, **(C)** NME2 and **(D)** NME4. 8-azido-ADP was selected for these assays because NME can utilize it as a substrate but not PK. Error bars indicate standard deviations from the averages of at least three replicates.

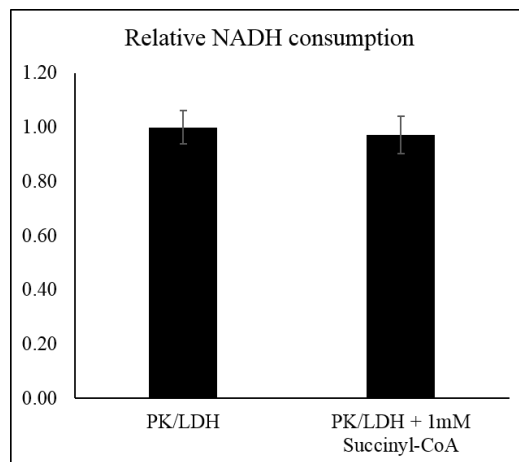


Figure A.3: Histogram showing relative activity of PK/LDH with and without succinyl-CoA. ADP was added to initiate reactions and 1 mM succinyl-CoA was tested. Error bars indicate standard deviations from the averages of at least three replicates.

Discussion

All three NME enzymes tested were shown to bind CoA-SH (**Fig. A.1**). The nucleotide kinase activity of NMEs were not affected by the presence of 1 mM CoA-SH. 1 mM succinyl-CoA resulted in activity decreases for all three NME enzymes tested (**Fig. A.2B-D**). This observed decrease may be due to chemical succinylation of the proteins rather than succinyl-CoA binding. Succinyl-CoA did not decrease PK/LDH coupled activity (**Fig. A.3**). Further work is needed to validate the effect of NME binding of CoA.

Materials and Methods

Reagents

Coenzyme A- reduced (C3019), Succinyl-CoA (S1129), phosphoenolpyruvate (P0564), adenosine 5'-triphosphate disodium salt (A2383), adenosine 5'-diphosphate sodium salt (A2754) and Pyruvate Kinase/Lactic Dehydrogenase enzymes from rabbit muscle (P0294) were purchased from Sigma-Aldrich. 8-Azidoadenosine 5-triphosphate sodium salt (53696-59-6) was purchased from Alfa Chemistry. Amicon Ultra centrifugal filter unit with ultracel-10 membrane was purchased from EMD Millipore.

Cloning, Expression and Purification of NME1, NME2, and NME4 in *E. coli*

Human NME1, NME2, and NME4 (29 – 187) were PCR-amplified from HEK 293T cDNA. The following primers were used:

NME1: taattaatgcatccatggccaactgtgagcgtacctc (forward primer),
taattaatctcgagctaCTTATCGTCGTCATCCTTGTAATCttcatagatccagttctgagcacagctc
(reverse primer with Flag-tag).

NME2: taattaatggatccatggccaacctggagcgcacc (forward primer),
taattaatctcgagctaCTTATCGTCGTCATCCTTGTAATCttcatagaccagtcagcacaagac
(reverse primer with Flag-tag).

NME4 (29-187): taattaatcatatgtctctggacccgggagcgg (forward primer),
taattaatGTCGACctaCTTATCGTCGTCATCCTTGTAATCggctgggtggatgctgctgtg
(reverse primer with Flag-tag).

NME1 and NME2 were cloned into pET28a using BamHI/XhoI sites and NME4 was cloned using NdeI/XhoI sites of pET28a. The sequence-confirmed plasmids were overexpressed in SoluBL-21. Cells were cultured at 37 °C in LB media with 50 µg/mL kanamycin. NME expression was induced by adding 200 µM isopropyl β-D-1-thiogalactopyranoside and cells were further incubated for overnight at 18°C. Cells were collected at 11,000 g for 7 min and the cell pellet was suspended in 50 mM HEPES pH 9.0, 500 mM NaCl, 30 mM imidazole, 1 mM MgCl₂, 1 mM PMSF. Cells were lysed using an EmulsiFlex-C3 cell disruptor and then centrifuged at 48,384 g for 45 min using a Beckman Coulter refrigerated floor centrifuge. The soluble fraction was loaded onto a Ni-NTA agarose column then washed with 50 mM HEPES pH 9.0, 500 mM NaCl, 30 mM imidazole, 1 mM MgCl₂. NME was eluted using a gradient of 50-500 mM imidazole in wash buffer. Fractions containing pure NME (determined by SDS-PAGE analysis) were collected, desalted by dialysis, and stored at -80 °C.

HPLC analysis of NME binding to CoA-SH

CoA-SH at 50 µM was incubated with and without 45 µM NME1, NME2 or NME4 in 100 µL of buffer (50 mM HEPES pH 9.0, 500 mM NaCl, 1 mM MgCl₂) at room temperature for 30 min. The mixtures were then transferred to Amicon Ultra-0.5

centrifugal filter units with ultracel-10 membrane. After centrifugation at 17,000 g for 20 min, 45 μ L of filtrate was used for HPLC analysis. The percentage CoA-SH bound (%CB) was calculated using the following equation:

$$\%CB = \frac{A_0 - A}{A_0} \times 100$$

Where A_0 is the peak area from CoA-SH only samples and A is the peak area from CoA-SH in the presence of enzyme.

NME Activity Assay

Enzyme activity was measured by the depletion of NADH at 340 nm using a UV-visible spectrophotometer (Cary 50 UV-visible spectrophotometer; Varian). The reaction mixture contained 35 mM HEPES 9.0, 150 mM NaCl, 20 mM MgCl₂, 400 μ M phosphoenolpyruvate, 100 μ M NADH, 133 μ M 8-azido-ADP, 25 nM NME and 5 μ g PK/LDH. The mixture was incubated at room temperature for 5 min with or without 1 mM CoA-SH/succinyl-CoA and then the spectrophotometer was started. After an additional 2 min, 233 μ M ATP was added to initiate the reaction. For PK/LDH only test reactions, 93 μ M of ADP was used.

REFERENCES

1. Peuchant, E. *et al.* Metastasis suppressor NM23 limits oxidative stress in mammals by preventing activation of stress-activated protein kinases / JNKs through its nucleoside diphosphate kinase activity. *Fed. Am. Soc. Exp. Biol.* **31**, 1531–1546 (2017).
2. Novak, M. *et al.* Metastasis suppressor NME1 regulates melanoma cell morphology, self-adhesion and motility via induction of fibronectin expression. *Exp. Dermatol.* **24**, 455–461 (2015).

APPENDIX B

METABOLOMICS-ASSISTED PROTEOMICS IDENTIFIES SIRT5 AS AN IMPORTANT REGULATOR OF HEART FUNCTION¹

Abstract

Cellular metabolites, such as acyl-CoA, can modify proteins, leading to protein posttranslational modifications (PTMs). One such PTM is lysine succinylation, which is regulated by sirtuin 5 (SIRT5). Although numerous proteins are modified by lysine succinylation, the physiological significance of lysine succinylation and SIRT5 remains elusive. Here, by profiling acyl-CoA molecules in various mouse tissues, we have discovered that different tissues have different acyl-CoA profiles and that succinyl-CoA is the most abundant acyl-CoA molecule in the heart. This interesting observation has prompted us to examine protein lysine succinylation in different mouse tissues in the presence and absence of SIRT5. Protein lysine succinylation predominantly accumulates in the heart when *Sirt5* is deleted. Using proteomic studies, we have identified many cardiac proteins regulated by SIRT5. Our data suggest that ECHA, a protein involved in fatty acid oxidation, is a major enzyme that is regulated by SIRT5 and affects heart function. *Sirt5* knockout (KO) mice have lower ECHA activity, increased long-chain acyl-CoAs, and decreased ATP in the heart under fasting conditions. *Sirt5* KO mice develop hypertrophic cardiomyopathy, as evident from the increased heart weight relative to body weight, as well as reduced shortening and ejection fractions. These findings establish that regulating heart metabolism and function is a major physiological function of lysine succinylation and SIRT5.

^{1a} This appendix is modified from published work: Sadhukhan S., Liu, X., Ryu, D., Nelson, O. D., Stupinski, J. A., Li, Z., Weiss, R. S., Locasale, J. W., Auwerx, J., and Lin, H., (2016), “Metabolomics-assisted proteomics identifies SIRT5 as an important regulator of heart function”, *Proceedings of the National Academy of Sciences*, 113 (16): 1–6.

^{1b} I constructed ECHA and ECHB plasmids for mammalian and *E. coli* expression and generated all mutants. I purified the ECHA-ECHB complex from *E. coli* and performed ECHA activity assays for *in-vitro* validation of SIRT5 regulation.

Introduction

Protein posttranslational modifications (PTMs) contribute toward the functional diversity of proteomes through regulating their activity, stability, and cellular localization. Many novel PTMs have been identified recently that result from enzymatic or nonenzymatic reactions with metabolites¹⁻⁵. Lysine, being the most frequently posttranslationally modified amino acid, has become the target of various PTMs such as acetylation, methylation, propionylation, butyrylation, crotonylation, succinylation, malonylation, glutarylation, long-chain fatty acylation, ubiquitination, and 2-hydroxyisobutyrylation^{1,3-9}. Unlike lysine acetylation, lysine succinylation is a relatively new PTM and the succinyl donor is presumably succinyl-CoA. Acetylation on lysine neutralizes the positive charge of lysine side chain and is known to affect the structure and function of chromatin¹⁰ as well as cellular metabolism¹¹. However, succinylation on lysine undergoes a complete charge reversal by changing a positively charged side chain to a negatively charged one. Regarding the change in charge, lysine succinylation is similar to phosphorylation, producing a two-unit charge shift in the modified residues. So, it can be anticipated that lysine succinylation would have a significant role in metabolic pathways, as was previously found for acetylation or phosphorylation.

Sirtuins are an evolutionarily conserved family of NAD-dependent lysine deacylases. Among the seven mammalian sirtuins (SIRT1–7), SIRT3–5 are located in mitochondria^{12,13}. Unlike SIRT3, both SIRT4 and SIRT5 have very weak deacetylase activities¹⁴. SIRT5 possesses unique enzymatic activity on hydrolyzing negatively charged lysine modifications such as lysine succinylation, malonylation, and

glutarylation^{1,4,8}. The presence of two positively charged amino acids, Tyr102 and Arg105, in the active site of SIRT5 explained its preference for negatively charged acyl groups such as succinyllysine¹. Although proteomic studies¹⁵⁻¹⁹ in mouse liver and skeletal muscle have identified hundreds of potential desuccinylation substrates of SIRT5 and several of these have been biochemically confirmed, the physiological significance of SIRT5 and lysine succinylation remains unclear. Deletion of *Sirt5* in mice produced only subtle phenotypes that seemed normal under basal conditions^{20,21} despite increased serum ammonium levels²². We thus set out to obtain crucial information that would help to reveal the function of lysine succinylation and SIRT5.

Acetyl-CoA and succinyl-CoA are important intracellular metabolites involved in diverse metabolic pathways including the TCA cycle. Differences in metabolism could lead to a differential distribution of acyl-CoAs across different tissues. In many recently discovered PTMs, the lysine side chains of proteins react with acyl-CoAs through their ϵ -amino groups. Thus, the distribution of acyl-CoA may significantly affect the PTMs. Herein, we have conducted a metabolomics study to first profile acyl-CoAs in various murine tissues and found that different tissues have very different acyl-CoA profiles. This has led us to examine protein lysine succinylation across different tissues. Protein lysine succinylation predominantly accumulates in the heart when *Sirt5* is deleted. We have identified many desuccinylation substrates of SIRT5 using proteomics, among which ECHA, a protein involved in fatty acid oxidation, is a major substrate in the heart. SIRT5 activates ECHA via desuccinylation and, as a result, *Sirt5*-deficient mice exhibit defective fatty acid metabolism and decreased ATP production. *Sirt5* knockout (KO) mice exhibit both reduced shortening fraction and

ejection fraction, implying a reduced cardiac function. Taken together, these findings reveal that a major physiological role of lysine succinylation and SIRT5 is to regulate heart metabolism and function.

Results

Different Mouse Tissues Have Unique Acyl-CoA Profiles

To obtain information that would help reveal the function of lysine succinylation and SIRT5, we profiled acyl-CoA concentrations, including succinyl-CoA (the presumed donor of succinyl for lysine succinylation), in major mouse organs such as liver, heart, kidney, brain, and muscle. This targeted metabolomics study conducted on acyl-CoAs from wild type (WT) mouse tissues revealed that different tissues have unique acyl-CoA profiles. For example, succinyl-CoA is the most abundant acyl-CoA in the heart. In the liver, the absolute concentration of succinyl-CoA is similar to that in the heart, but acetyl-CoA and free CoA are more abundant than succinyl-CoA (**Fig. B.1A**). This interesting acyl-CoA profile suggested that different tissues might have differential patterns of protein lysine succinylation and prompted us to examine succinylation in different mouse tissues.

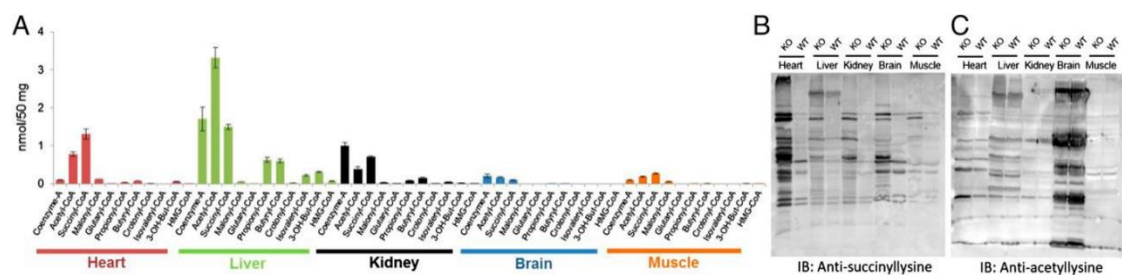


Figure B.1. Protein lysine succinylation occurs to the greatest extent in the heart. (A) Profiling of short-chain CoAs among different tissues from *Sirt5* WT mice using LC-MS/MS (mean \pm SEM, $n = 3$ mice). (B and C) Western blot of different tissue lysates (25 μ g each) against (B) anti-succinyllysine antibody and (C) against anti-acetyllysine antibody. *Sirt5* KO heart has the highest succinylation level. Coomassie stained gels (loading control) are shown in Fig. B.3D and E.

Protein Lysine Succinylation Predominantly Occurs in the Heart of *Sirt5* KO

Mice.

We next investigated the protein lysine succinylation and acetylation status in different tissues from *Sirt5* WT and KO mice. Western blot analysis for succinyllysine demonstrated that although the level of succinylation increased in all tissues when *Sirt5* was knocked out, it increased most dramatically in the heart (**Fig. B.1B**). Importantly, concentrations of succinyl-CoA and succinyl-carnitine were comparable in the *Sirt5* WT and KO mice's hearts (**Fig. B.2A and B**), implicating that the observed hypersuccinylation was generated by the deficiency of SIRT5 and not by increased succinyl donors. Levels of most of the short-chain acyl-CoAs remained unaltered in *Sirt5* WT and KO mice tissues (**Fig. B.2C–F**). Western blot analysis for acetyllysine showed no significant changes in acetylation in *Sirt5* WT and KO tissues (**Fig. B.1C**). The data suggested that among the mouse tissues tested, the desuccinylase activity of SIRT5 might play a very important role in the heart. Consistent with this hypothesis, among the different mouse tissues tested, the heart had the highest SIRT5 protein level (**Fig. B.3**). Very recently SIRT5 is found to possess deglutarylation activity in addition to its known deacetylation, demalonylation, and desuccinylation activity⁸. In general, glutaryl-CoA concentration is much lower compared with acetyl-CoA and succinyl-CoA. It is highest in the liver tissue among the tissues studied and hence, as expected, we found that the changes in protein lysine glutarylation level were rather small in all tissues examined when *Sirt5* was knocked out (**Fig. B.2G**). These results suggested that although SIRT5 can remove several different negatively charged acyl lysine modifications, the major acyl group removed in vivo is likely succinyl.

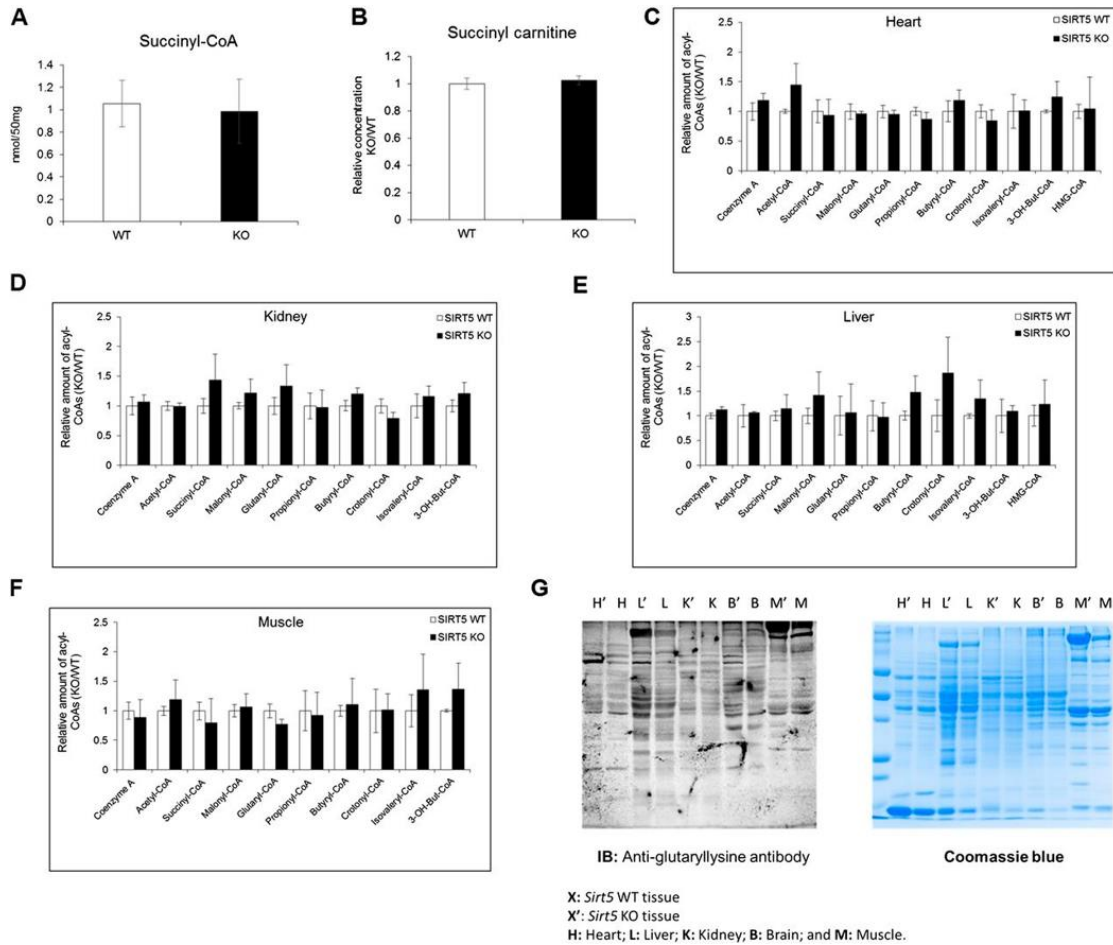


Figure B.2. Concentration of succinyl-CoA in mouse hearts from WT and *Sirt5* KO animals (A) Concentration of succinyl-CoA in mouse hearts from WT and *Sirt5* KO animals. (B) Relative level of succinyl-carnitine in mouse hearts from WT and *Sirt5* KO animals. (C–F) Relative level of short-chain acyl-CoAs in mouse heart, kidney, liver, and muscle from WT and *Sirt5* KO animals after 30 min of endurance exercise. The metabolomics data are provided as mean \pm SEM, $n = 3$ per genotype. (G) Western blot of different tissue lysates (25 μ g each) from *Sirt5* KO (designated by the prime sign) and WT mouse tissues against anti-glutaryllysine antibody. B, brain; H, heart; K, kidney; L, liver; M, muscle.

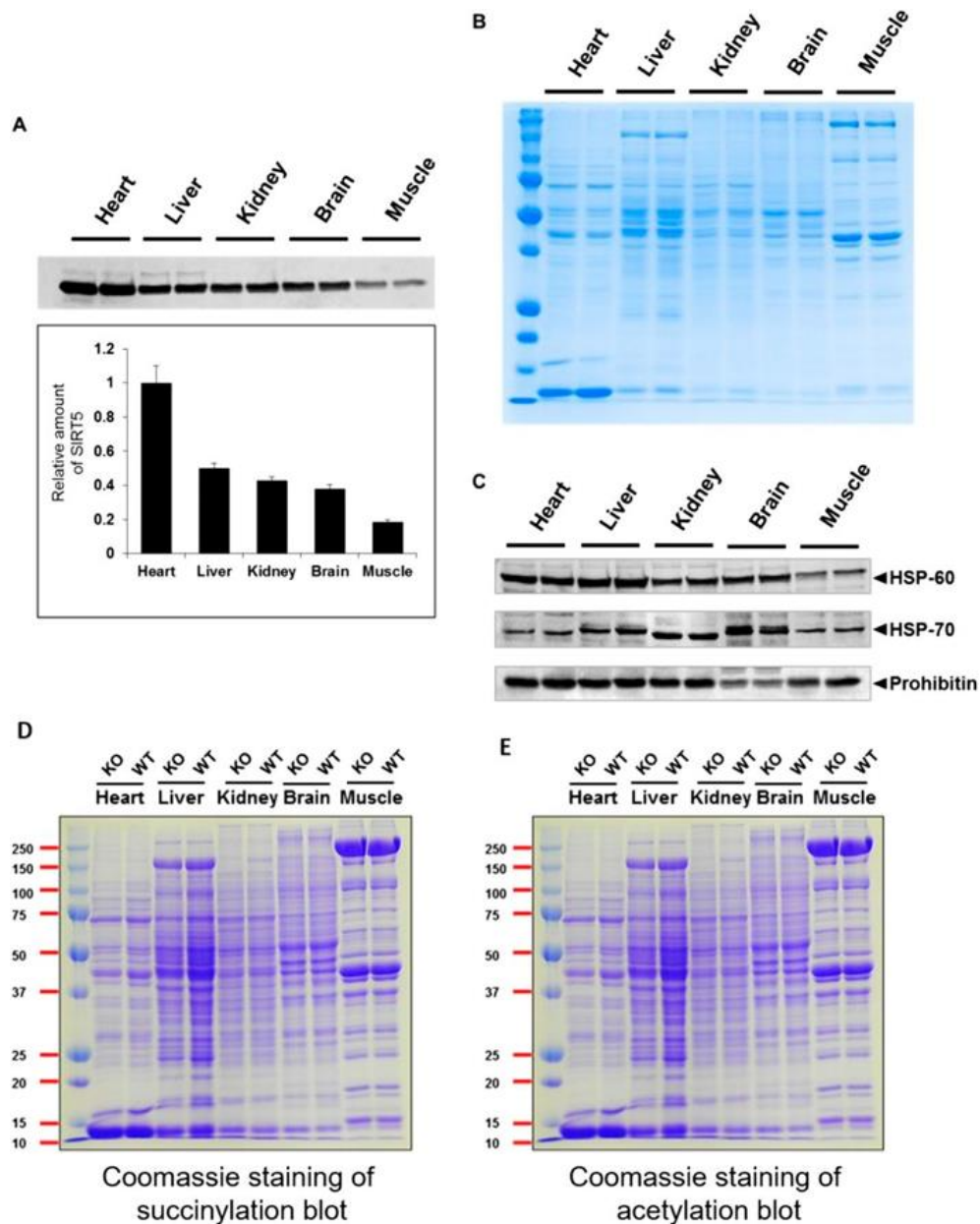


Figure B.3. SIRT5 Western blot for different tissue lysates (25 μ g each) from *Sirt5* WT mouse tissues showing that the heart has the highest amount of SIRT5. (A) SIRT5 Western blot for different tissue lysates (25 μ g each) from *Sirt5* WT mouse tissues showing that the heart has the highest amount of SIRT5. The experiment was done with tissues from two different mice (duplicate). (B) Coomassie-stained gel showing equal loading of total protein. (C) Prohibitin, HSP-60, and HSP-70 were used as a loading control. Because the readings with different markers were not consistent (e.g., in the brain lysate the Hsp70 level was very high but prohibitin level was very low), we used the total protein amount to normalize the results in A. (D and E) Coomassie-stained gels (loading control) for Western blot of different tissue lysates (25 μ g each) against anti-succinyllysine antibody (D) and anti-acetyllysine antibody (E).

Quantitative Proteomics on Lysine Succinylation from *Sirt5* WT and KO Heart

We next sought to identify proteins that are succinylated and regulated by SIRT5 in mouse heart. We used a proteomics approach involving reductive dimethylation²³ of the tryptic peptides followed by the enrichment of the succinylated peptides for identification by mass spectrometry (MS) (**Fig. B.4A**). Tryptic peptides from equal amounts of total lysate of *Sirt5* WT and KO mice heart tissues were separately labeled with heavy and light dimethyl groups, respectively. The labeled peptides were then mixed and succinylated peptides were enriched using an anti-succinyllysine polyclonal antibody. Nano liquid chromatography (LC)-MS/MS analysis was then carried out to compare the abundance of succinylated peptides in *Sirt5* WT and KO samples. MS analysis revealed 124 succinylated proteins that are potentially regulated by SIRT5. Among all the identified succinylated proteins, more than 75% were mitochondrial proteins (**Dataset B2.1**). More than 90% of succinylation sites showed increased abundance in *Sirt5* KO heart with an average KO/WT ratio of 8.37 and a median of 1.64 (**Dataset B2.2**). Significantly, over 25% of the sites showed over threefold greater abundance in *Sirt5* KO heart (**Dataset B2.2**).

To gain insight into how lysine succinylation and SIRT5 might affect mitochondrial metabolic networks, we performed pathway enrichment analysis using DAVID bioinformatics resources^{24,25}. Consistent with earlier reports, a number of metabolic pathways including branched-chain amino acids metabolism, the TCA cycle, fatty acid metabolism, propanoate metabolism, oxidative phosphorylation, pyruvate metabolism, and ATP synthesis are significantly enriched among the SIRT5 desuccinylation targets (**Fig. B.4C**)^{16,18,19}. It is possible that the regulation of all these

metabolic enzymes collectively contributes to the biological function of SIRT5 and lysine succinylation in the heart. Nevertheless, to gain a better understanding of the physiological roles for SIRT5, we sought to identify the pathway that is significantly affected in the heart when *Sirt5* is knocked out and that can play important roles in regulating heart function.

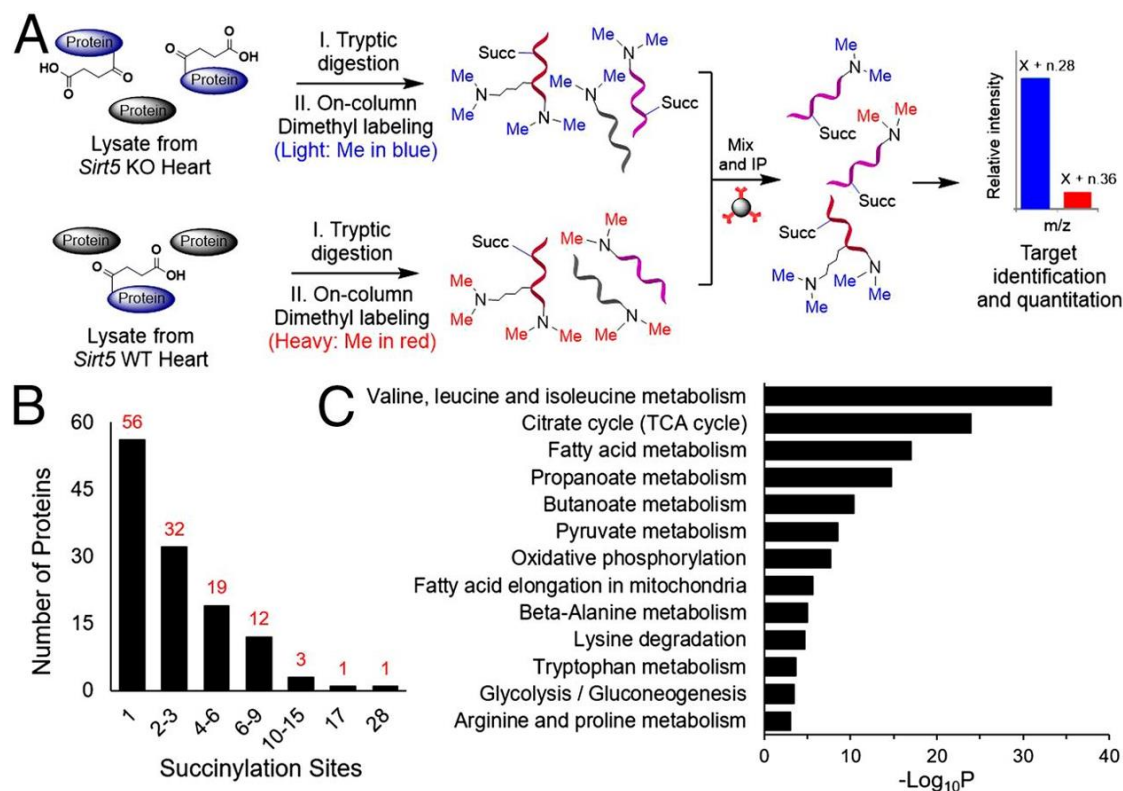


Figure B.4 Workflow of the dimethyl-labeling strategy for the succinylome analysis. (A) One milligram of total protein from *Sirt5* KO and WT heart was separately digested with trypsin and labeled with light and heavy dimethyl groups, respectively. The isotopically labeled peptides were mixed together and immunoprecipitated with anti-succinyllysine antibody. Succinyl-lysine peptides were then analyzed by nano LC-MS/MS. (B) Distribution of number of lysine succinylation sites per protein. (C) Metabolic pathways enriched with lysine succinylated proteins.

One feature that caught our attention was that the number of succinylation sites per protein varied significantly (from 1 to 28) depending on the protein (Fig. B.4B). ECHA was identified to have the most succinylation sites (at 28 Lys residues) in

the *Sirt5* KO heart. Among the 66 lysine residues of ECHA, 28 were succinylated and the majority of succinylated residues (26 out of 28) were only found in *Sirt5* KO heart, indicative of ECHA being a target of SIRT5. We focused on ECHA for biochemical validations for two considerations. First, we examined several other desuccinylation targets of SIRT5 (e.g., citrate synthase and ATP synthase) and found that the activities of these targets were not significantly affected by SIRT5 in the heart. Second, ECHA is most abundant in the heart compared with other tissues. ECHA is the α -subunit of mitochondrial trifunctional enzyme, which is important for fatty acid β -oxidation and has three distinct activities: enoyl-CoA hydratase (ECH), 3-hydroxyacyl-CoA dehydrogenase (HACD), and 3-ketoacyl-CoA thiolase (KCAT)²⁶. The α -subunit (ECHA) has the ECH and HACD activities whereas the β -subunit (ECHB) harbors the KACT activity.

SIRT5 Activates ECHA by Desuccinylation.

To confirm that ECHA was indeed hypersuccinylated in SIRT5-deficient mice, we immunoprecipitated ECHA from *Sirt5* WT and KO mouse heart and analyzed the succinylation level by Western blot using anti-succinyllysine antibody. ECHA was highly succinylated in the absence of SIRT5 (**Fig. B.5A**). Similarly, Flag-tagged mouse ECHA (Flag-ECHA) in *Sirt5* knockdown (KD) HEK-293T cells was hypersuccinylated compared with ECHA from control KD cells (**Fig. B.5B**). When Flag-ECHA was cotransfected with an expression vector for either SIRT5, or its catalytic mutant SIRT5-H158Y, into HEK-293T cells, ECHA succinylation level was decreased when coexpressed with SIRT5, but not with SIRT5-H158Y (**Fig. B.5C**). Additionally, when coexpressed, Flag-ECHA was able to immunoprecipitate V5-tagged SIRT5, suggesting

that ECHA and SIRT5 interact with each other (**Fig. B.5D**).

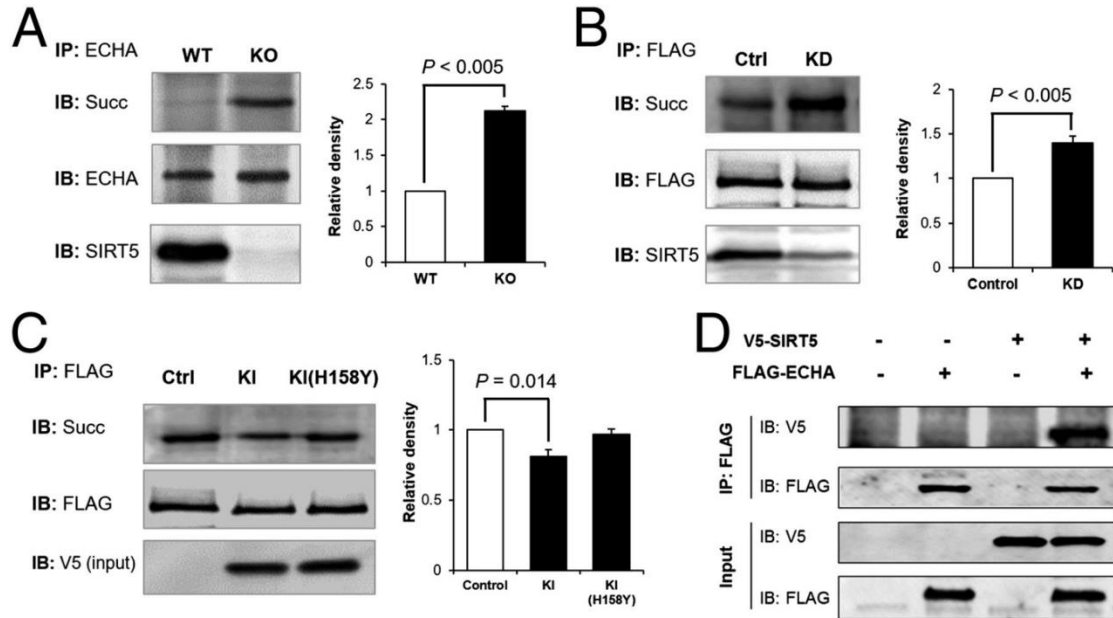


Figure B.5 Lack of SIRT5 leads to hypersuccinylation on ECHA. (A) ECHA was immunoprecipitated from *Sirt5* WT and KO mouse heart using ECHA-specific antibody. *Sirt5* KO mouse heart had increased succinylation on endogenous ECHA. (B) Flag-ECHA expressed in HEK-293T *Sirt5* KD cells showed increased succinylation compared with Flag-ECHA from control KD cells. (C) Overexpression of WT SIRT5, but not catalytically inactive SIRT5-H158Y, decreased the succinylation level of ECHA. Quantitative representation of relative density of succinylation (mean \pm SEM, $n = 3$) is shown for A–C. (D) Flag-ECHA and V5-tagged SIRT5 were co-overexpressed in HEK-293T cells. Immunoprecipitation of Flag-ECHA pulled down V5-tagged SIRT5.

Next, we aimed to determine whether the succinylation of ECHA modulates its enzymatic activity. The combined ECH and HACD activities of ECHA were measured by monitoring the formation of NADH from NAD at 340 nm²⁷ using 2-(E)-decenoyl-CoA as a substrate. ECHA from *Sirt5* KO heart showed a 32% decrease in activity compared with that from *Sirt5* WT heart, suggesting that ECHA succinylation down-regulates its activity (**Fig. B.6A**). Similarly, ECHA purified from *Sirt5* KD HEK-293T

cells showed a lower activity than that from the control cells (**Fig. B.6B**). Co-expression of ECHA with SIRT5 decreased ECHA succinylation (**Fig. B.5C**) and led to a 24% increase in enzymatic activity (**Fig. B.6B**). Coexpression of ECHA with SIRT5-H158Y did not change ECHA succinylation (**Fig. B.5C**) or increase its activity (**Fig. B.6B**). We also purified recombinant mouse trifunctional protein complex (ECHA and ECHB) from *Escherichia coli* to test the consequence of succinylation on its activity in vitro. We first treated the recombinant ECHA and ECHB complex with succinyl-CoA for 10 min at 27 °C to prompt non-enzymatic succinylation, and then the reaction mixture was further incubated with or without SIRT5 for 10 min at 27 °C. Non-enzymatically succinylated ECHA and ECHB complex showed a 40% reduction in activity, but upon SIRT5 treatment the activity was restored (**Fig. B.6C**). To evaluate whether lysine acetylation also regulates ECHA activity, we performed a chemical acetylation of ECHA and ECHB complex by incubating it with acetic anhydride and checked its activity. As shown in **Fig. B.7A**, we did not observe any change in ECHA activity after it was acetylated. This result further demonstrates that ECHA activity is regulated by succinylation and SIRT5-catalyzed desuccinylation.

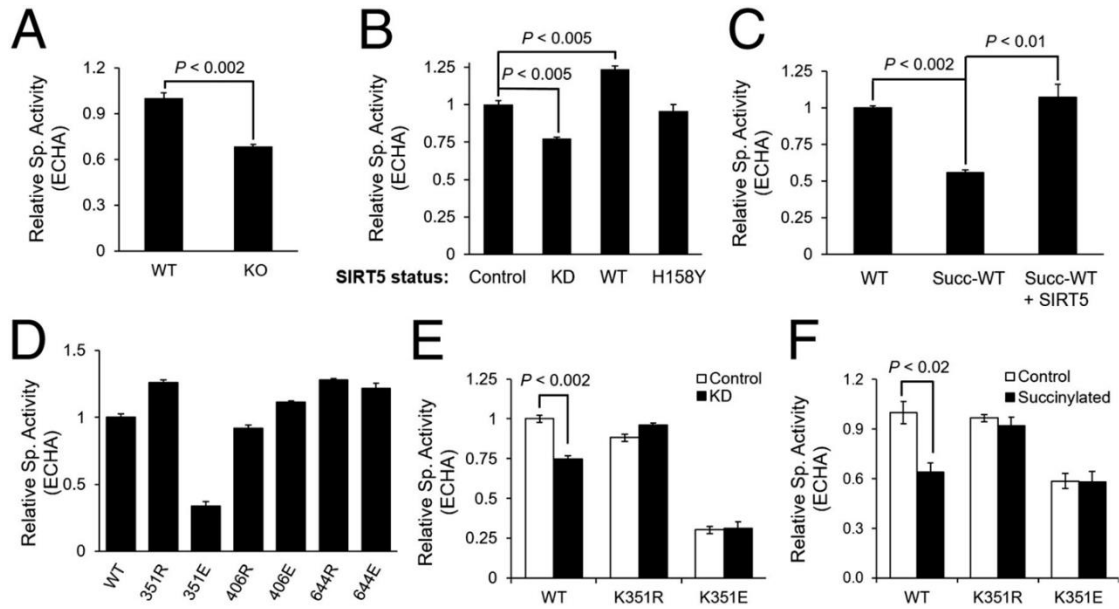


Figure B.6 SIRT5 increases ECHA activity by desuccinylation. (A) ECHA activity was higher in *Sirt5* WT mouse hearts than in *Sirt5* KO mice. (B) Flag-ECHA expressed in HEK-293T control, *Sirt5* KD, and SIRT5 (WT or H158Y) overexpressing cells showed activities consistent with the hypothesis that SIRT5 increases ECHA activity by desuccinylation. (C) Recombinant ECHA and ECHB (co-expressed and purified in *E. coli*) could be nonenzymatically succinylated, which decreased the ECHA activity. Incubation with SIRT5 and NAD restored ECHA activity. (D) K351 is the only residue that decreases ECHA activity when mutated to E. (E) Neither K351R nor K351E show any change in activity when purified from HEK-293T control or *Sirt5* KD cells. (F) Unlike WT, K351R and K351E mutant ECHA does not lose any additional activity when incubated with succinyl-CoA. Data shown as mean \pm SEM, $n = 3$.

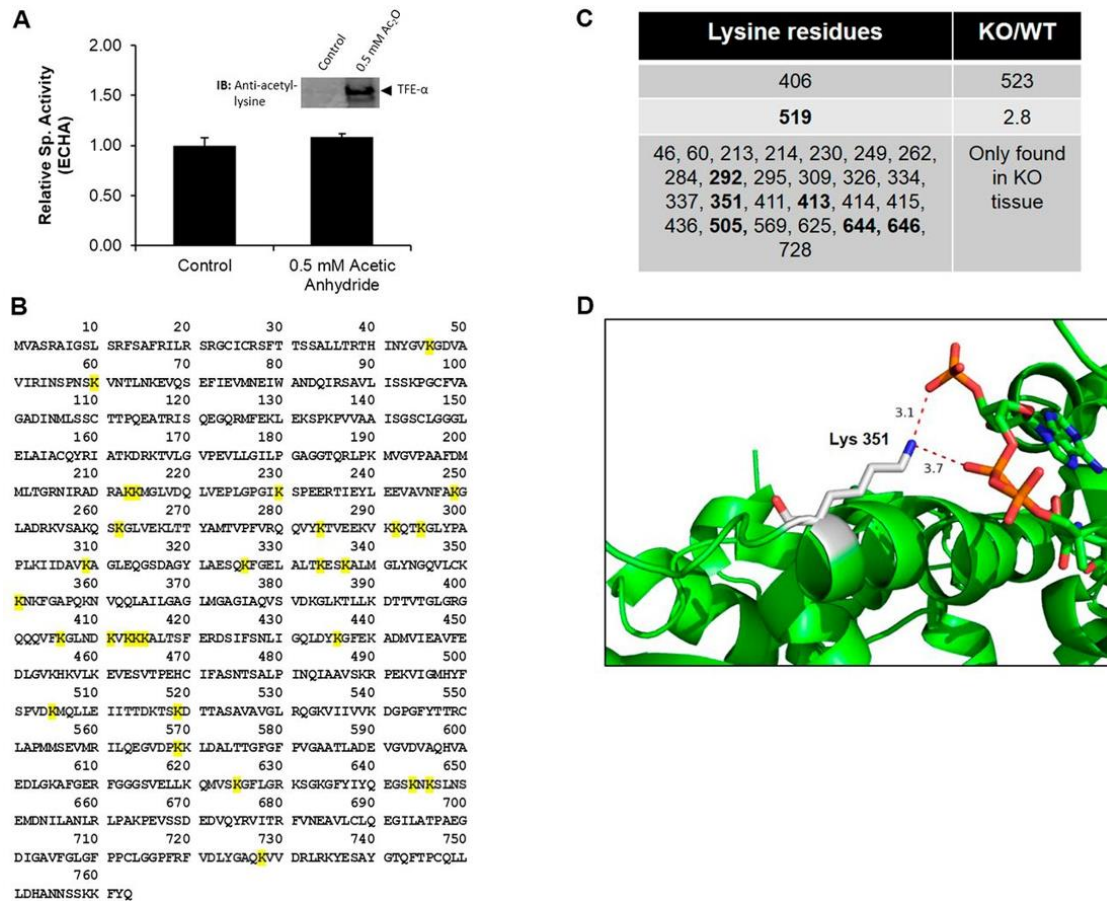


Figure B.7 Recombinant ECHA and ECHB complex was nonenzymatically acetylated with 0.5 mM acetic anhydride for 15 min at room temperature. (A) Recombinant ECHA and ECHB complex was nonenzymatically acetylated with 0.5 mM acetic anhydride for 15 min at room temperature. Data are shown as mean \pm SEM, $n = 3$. ECHA did not show any significant change in activity after chemical acetylation. (Inset) Western blot against anti-acetyllysine antibody shows acetylation on ECHA after treating with 0.5 mM acetic anhydride. (B) Succinylated lysine residues of ECHA identified from our proteomics analysis are highlighted in yellow. (C) Fold change of succinyl-lysine-containing peptides (KO/WT) calculated from the peak area of the peptides. (D) The interactions between Lys351 ϵ -N (denoted by blue) and the negatively charged CoA phosphate groups (oxygen is denoted by red) are shown in the X-ray crystal structure of *M. tuberculosis* ECHA in complex with free CoA bound at the hydratase active sites (PDB ID code 4B3J). The figure was generated using PyMOL. Sequence alignment of ECHA showed Lys351 in mice is aligned with Ala-312 in *M. tuberculosis*. Hence, Ala-312 in ECHA of *M. tuberculosis* was mutated to Lys using PyMOL.

Lys351 Is the Major Succinylation Site of ECHA That Regulates Its Activity

To elucidate which of the 28 succinyllysine residues (**Fig. B.7B and C**) identified on mouse ECHA down-regulates its enzymatic activity, we examined the crystal structure of a homologous ECHA from *Mycobacterium tuberculosis* in complex with free CoA bound at the ECH active site²⁸. The crystal structure shows that several lysine residues (K351, K406, and K644) targeted by SIRT5 are present at the interface between ECHA and ECHB or are close to the bound CoA in the ECH site. For example, K351 is very close to the bound CoA (the distance between the ϵ -N of K351 and the phosphate of CoA is less than 4 Å) and hence the succinylation on K351 could disrupt the interaction between ECHA and CoA (**Fig. B.7D**). To test the effect of succinylation of these lysine residues (K351, K406, and K644) on ECHA activity, we expressed Flag-tagged ECHA WT, K-to-R mutants (mimicking the desuccinylated state) or K-to-E mutants (mimicking the negatively charged succinyllysine modification) in HEK-293T and carried out enzymatic activity assays after immunoprecipitation. Whereas all of the K-to-R mutants maintained basal activity, only K351E showed a significant loss (more than 70%) in ECHA enzymatic activity compared with the WT (**Fig. B.6D**). These data identify Lys351 as a critical lysine residue for the regulation of ECHA enzymatic activity.

We further checked the enzymatic activity of K351R and K351E mutants immunopurified from HEK-293T control and *Sirt5* KD cells. Whereas WT ECHA from *Sirt5* KD cells showed a decrease in activity compared with that from control KD cells, neither K351R nor K351E showed any difference in enzymatic activity in control and *Sirt5* KD cells (**Fig. B.6E**). We also showed that upon chemical succinylation with

succinyl-CoA, K351R and K351E ECHA did not lose additional activity (**Fig. B.6F**). Thus, our mutational data suggest that SIRT5 regulates ECHA enzymatic activity mainly through desuccinylation of Lys351.

Absence of SIRT5 Resulted in Reduced Fatty Acid Oxidation and Accumulation of Long-Chain Fatty Acyl-CoAs

We wanted to determine the consequence of decreased ECHA enzymatic activity due to succinylation on the level of long-chain fatty acyl-CoAs in the heart. Defective ECHA would significantly slow down the β -oxidation of long-chain fatty acids, leading to accumulation of long-chain acyl-CoAs. Indeed, after 30 min of endurance exercise, long-chain acyl-CoA levels were elevated in the KO heart compared with the WT (**Fig. B.8A**). Significant accumulation of long-chain acyl-CoAs in the heart was also observed in *Sirt5* KO mice that were fasted for 24 hr (**Fig. B.9A**). *Sirt5* KO heart also showed an accumulation of odd-chain fatty acyl-CoA with a chain length higher than 11 but not the shorter ones (**Fig. B.9B**). The data suggest that the loss in ECHA activity in *Sirt5* KO heart also slows down the odd-chain fatty acid oxidation. Endurance exercise or fasting forces the mice to use β -oxidation to get the necessary energy and therefore requires optimal ECHA activity. Our data suggest that succinylation impairs fatty acid oxidation through down-regulation of ECHA activity. Hence, SIRT5 is important to maintain efficient fatty acid oxidation in the heart during energy-demanding situations such as fasting and exercise. In addition, fatty acid oxidation, measured in permeabilized heart tissues from *Sirt5* WT and KO mice, was clearly reduced in *Sirt5* KO mice (**Fig. B.8B**). Our findings are in agreement with the previous report of reduced fatty acid oxidation and accumulation of acylcarnitines in

Sirt5 KO liver and muscles¹⁸.

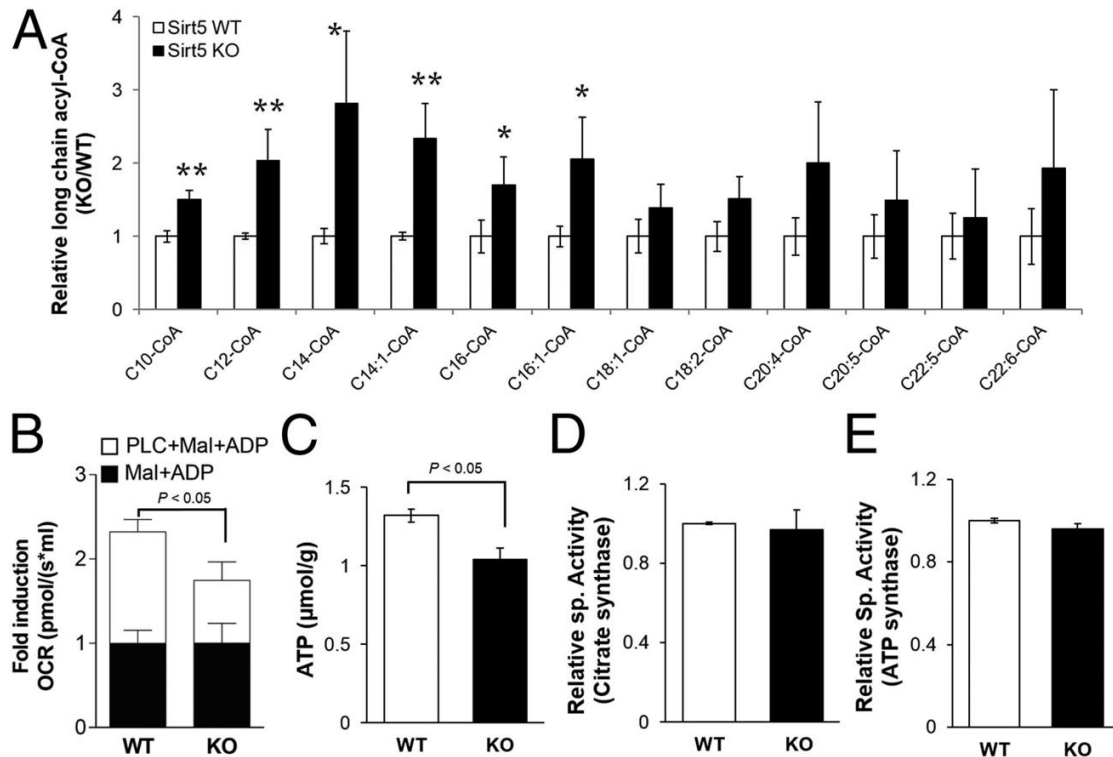


Figure B.8 SIRT5 deficiency leads to accumulation of long-chain CoAs and decreased cardiac ATP levels. (A) Relative levels of long-chain CoA thioesters in *Sirt5* KO hearts compared with WT (after 30 min of exercise, ** $P < 0.05$, * $P < 0.1$). (B) Normalized fatty acid oxidation was significantly reduced in permeabilized *Sirt5* KO heart tissue. Mitochondrial respiration in response to palmitoyl-l-carnitine (PLC) was monitored. Malate (2 mM) and ADP (2.5 mM) were used as a pre-treatment. (C) Cardiac ATP levels were measured in *Sirt5* WT and KO mice after 24 hr of fasting. (D) Enzymatic activity of citrate synthase was measured in heart extracts from *Sirt5* WT and KO mice. (E) Complex V activities were measured from *Sirt5* WT and KO mice heart mitochondria. All data shown as mean \pm SEM, $n = 3$ per genotype.

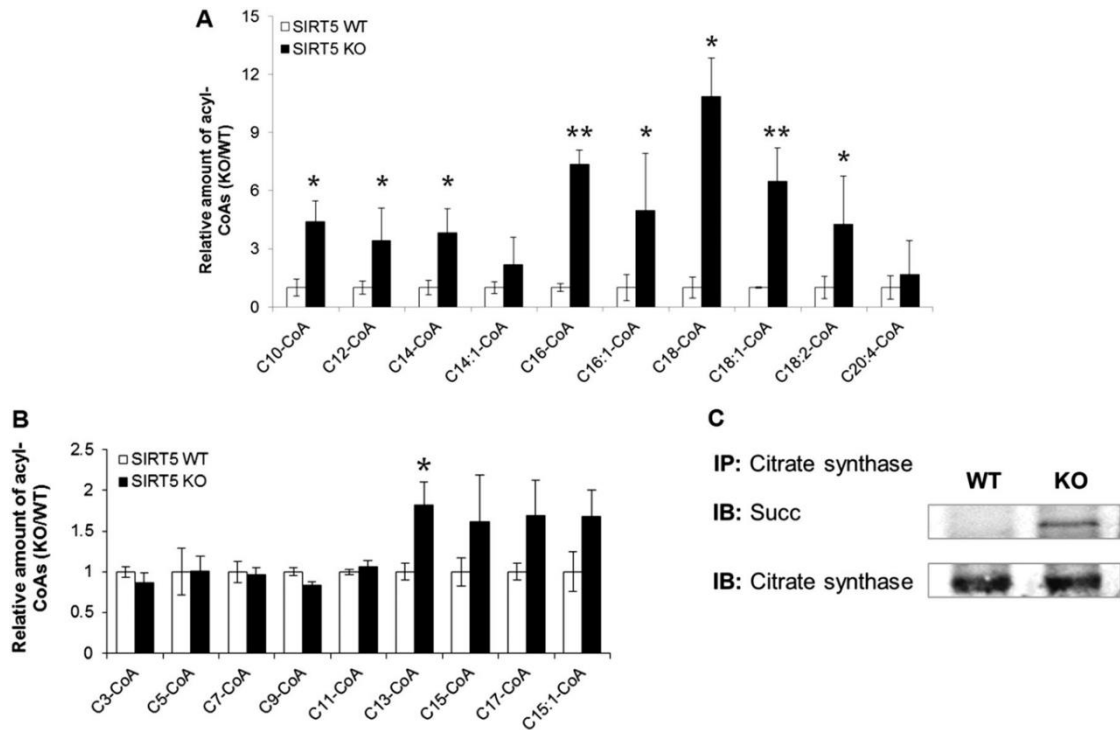


Figure B.9 Relative level of long-chain CoA thioesters in *Sirt5* KO hearts compared with WT after 24 hr of fasting. (A) Relative level of long-chain CoA thioesters in *Sirt5* KO hearts compared with WT after 24 hr of fasting (mean \pm SEM, $n = 3$ per genotype, $**P < 0.05$, $*P < 0.1$). **(B)** Relative level of odd-chain acyl-CoAs in *Sirt5* KO hearts compared with WT after 30 min of exercise (mean \pm SEM, $n = 3$ per genotype, $*P < 0.1$). **(C)** Citrate synthase from *Sirt5* KO mouse heart had increased succinylation.

Lack of SIRT5 Results in Lower Cardiac ATP Levels.

To further test the hypothesis that the regulation of ECHA by SIRT5 is important for cardiac energy production, we measured ATP levels in *Sirt5* WT and KO hearts. As would be expected in the case of defective fatty acid oxidation, we observed more than 20% reduction in ATP in *Sirt5* KO heart compared with WT (**Fig. B.8C**). Other metabolic enzymes regulated by SIRT5 might also contribute to the decreased ATP production in *Sirt5* KO hearts. For example, citrate synthase controls the flow of acetyl-CoA into the TCA cycle and any loss in its activity might also contribute to the observed decrease of fatty acid oxidation. To test this possibility, we measured the enzymatic

activity of citrate synthase from *Sirt5* WT and KO heart lysates and found that WT and KO heart had comparable citrate synthase activities despite citrate synthase being hypersuccinylated in KO heart (**Fig. B.8D and Fig. B.9C**). Another likely candidate for reduced ATP level in *Sirt5* KO heart is ATP synthase, which was found to be hypersuccinylated in the proteomics study. However, we did not observe any significant change in ATP synthase (complex V) activity in *Sirt5* WT and KO heart (**Fig. B.8E**). These data support the conclusion that the observed succinylation-induced fatty acid oxidation deficit is mainly driven by the regulation of ECHA.

SIRT5 KO Mice Exhibit Reduced Cardiac Function and Develop Hypertrophic Cardiomyopathy with Aging

The heart has a very rapid and dynamic rate of ATP consumption²⁹, and hence a constant supply of ATP is necessary to keep the heart working properly. Lower cardiac ATP content might decrease the ability of *Sirt5* KO mice to effectively convert the chemical energy to contractile work³⁰. Fatty acid is a major energy source used to sustain contractile function in the heart, and thus a decrease in fatty acid metabolism might result in heart dysfunction. To further explore cardiac function in *Sirt5* WT and KO mice, we performed echocardiography on mice at 8 weeks of age after overnight fasting. Both the shortening fraction and ejection fraction were reduced in young adult *Sirt5* KO mice, indicating reduced cardiac function in the absence of SIRT5 (**Fig. B.10A and B and Fig. B.11**). To see whether the cardiac phenotype becomes more prominent upon aging, we also recorded echocardiographic parameters in 39-week-old mice. The older *Sirt5* KO mice showed hallmarks of hypertrophic cardiomyopathy, such as significantly increased heart weight (normalized to body weight) and left ventricular

mass (normalized to body weight) along with reduced shortening fraction and ejection fraction (**Fig. B.10C–G and Fig. B.12A–I**). Hematoxylin and Eosin (H&E) staining and quantification of cardiomyocyte cross-sectional area shows evidence of cardiac hypertrophy in the *Sirt5* KO mice (**Fig. B.10H and I and Fig. B.12J**). Furthermore, there was evidence of fibrosis (Masson's trichrome staining, **Fig. B.10J**) and macrophage infiltration (F4/80 staining, **Fig. B.12K**) in *Sirt5* KO hearts. In addition, well-known markers for cardiomyopathy, such as smooth muscle myosin (SMM) and atrial natriuretic peptide (ANP) levels (**Fig. B.10K**), were robustly induced in *Sirt5* KO hearts. Finally, to rule out the possibility that the hypertrophic cardiomyopathy in *Sirt5* KO mice was caused by a developmental defect, we monitored the hearts of neonatal *Sirt5* WT and KO pups. In *Sirt5* KO pups, heart weight was normal (**Fig. B.12L**). Moreover, we failed to discover an induction of the transcript levels of the cardiomyopathy markers *Smm* and *Anp* in the hearts of *Sirt5* KO pups at 2 days of age (**Fig. B.12M**). Thus, the hypertrophic cardiomyopathy in *Sirt5* KO mice was not caused by a developmental defect.

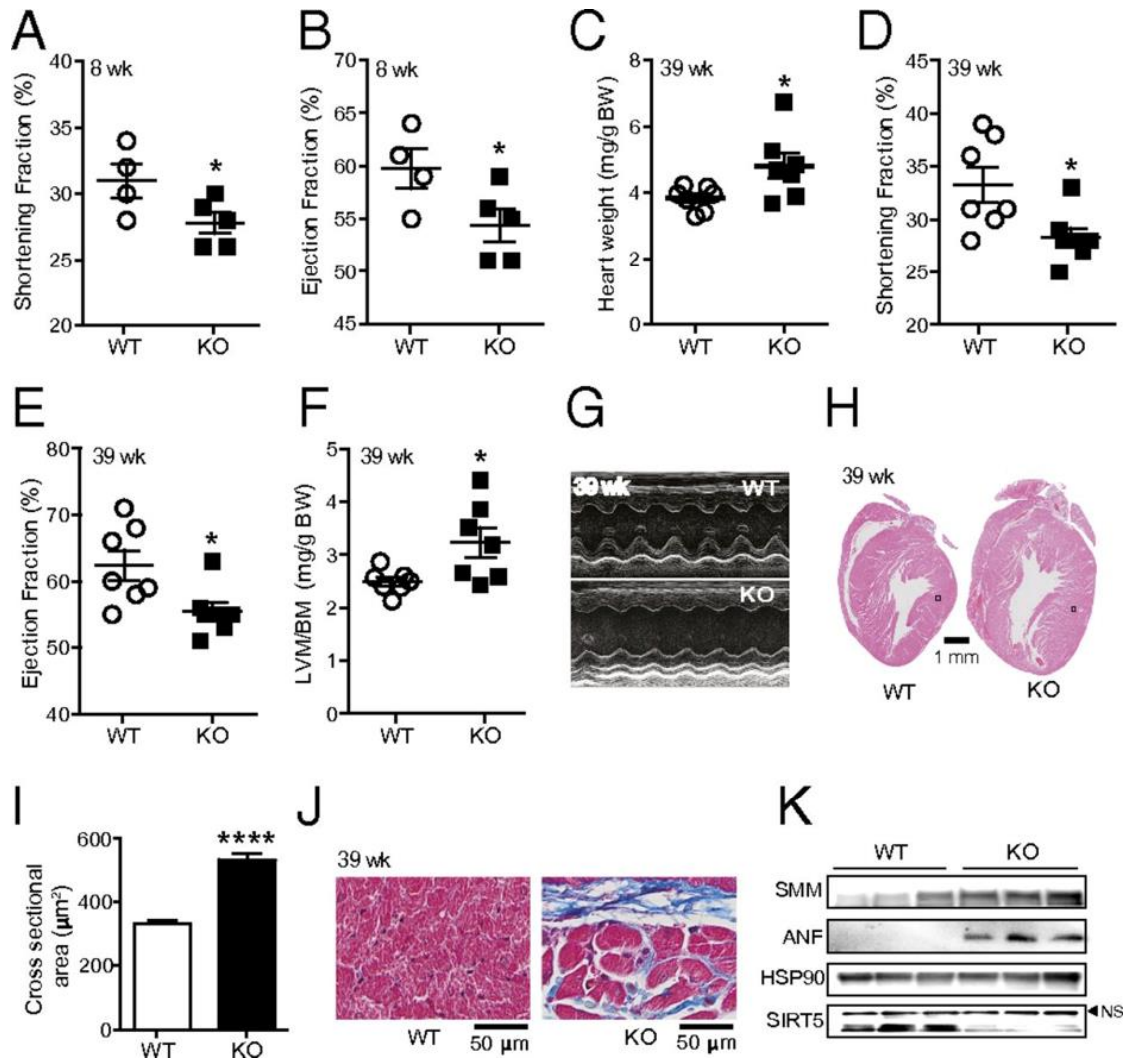


Figure B.10 SIRT5 deficiency causes hypertrophic cardiomyopathy. (A) Shortening fraction and (B) ejection fraction were reduced in *Sirt5* KO mice ($n = 4$ and 5 for *Sirt5* WT and KO respectively, 8-week-old males). (C) Normalized heart weight of *Sirt5* WT and KO male mice ($n = 7$ per genotype). (D) The shortening fraction, and (E) ejection fraction were significantly reduced whereas (F) left ventricular mass to body mass (LVM/BM) was significantly increased in hearts of *Sirt5* KO mice. (G) Representative M-mode images of echocardiography showing cardiac dysfunction in *Sirt5* KO mice. (H) H&E staining of heart cross-sections and (I) quantification of cardiomyocytes cross-sectional areas ($n = 100$ per genotype), showing cardiac hypertrophy in the *Sirt5* KO mice. The two black boxes in H indicate the localization of the images that are shown in larger magnification in Fig. B.12J. (J) Masson's trichrome stain in cross-sections of the heart showing increased fibrosis in *Sirt5* KO hearts. (K) Evaluation of SMM, ANF, HSP90, and SIRT5 protein levels in *Sirt5* WT and KO mouse hearts. Experiments in C–J were performed with hearts of 39-week-old male mice. All graphs shown as mean \pm SEM, * $P < 0.05$, **** $P < 0.0001$.

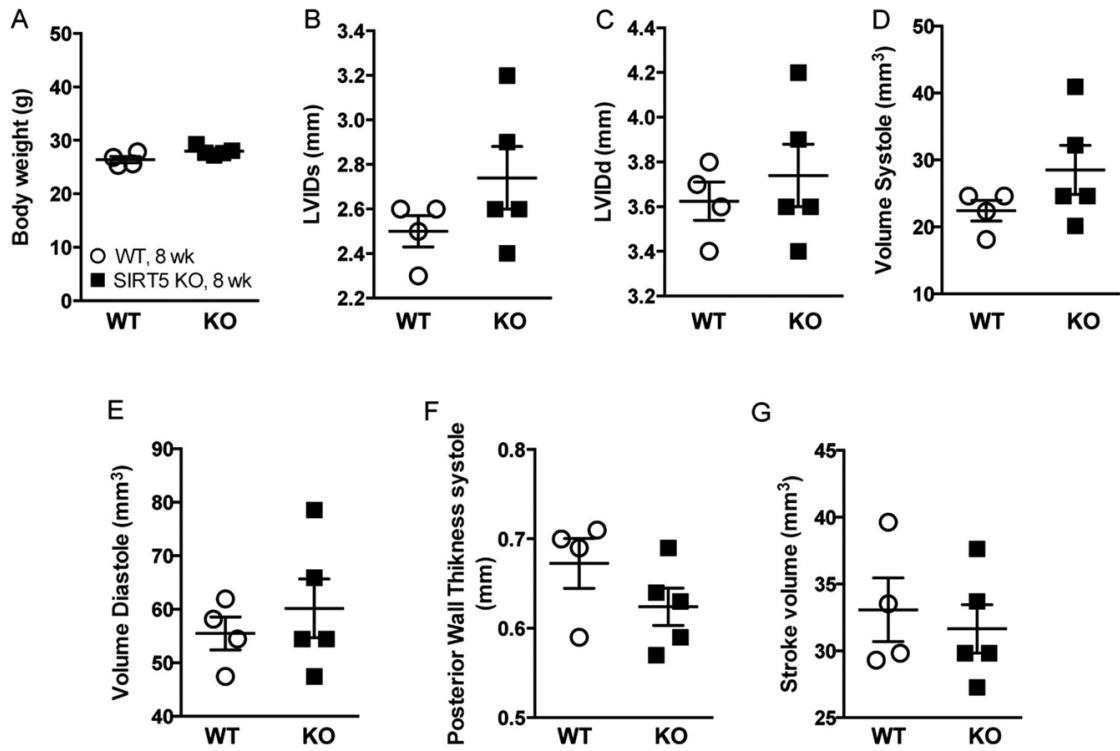


Figure B.11 Body weight of *Sirt5* WT and KO male mice (8-week-old males) (A) Body weight of *Sirt5* WT and KO male mice ($n = 4-5$ per genotype, 8-week-old males). (B) Left ventricular internal dimension in systole (LVIDs), (C) left ventricular internal dimension in diastole (LVIDd), (D) volume in systole, (E) volume in diastole, (F) posterior wall thickness, and (G) stroke volume did not altered significantly in *Sirt5* KO male mice. All graphs are shown as mean \pm SEM.

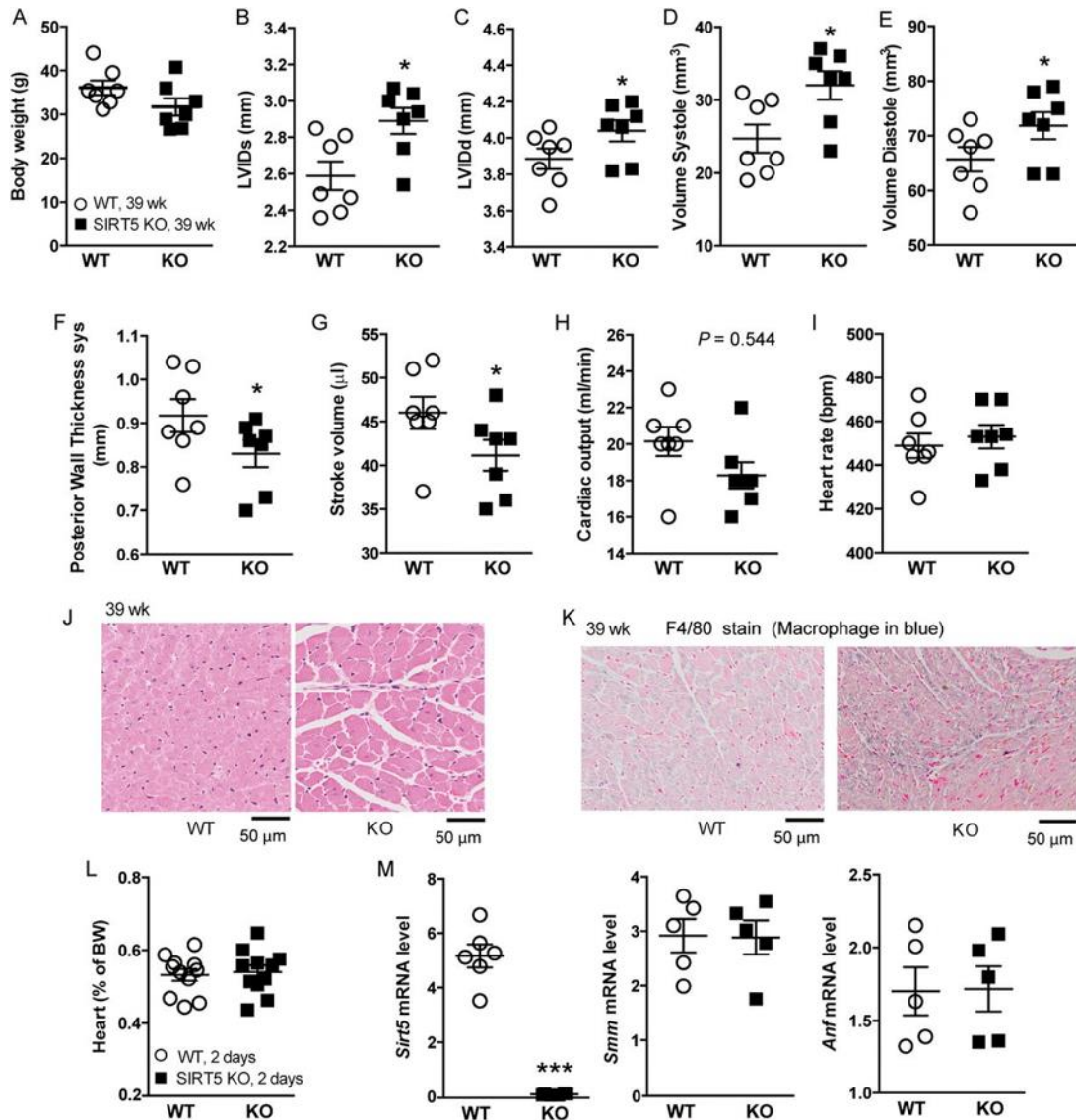


Figure B.12 Body weight of *Sirt5* WT and KO male mice (39-week-old males). (A) Body weight of *Sirt5* WT and KO male mice ($n = 7$ per genotype, 39-week-old males). (B) Left ventricular internal dimension in systole (LVIDs), (C) left ventricular internal dimension in diastole (LVIDd) and (D) volume in systole and (E) diastole were significantly increased whereas (F) posterior wall thickness, (G) stroke volume and (H) cardiac output were reduced in *Sirt5* KO male mice. (I) Heart rate did not show clear differences between the genotypes. (J) Representative zoomed-in (black boxes in Fig. B.10H) image of H&E staining of heart cross-sections (39-week-old males). (K) F4/80 staining in cross-sectional heart showing increased macrophage infiltration in *Sirt5* KO heart (39-week-old males). (L) Normalized heart weight of WT and *Sirt5* KO pups ($n = 11$ per genotypes, 2-d-old pups) does not show any difference. (M) mRNA levels of *Sirt5*, *Smm*, and *Anf* as markers of cardiac dysfunction were evaluated by qRT-PCR ($n = 5$ per genotype, 2-d-old pups). All graphs are shown as mean \pm SEM, *** $P < 0.001$, * $P < 0.05$.

Discussion

Sirtuins were originally thought to be NAD-dependent protein lysine deacetylases³¹. The lack of efficient deacetylation activity for SIRT4–7 prompted studies that led to the discovery that SIRT5 is an efficient desuccinylase, demalonylase^{1,17} and deglutarylase⁸. This finding also opened up directions to discover novel activities for other sirtuins^{7,9}. Finding the desuccinylase and demalonylase activity of SIRT5 also led to the identification of lysine succinylation and malonylation as common PTMs^{1,4,16-19,32}. Proteomic studies have identified about 1,000 proteins that are succinylated and regulated by SIRT5^{16,18,19}. Despite these studies, the biological significance of lysine succinylation and SIRT5 remains unclear. *Sirt5* KO mice only display subtle changes in physiology and seem normal under basal conditions regardless of elevated ammonia levels²². In our study, we used targeted metabolomics to profile acyl-CoA distributions in different tissues. Interestingly, the metabolomics data show that succinyl-CoA is the most abundant short-chain acyl-CoA in the mouse heart. The heart needs a constant energy supply to sustain the mechanical pumping and thus may need to optimize metabolism to favor the TCA cycle and oxidative phosphorylation, which may lead to a higher succinyl-CoA concentration. Regardless of what exactly causes this interesting acyl-CoA profile, the results we obtained suggest that different tissues have very different metabolism and that it is worthwhile to examine the function of acylation in different tissues.

The unique acyl-CoA profiling results then led us to examine succinylation in different mouse tissues with and without SIRT5. Interestingly, succinylation increases most dramatically in the heart when *Sirt5* is deleted, which suggests that SIRT5 may

have important functions in the heart. Consistent with this, SIRT5 level is higher in the heart than in other mouse tissues tested. *Sirt5* KO mice exhibit a reduced cardiac function and display signs of cardiomyopathy upon aging. Thus, protein succinylation and SIRT5 exert important roles in cardiac function. To understand the molecular mechanism underlying the function of succinylation and SIRT5 in the heart, we have identified over a hundred proteins with increased lysine succinylation in *Sirt5* KO heart using semiquantitative proteomics. Among the proteins we identified, ECHA has the highest number of lysine succinylation sites. SIRT5 activates ECHA by desuccinylating it. Consistent with ECHA being inhibited by succinylation, *Sirt5* KO hearts have compromised long-chain fatty acid oxidation along with a decreased ATP levels. We believe that the inhibition of the fatty acid oxidation pathway is the major contributor to the reduced ATP production because several lines of evidence suggest that neither the TCA cycle nor ATP synthase is inhibited by *Sirt5* deletion.

Succinylation is a widespread PTM and affects major metabolic pathways including amino acid metabolism, the TCA cycle, fatty acid metabolism, oxidative phosphorylation, urea cycle, ketogenesis, and so on. SIRT5 can either activate or repress enzymatic activity via desuccinylation. SIRT5 is reported¹⁸ to up-regulate hepatic ketogenesis through activation of 3-hydroxy-3-methylglutaryl-CoA synthase 2. There are reduced fatty acid oxidation and accumulation of medium- and long-chain acylcarnitines in *Sirt5*-deficient mouse liver and muscle, but the underlying mechanism was not investigated. In our current study, we show that SIRT5 positively modulates fatty acid oxidation in the mouse heart. In addition, we demonstrate that succinylation impairs fatty acid oxidation through down-regulation of ECHA activity. Altogether, this

suggests that SIRT5 plays a critical role in regulating fatty acid metabolism in multiple tissues.

Although many of the substrate proteins that we identified here were also previously reported^{16,18,19}, the uniqueness of the current study is that for the first time to our knowledge we have connected lysine succinylation and SIRT5 to an important physiological function (i.e., the regulation of heart metabolism and function). This function likely underlies the impaired performance in an endurance run test reported earlier²¹. In recent years, significant advances have been made on the role of fatty acid metabolism defects in the pathogenesis of cardiomyopathy. Fatty acid oxidation provides most of the energy required by the heart. In 1939, Herrmann and Decherd³³ proposed the energy-starvation hypothesis, which stated that deprivation of cardiac energy could lead to heart failure. Cardiomyopathy can occur in a broad range of pathological conditions. It is well documented that defects or disorders of fatty acid metabolism often lead to cardiomyopathy³⁴⁻³⁶. Cardiomyopathy is a major symptom of inborn errors in fatty acid metabolism, such as malonyl-CoA decarboxylase deficiency, carnitine palmitoyl transferase 2 deficiency, medium-chain acyl-CoA dehydrogenase deficiency, and mitochondrial trifunctional protein (MTP) deficiency³⁷. A mutation of the *Hadha* gene, which encodes ECHA protein, leads to MTP deficiency with cardiac symptoms³⁸. In the present study, we have established that SIRT5 deficiency leads to decreased ECHA activity and deficiency in cardiac energy metabolism, and ultimately cardiomyopathy. Very recently, Boylston et al.³⁹ have showed that *Sirt5* KO mice are more susceptible to ischemia-reperfusion injury compared with WT.

Connecting lysine succinylation and SIRT5 to heart function was made possible

by the targeted metabolomics analysis of acyl-CoA concentrations in various mouse tissues. In the last decade, many novel PTMs have been reported, including propionylation, butyrylation, crotonylation, glutarylation⁸, long-chain fatty acylation^{7,9}, and 2-hydroxyisobutyrylation⁶. All these PTMs likely result from reactions with cellular metabolites either via specific acyltransferases or via non-enzymatic pathways, similar to lysine succinylation^{40,41}. Although our studies with ECHA suggest that chemical succinylation and SIRT5-catalyzed desuccinylation *in vitro* is able to recapitulate the effects of succinylation and desuccinylation on ECHA *in vivo*, protein-catalyzed succinylation cannot be completely ruled out. Regardless of the enzymatic or nonenzymatic nature of lysine acylation, our study here suggests that combining metabolomics of acyl-CoAs and proteomic identification of substrate proteins in different tissues is useful to understand the functions of these newly identified PTMs.

Materials and Methods

Reagents:

Mouse monoclonal anti-Flag M2 antibody conjugated with horseradish peroxidase, anti-Flag M2 affinity gel, *d*₆-acetic anhydride, acyl-CoA standards, ammonium formate, and 2-(2-pyridyl)ethyl silica gel were purchased from Sigma-Aldrich. The rabbit pan-specific anti-acetyllysine was purchased from ImmuneChem Pharmaceuticals, Inc. Rabbit pan-specific anti-succinyllysine (PTM-401) and anti-glutaryllysine (PTM-1151) antibodies were purchased from PTM Biolab, Inc., respectively. The mouse monoclonal antibody against V5 tag (46-0705) was purchased from Life Technologies. The ECHA antibody (sc-292195), protein A/G PLUS-agarose

(sc-2003), citrate synthase antibody (sc-390693), and goat anti-rabbit/mouse IgG conjugated with HRP (sc-2004) were purchased from Santa Cruz Biotechnology. The SIRT5 rabbit monoclonal antibody (8782) was purchased from Cell Signaling. The 2-(*E*)-decenoic acid was purchased from MP Biomedicals. Octyl- β -D-glucopyranoside was purchased from Chem-Impex International, Inc. Ni-NTA agarose was purchased from Qiagen.

Synthesis of d_3 -Acetyl-CoA As the Internal Standard

d_3 -Acetyl-CoA was synthesized according to the method reported by Dils and Carey⁴². Briefly, 15 mg of CoA was dissolved in ice-cooled 2 mL of 0.1 M KHCO₃. d_6 -Acetic anhydride (40 μ L) was added into the mixture and incubated at 4 °C. After 30 min, the reaction mixture was acidified with 0.1 M HCl to adjust the pH to \sim 2. No free CoA was detected in the crude reaction mixture based on LC-MS analysis. The crude reaction mixture was further purified by reverse-phase HPLC using Beckman Coulter System Gold 125p Solvent Module and 168 detector with a TARGA C18 column (250 \times 20 mm i.d., 10 μ m; Higgins Analytical, Inc.) monitoring at 215 and 260 nm. For the purification, solvent A was 5 mM ammonium acetate (pH 5.3), solvent B was 40% acetonitrile in water, and the following gradient was used: a linear gradient of 0–20% solvent B over 5 min, then a linear gradient of 20–50% solvent B over 25 min, and finally 50% solvent B for 5 min before equilibrating the column back to 0% solvent B over 10 min at a flow rate of 8 mL/min. The purified fractions were then lyophilized and analyzed by LC-MS. Calculated m/z of d_3 -acetyl-CoA for C₂₃H₃₆D₃N₇O₁₇P₃S ([M+H]⁺) was 813.60, found 813.33.

LC-MS analysis was performed on a Shimadzu HPLC LC20-AD and Thermo

Scientific LCQ Fleet with a Sprite TARGA C18 column (40 × 2.1 mm i.d., 5 μm; Higgins Analytical, Inc.) monitoring at 215 (detector 1 channel A) and 260 nm (detector 1 channel B) with positive/negative mode for mass detection. Solvents used for LC-MS analysis were water with 0.1% acetic acid (solvent A) and acetonitrile with 0.1% acetic acid (solvent B). Acyl-CoA was eluted at a flow rate of 0.3 mL/min with 0% solvent B for 2 min, followed by a linear gradient of 0–10% solvent B over 2 min, followed by a linear gradient of 10–100% solvent B over 5 min, and finally 100% solvent B for 2 min before equilibrating the column back to 0% solvent B over 4 min.

Preparation of Acyl-CoA Standards

One hundred micromolar stock solution for the standard acyl-CoA esters in Milli-Q water with 100 mM ammonium formate, pH 5.0, was made by measuring the absorbance at 260 nm ($\epsilon = 16,400 \text{ mM}^{-1}\cdot\text{cm}^{-1}$). To prepare standard curves, equal concentrations of standard acyl-CoAs of interest were mixed, creating a master mix, and we performed twofold serial dilutions in Milli-Q water with 100 mM ammonium formate, pH 5.0. d_3 -Acetyl-CoA was used as the internal standard.

Extraction of Short-Chain Acyl-CoAs from Different Tissues

All of the extraction solutions, buffers, and solvents used for the CoA extraction were precooled on ice. Powder frozen mice tissues (~50 mg), spiked with 0.6 nmol of d_3 -acetyl-CoA as internal standard, were homogenized with 3 mL of methanol/water (1:1) containing 5% acetic acid (extraction buffer) using a Dounce homogenizer (25 strokes) on ice. The tissue homogenates were centrifuged at $20,000 \times g$ for 15 min at 4 °C. The clear supernatant was loaded on a 3-mL ion exchange cartridge packed with 100 mg of 2-(pyridyl)ethyl silica gel. The cartridge had been preactivated with 3 mL

of methanol and then with 3 mL of extraction buffer. The ion exchange resin was washed with 2 mL of extraction buffer to remove unbound metabolites. The acyl-CoAs trapped on the silica gel cartridge were eluted with 2 mL of methanol/250 mM ammonium formate (4:1). The combined effluent was dried with nitrogen gas and stored at $-80\text{ }^{\circ}\text{C}$ until LC-MS analysis.

Extraction of Long-Chain Acyl-CoAs from Heart Tissues

All of the extraction solutions and solvents used for the CoA extraction were precooled on ice. Powder frozen heart tissues ($\sim 20\text{ mg}$) were homogenized with 0.5 mL of methanol/water 4:1 using an electronic mixer for 30 sec on ice. The tissue homogenates were centrifuged at $20,000 \times g$ for 15 min at $4\text{ }^{\circ}\text{C}$. The clear supernatant was dried in a SpeedVac. The dried residue was stored at $-80\text{ }^{\circ}\text{C}$ until LC-MS analysis.

Absolute Quantitation of ATP

ATP content in *Sirt5* WT and KO heart tissues was measured using a colorimetric assay following the protocol of the ATP assay kit (Abcam).

Sample Reconstitution for LC-MS Analysis

Dried tissue extract was dissolved into either water with 50 mM ammonium acetate (pH 6.8, short-chain acyl-CoA) or 50 mM ammonium acetate with 20% (vol/vol) acetonitrile (pH 6.8, long-chain acyl-CoA). Samples were centrifuged at $20,000 \times g$ at $4\text{ }^{\circ}\text{C}$ for 3 min and the supernatant was transferred to LC vials. The injection volume was 12 μL .

HPLC Method

An Ultimate 3000 UHPLC (Dionex) was coupled to a Q-Exactive mass spectrometer (QE-MS; Thermo Scientific) for metabolite separation and detection. For

acyl-CoA analysis, a reverse-phase liquid chromatography method was used. A Luna C18 column (100 × 2.0 mm i.d., 3 μm; Phenomenex) was used. For short-chain acyl-CoA, the solvent A was water with 5 mM ammonium acetate (pH 6.8), and solvent B was methanol. The linear gradient was as follows: 0 min, 2% solvent B; 1.5 min, 2% solvent B; 3 min, 15% solvent B; 5.5 min, 95% solvent B; 14.5 min, 95% solvent B; 15 min, 2% solvent B; and 20 min, 2% solvent B. For long-chain acyl-CoA, solvent A was water with 10 mM ammonium acetate (pH 8.5, adjusted with 10 N ammonium hydroxide), and solvent B was acetonitrile. The linear gradient was as follows: 0 min, 20% solvent B; 1.5 min, 20% solvent B; 5 min, 95% solvent B; 14.5 min, 95% solvent B; 15 min, 20% solvent B; and 20 min, 20% solvent B. The column temperature was room temperature.

MS Method

The QE-MS was equipped with a heated electrospray ionization (HESI) probe, and the relevant parameters were as follows: heater temperature, 120 °C; sheath gas, 30 psi; auxiliary gas, 10 psi; sweep gas, 3 psi; and spray voltage, 3.6 kV for positive mode. The capillary temperature was set at 320 °C, and the S-lens was 55. A full scan range was set at 300–1,500 (*m/z*). The resolution was set at 70,000 (at *m/z* 200). The maximum injection time was 200 ms. The automated gain control was targeted at 3×10^6 ions.

Data Analysis

Raw data collected from LC-QE-MS were processed on Thermo Scientific software Sieve 2.0. Peak alignment and detection were performed according to manufacturer protocols. For a targeted metabolomics analysis, a frameseed including acyl-CoA metabolites that had been previously validated was used for targeted

metabolites analysis with data collected in positive mode; m/z width was set at 8 ppm.

Dimethyl Labeling of Heart Protein Extracts

Hearts were collected from *Sirt5* WT and KO male mice at 12 wk of age. The frozen powdered heart tissues were homogenized and lysed using lysis buffer (50 mM Tris·HCl, pH 8.0, 150 mM NaCl, 5 mM nicotinamide, 1% Nonidet P-40, 10% glycerol, and 1% vol/vol protease inhibitor mixture). The lysate was centrifuged at $20,000 \times g$ for 20 min at 4 °C to remove the cell debris. Protein concentration of the supernatant was measured using the Bradford method. One milligram of total protein was taken from *Sirt5* WT and KO samples for tryptic digestion. The protein mixtures were denatured and reduced with 6 M guanidine hydrochloride, 10 mM DTT in 50 mM triethylammonium bicarbonate, pH 8.0, for 1 hr at room temperature. Next, cysteine residues were alkylated by 50 mM iodoacetamide in darkness at room temperature for 1 hr followed by quenching with 1 M DTT (final concentration 50 mM) for 1 hr at room temperature. After proteolytic digestion by trypsin (with trypsin: protein 1:20 wt/wt) for 16 hr at 37 °C, the peptides from *Sirt5* WT and KO samples were separately labeled with heavy and light dimethyl groups, respectively, using an on-column labeling procedure²³. The isotopically labeled peptides were mixed together and lyophilized to powder.

Enrichment of Lysine-Succinylated Peptides

The anti-succinyllysine antibody (40 µg) was immobilized on 40 µL 25% suspension of protein A/G PLUS-agarose beads by incubating at 4 °C for 6 hr. The supernatant was discarded, and the beads were washed three times with NETN buffer (50 mM Tris·HCl, pH 8.0, 100 mM NaCl, 1 mM EDTA, and 0.5% Nonidet P-40). The

lyophilized tryptic peptides obtained above were redissolved in 500 μ L NETN buffer and incubated with the anti-succinyllysine antibody immobilized protein A/G PLUS-agarose beads at 4 °C for overnight with gentle shaking. The beads were washed three times with 1 mL of NETN buffer and three times with ETN (50 mM Tris·HCl, pH 8.0, 100 mM NaCl, and 1 mM EDTA). The bound peptides were eluted by washing three times with 100 μ L of 1% trifluoroacetic acid. The elutions were combined, lyophilized, and cleaned up with C18 ZipTips (Millipore Corp.) according to the manufacturer's instructions before nano LC-MS/MS analysis.

Identification and Quantitation of Dimethyl-Labeled Lysine-Succinylated Peptides by Nano LC-MS/MS Analysis

The tryptic digest was reconstituted in 50 μ L of 2% acetonitrile with 0.5% formic acid (FA) and about 100–200 ng of tryptic digest was injected for nano LC-ESI-MS/MS analysis, which was carried out on a LTQ-Orbitrap Elite mass spectrometer (Thermo-Fisher Scientific) equipped with a CorConneX nano ion source device (CorSolutions LLC). The Orbitrap was interfaced with a Dionex UltiMate3000RSLCnano HPLC system (Thermo/Dionex). The tryptic peptide samples (5 μ L) were injected onto a PepMap C18 trap column-nano Viper (5 μ m, 100 μ m \times 2 cm; Thermo/Dionex) at 20 μ L/min flow rate for on-line desalting and then separated on a PepMap C18 reverse-phase nano column (3 μ m, 75 μ m \times 15 cm; Thermo/Dionex) that was installed in the “plug and play” device with a 10- μ m spray emitter (NewObjective). As described previously⁴³, the peptides were eluted with a 120-min gradient of 5–38% acetonitrile in 0.1% FA at a flow rate of 300 nL/min, followed by a 5-min ramping to 90% acetonitrile in 0.1% FA and a 7-min hold at 90% acetonitrile in

0.1% FA. The column was re-equilibrated with 2% acetonitrile in 0.1% FA for 25 min before the next run. The Orbitrap Elite was operated in positive ion mode with nano spray voltage set at 1.5 kV and source temperature at 250 °C. Instrument calibration was performed using Ultramark 1621 for both Fourier transform (FT) mass analyzer and LTQ mass analyzer along with an additional background ion signal at m/z 445.120025 used as the lock mass for FT mass analyzer.

The instrument was operated in data-dependent acquisition with FT-FT mode using the FT mass analyzer for one survey MS scan of precursor ions followed by MS/MS scans of the top 15 most intense peaks with multiple charged ions above a threshold ion count of 10,000 in a higher-energy collisional dissociation (HCD)-based FT mass analyzer with normalized collision energy of 35%. MS survey scans were set at a resolution of 60,000 (FWHM at m/z 400) for the mass range of m/z 375–1,800 and MS/MS scans at 15,000 resolution for the mass range m/z 100–2,000. Dynamic exclusion parameters were set at repeat count 1 with a 30-sec repeat duration, exclusion list size of 500, 60-sec exclusion duration, and ± 10 ppm exclusion mass width. HCD parameters were set at the following values: isolation width 2.0 m/z , normalized collision energy 35%, activation Q at 0.25, and activation time 0.1 msec. All data were acquired using Xcalibur 2.2 operation software (Thermo-Fisher Scientific).

Data Analysis

All MS and MS/MS raw spectra were processed using Proteome Discoverer 1.4 (PD1.4; Thermo). The mouse RefSeq sequence database was downloaded on April 12, 2012, from NCBI and used for database searches. The database search was performed with two-missed cleavage site by trypsin allowed. The peptide tolerance was set to 10

ppm and MS/MS tolerance was set to 0.1 Da for HCD. A fixed carbamidomethyl modification of cysteine and light dimethyl (+28.031 Da) and heavy dimethyl (+36.076 Da) for any N-terminus was set along with the following variable modifications: methionine oxidation, deamidation on asparagine/glutamine residues, succinylation, and both light/heavy dimethyl on lysine residue. Data filtering parameters were as follows: (i) $\leq 1\%$ FDR, (ii) the peptide spectrum matches (PSMs) with confidence at least high, (iii) the PSMs with delta Cn better than 0.15, and (iv) mass precision $2 \leq$ ppm. All MS/MS spectra for identified succinylated peptides with marginal scores from initial database searching were manually inspected and validated using both PD 1.4 and Xcalibur 2.2 software.

For relatively quantitative analysis of succinylated peptides between high/heavy samples, the peak areas of detected precursor ions at each specific m/z corresponding to the succinylated peptides were generated from the precursor ion-based methyl-duplex algorithm in PD 1.4. The peak area of some important succinylated peptides in raw data files was manually inspected using Xcalibur 2.2 software with mass tolerance at 5 ppm and mass precision at 4 decimal.

Cell Culture and Transfection

HEK 293T cells were cultured in complete DMEM containing glucose and L-glutamine (Invitrogen) supplemented with 10% heat-inactivated FBS (Invitrogen). Cells were transfected using lipofection method (Invitrogen). To make the cDNA library, total RNA was isolated from mouse embryonic fibroblasts (MEFs) using the RNeasy mini kit (Qiagen, 74106) according to the manufacturer's instructions. The isolated total RNA was used for the cDNA synthesis using RT-PCR. Flag-tagged ECHA was PCR-

amplified from MEFs cDNA using TAATGAGCTCATGGTGGCGTCCCGGGCG (forward primer) and TAATCTCGAGTCAC TTATCGTCGTCATCCTTGTAATCCTGGTAGAACTTCTTGCTAGAGTTGTTAG C (reverse primer) and cloned into SacI/XhoI restriction sites of a pCMV vector.

Construction of Plasmids for ECHA Mutants

ECHA lysine-to-arginine and lysine-to-glutamate mutants in a pCMV vector were constructed using a quick-change site-mutagenesis strategy with the primers listed below:

- ECHA K351R:
Forward primer: CAGGTCCTGTGCAAGAGGAATAAATTTGGAGCA
Reverse primer: CTTGCACAGGACCTGGCCGTTATAAAGCCCCAT
- ECHA K351E:
Forward primer: CAGGTCCTGTGCAAGGAGAATAAATTTGGAGCA
Reverse primer: CTTGCACAGGACCTGGCCGTTATAAAGCCCCAT
- ECHA K406R:
Forward primer: CAGCAGCAAGTGTTTCAGGGGGCTGAACGACAA
GGTGAAGAAGAAAGCTCTCACATCA
Reverse primer: GAACACTTGCTGCTGTCCCCGGCCCAGCCCCGT
- ECHA K406E:
Forward primer: CAGCAGCAAGTGTTTCGAGGGGGCTGAACGACAA
GGTGAAGAAGAAAGCTCTCACATCA
Reverse primer: GAACACTTGCTGCTGTCCCCGGCCCAGCCCCGT
- ECHA K644R:

Forward primer: TATCAGGAGGGCTCAAGGAATAAGAGTTTGA
ATTCTGAA

Reverse primer: TGAGCCCTCCTGATAGATGTAAAAGCCCTTCCC

- ECHA K644E:

Forward primer: TATCAGGAGGGCTCAGAGAATAAGAGTTTGAATT
CTGAA

Reverse primer: TGAGCCCTCCTGATAGATGTAAAAGCCCTTCCC

Generation of *Sirt5* Stable KD Cell Lines

Sirt5 shRNA lentiviral plasmids in pLKO.1-puro vector were purchased from Sigma-Aldrich. *Sirt5* shRNA 1 (TRCN0000018544):

CCGGGAGTCCAATTTGTCCAGCTTTCTCGAGAAAGCTGGACAAATTGGACT
CTTTTT and shRNA 2 (TRCN0000018545):

CCGGGCTACGAACAGATTCAGGTTTCTCGAGAAACCTGAATCTGTTCGTAG

CTTTTT were used. After co-transfection of *Sirt5* shRNA plasmid, pCMV- Δ R8.2, and pMD2.G into HEK 293T cells, the medium was collected to infect HEK 293T cells for different experimental purposes. The *Sirt5* KD cells were selected using 1.5 mg/mL puromycin in DMEM complete medium containing glucose and L-glutamine (Invitrogen) supplemented with 10% heat-inactivated FBS (Invitrogen). Cells infected with lentivirus containing control shRNA plasmid were carried out similarly. Knockdown by shRNA 1 was more efficient and data shown in the main text were from *Sirt5* KD cells with shRNA 1.

Synthesis of 2-(*E*)-Decenoyl-CoA

The 2-(*E*)-decenoic acid (8.5 mg, 0.05 mmol) and PyBOP (51.2 mg, 0.1 mmol) were dissolved in 200 μ L THF. CoA (39 mg, 0.05 mmol) and K_2CO_3 (28 mg, 0.2 mmol) were dissolved in 200 μ L of H_2O . The two solutions were mixed and incubated for 2 hr at room temperature with occasional vortexing. After that, the reaction mixture was diluted with 2 mL 1:1 water/MeOH. To purify the 2-(*E*)-decenoyl-CoA, preparative HPLC was performed on a Beckman Coulter System Gold 125p Solvent Module and 168-detector with a TARGA C18 column (250 \times 20 mm, 10 μ m; Higgins Analytical, Inc.) monitoring at 215 and 260 nm. Solvents for HPLC were water with 0.1% trifluoroacetic acid (solvent A) and acetonitrile with 0.1% TFA (solvent B). Acyl-CoA was eluted at a flow rate of 8 mL/min with a linear gradient of 0–100% solvent B over 20 min, and finally 100% solvent B for 10 min before equilibrating the column back to 0% solvent B over 10 min. The purified fractions were then lyophilized and analyzed by LC-MS. The calculated m/z for 2-(*E*)-decenoyl-CoA $C_{31}H_{51}N_7O_{17}P_3S$ ($[M-H]^-$) was 918.76, found 919.11.

Activity Assay of ECHA

As the substrate for the activity assay of ECHA, 2-(*E*)-decenoyl-CoA was used. The combined 2-enoyl-CoA hydratase and 3-hydroxyacyl CoA dehydrogenase activities were measured by monitoring the formation of NADH at 340 nm (absorption coefficient $6,220 M^{-1}\cdot cm^{-1}$) as described previously²⁷. The reaction mixture contained 100 mM Tris·HCl (pH 9.0), 100 mM KCl, 100 μ g/mL BSA, 1 mM free CoA, 120 μ M NAD, and 30 μ M 2-(*E*)-decenoyl-CoA substrate. The reaction was initiated by the addition of 4 μ g of total lysate from heart or the purified Flag-tagged ECHA from one

10-cm tissue culture plate ($\sim 8 \times 10^6$ cells) HEK 293T cells to the reaction mixture. The increasing absorbance at 340 nm was monitored for 10 min using a UV-visible spectrophotometer (Cary 50 UV-visible spectrophotometer; Varian).

Expression and Purification of ECHA and ECHB from E. coli

ECHA and ECHB were PCR-amplified from mouse embryonic fibroblasts cDNA. The following primers were used: TAATCATATGGTGGCGTCCCGGGCG (forward primer for Flag-tagged ECHA), TAATCTCGAGTCACTTATCGTCGTCATCCTTGTAATCCTGGTAGAACTTCTTGCTAGAGTTGTTAGC (reverse primer for Flag-tagged ECHA), TAATGAATTCATGACTACC ATCTTGACTTCCACTTTTAGAAAC (forward primer for His-tagged ECHB), and TAATGTCGACTCATTGTTGGGGTAAGCTTCCACAATCATAGC (reverse primer for His-tagged ECHB). ECHA and ECHB were cloned into NdeI/XhoI and EcoRI/SalI restriction sites of pET-Duet and pET28a, respectively. Sequence-confirmed plasmids were cotransformed and expressed in BL-21 Rosetta cells. Cells were cultured at 37 °C in 4 L of LB media with 100 µg/mL ampicillin, 50 µg/mL kanamycin, and 20 µg/mL chloramphenicol. At an OD₆₀₀ of 0.7, 300 µM isopropyl β-D-1-thiogalactopyranoside was added to induce expression and cells were further incubated at 23 °C overnight. Cells were harvested at $11,325 \times g$ for 8 min and the cell pellet was stored at -80 °C until use. Cells were thawed and then suspended in 100 mM Hepes, pH 8.0, and 1 mM PMSF and then lysed using an EmulsiFlex-C3 cell disruptor (Avestin, Inc.). To the lysate was added octyl β-D-glucopyranoside to a final concentration of 0.8% (wt/vol) and the mixture was incubated for 20 min at 4 °C before centrifuging at $48,384 \times g$ for

30 min using a Beckman Coulter refrigerated floor centrifuge. The soluble fraction was loaded onto a column containing an Ni-NTA agarose. The column was then washed with wash buffer (100 mM Hepes, pH 8.0, 30 mM imidazole, and 0.8% octyl β -D-glucopyranoside) and then a linear gradient of 50–500 mM imidazole in wash buffer was used to elute the protein complex. Fractions containing relatively pure (determined by SDS/PAGE analysis) ECHA and ECHB complex were collected, buffer-exchanged [100 mM Hepes, pH 8.0, 0.8% octyl β -D-glucopyranoside, and 10% (vol/vol) glycerol], concentrated, and stored at -80 °C. All mutants of ECHA were purified similarly.

In Vitro Chemical Succinylation of ECHA and ECHB Complex

In vitro chemical succinylation of ECHA and ECHB complex was achieved by incubating 50 nM *E. coli* purified recombinant complex with 3 mM succinyl-CoA in a mixture of 100 mM Hepes, pH 7.4, 100 mM KCl, 10% (vol/vol) glycerol, 1 mM CoA, and 1 mM NAD at 27 °C for 20 min. It should be noted that any primary amine containing buffers (such as Tris buffer) will interfere with the chemical succinylation process. Because succinyl-CoA will also react with these amines they affect the succinylation efficiency as well as reproducibility.

Activity Assay of Citrate Synthase

Citrate synthase activity was measured as described previously⁴⁴. The reaction mixture contained 100 mM Tris·HCl (pH 8.0), 0.17 mM oxaloacetate, and 0.2 mM acetyl-CoA. The reaction was initiated by the addition of 4 μ g of total lysate from heart to the reaction mixture. The decreasing absorbance at 232 nm due to the cleavage of the thioesters bond was monitored for 5 min using a UV-visible spectrophotometer (Cary 50 UV-visible spectrophotometer; Varian).

Activity Assay of ATP Synthase (Complex V)

ATP synthase (complex V) activity was measured by linking the ATPase activity to NADH oxidation via the conversion of phosphoenolpyruvate to pyruvate by pyruvate kinase followed by pyruvate to lactate by lactate dehydrogenase. The assay was performed using a commercial kit from Cayman (MitoCheck Complex V Activity Assay Kit, 701000) according to the manufacturer's instructions. The reaction buffer was supplemented with 5 mM KCN. The reaction was started by adding 1 μ g mitochondrial suspension isolated from WT and *Sirt5* KO mouse heart. Oligomycin-sensitive activity was determined with 10 μ g/mL oligomycin. Complex V activity was calculated by using the extinction coefficient $6.22 \text{ mM}^{-1} \cdot \text{cm}^{-1}$.

Western Blot Analysis

Tissues were lysed in lysis buffer (50 mM Tris·HCl, pH 8.0, 150 mM NaCl, 1 mM EDTA, 1% Nonidet P-40, 5 mM nicotinamide, and protease inhibitor mixture). Protein extracts were separated by 12% SDS/PAGE and transferred onto PVDF membranes. The membrane was blocked using 5% BSA or milk in TBST (25 mM Tris·HCl, pH 7.4, 150 mM NaCl, and 0.1% Tween-20), incubated with antibodies in 5% BSA or milk in TBST, and developed in ECL Plus Western blotting detection reagents (GE Healthcare). The chemiluminescence was recorded by a Storm 860 Imager (Amersham Biosciences) and analyzed with ImageQuant TL v2005.

Echocardiography Analysis

Echocardiography was performed with a Vevo 2100 system (Visualsonics) using male mice as described⁴⁵. Briefly, mice that were fasted overnight were anesthetized with isoflurane (4–5% for induction and 1.5–2.5% for maintenance) and

their chest hair was removed with depilatory cream. The mice were then placed in a supine position on the Vevo mouse platform, where the paws were taped to ECG electrodes. Respiration rate, heart rate, and body temperature were continuously monitored. Warmed echo gel was gently applied on the hairless chest and the mouse hearts were imaged with a 40-MHz Echo probe. After echography, the residual gel was removed and Bepanthene cream was applied to the nude skin to prevent skin irritation. After the procedure mice were returned to their home cage.

Cardiac Output Measurement

Although cardiac output is the sum of aortic and coronary flow, aortic flow determines the majority of cardiac output, and hence we calculated cardiac output by extrapolating the aortic flow from the analysis of the left ventricle (LV) trace⁴⁶⁻⁴⁸. First, the LV trace analysis confirmed the reduced shortening fraction (calculated with **Eq. S1**) that we measured during echocardiography. Therefore, we extrapolated cardiac output (aortic flow) through LV trace analysis (**Eq. S2, S3 and S4**).

Here are the **equations**:

$$\text{Shortening fraction(LV trace, \%)} = [(\text{LVIDd} - \text{LVIDs})/\text{LVIDd}] \times 100\% \quad \text{[S1]}$$

$$\text{Diastolic volume(Vd)} = [7.0/(2.4 + \text{LVIDd})] \times \text{LVIDd}^3 \quad \text{[S2]}$$

$$\text{Systolic volume(Vs)} = [7.0/(2.4 + \text{LVIDd})] \times \text{LVIDd}^3 \quad \text{[S3]}$$

$$\text{Cardiac output(LV trace, mL/min)} = (\text{Vd} - \text{Vs}) \times \text{heart rate}/1,000 \quad \text{[S4]}$$

LV trace analysis using these formulas revealed a reduced cardiac output of *Sirt5* KO mice compared with the WT ($P = 0.544$, **Fig. B12H**).

Immunohistochemistry

H&E, Masson's trichrome, and F4/80 staining was performed as described previously^{45,49,50}. Briefly, tissue sections were obtained from Formalin-fixed heart slices. H&E, Masson's trichrome, and F4/80 stains were done using 8- μ m tissue slices. Fibrosis (accumulation of collagen) in heart was assessed by the blue color on Masson's trichrome staining. Antibodies against F4/80 (Abcam) were applied for immunohistochemistry to detect macrophages. F4/80 staining was visualized with HRP-conjugated goat anti-rat antibodies (Jackson ImmunoResearch) and DAB substrate (Sigma-Aldrich). Images were obtained using a slide scanner (VS120-L100; Olympus Life Sciences) and analyzed with ImageJ (imagej.nih.gov/ij/).

Fatty Acid Oxidation Measurements

Fatty acid oxidation in permeabilized heart tissues (39-week-old male WT and *Sirt5* KO mice) was monitored as described in previous reports^{51,52}. Briefly, mitochondrial respiration in response to palmitoyl-L-carnitine (50 μ M) was measured with an Oxygraph-2k instruments (Oroboros Instruments). Malate (2 mM) and ADP (2.5 mM) were used as a pretreatment. Substrate concentrations were chosen through preliminary experiments.

REFERENCES

1. Du J, et al. Sirt5 is a NAD-dependent protein lysine demalonylase and desuccinylase. *Science*. 2011;334(6057):806–809.
2. Lin H, Su X, He B. Protein lysine acylation and cysteine succination by intermediates of energy metabolism. *ACS Chem Biol*. 2012;7(6):947–960.
3. Tan M, et al. Identification of 67 histone marks and histone lysine crotonylation as a new type of histone modification. *Cell*. 2011;146(6):1016–1028.
4. Zhang Z, et al. Identification of lysine succinylation as a new post-translational modification. *Nat Chem Biol*. 2011;7(1):58–63.
5. Chen Y, et al. Lysine propionylation and butyrylation are novel post-translational modifications in histones. *Mol Cell Proteomics*. 2007;6(5):812–819.
6. Dai L, et al. Lysine 2-hydroxyisobutyrylation is a widely distributed active histone mark. *Nat Chem Biol*. 2014;10(5):365–370.
7. Jiang H, et al. SIRT6 regulates TNF- α secretion through hydrolysis of long-chain fatty acyl lysine. *Nature*. 2013;496(7443):110–113.
8. Tan M, et al. Lysine glutarylation is a protein posttranslational modification regulated by SIRT5. *Cell Metab*. 2014;19(4):605–617.
9. Zhu AY, et al. Plasmodium falciparum Sir2A preferentially hydrolyzes medium and long chain fatty acyl lysine. *ACS Chem Biol*. 2012;7(1):155–159.
10. Yang X-J, Seto E. Lysine acetylation: Codified crosstalk with other posttranslational modifications. *Mol Cell*. 2008;31(4):449–461.
11. Zhao S, et al. Regulation of cellular metabolism by protein lysine acetylation. *Science*. 2010;327(5968):1000–1004.
12. Pirinen E, Lo Sasso G, Auwerx J. Mitochondrial sirtuins and metabolic homeostasis. *Best Pract Res Clin Endocrinol Metab*. 2012;26(6):759–770.
13. Zhong L, Mostoslavsky R. Fine tuning our cellular factories: Sirtuins in mitochondrial biology. *Cell Metab*. 2011;13(6):621–626.
14. Rauh D, et al. An acetylome peptide microarray reveals specificities and deacetylation substrates for all human sirtuin isoforms. *Nat Commun*. 2013;4:2327.
15. Lin Z-F, et al. SIRT5 desuccinylates and activates SOD1 to eliminate ROS. *Biochem Biophys Res Commun*. 2013;441(1):191–195.
16. Park J, et al. SIRT5-mediated lysine desuccinylation impacts diverse metabolic pathways. *Mol Cell*. 2013;50(6):919–930.
17. Peng C, et al. The first identification of lysine malonylation substrates and its regulatory enzyme. *Mol Cell Proteomics*. 2011;10(12):012658.
18. Rardin MJ, et al. SIRT5 regulates the mitochondrial lysine succinylome and metabolic networks. *Cell Metab*. 2013;18(6):920–933.
19. Weinert BT, et al. Lysine succinylation is a frequently occurring modification in prokaryotes and eukaryotes and extensively overlaps with acetylation. *Cell Reports*. 2013;4(4):842–851.
20. Lombard DB, et al. Mammalian Sir2 homolog SIRT3 regulates global mitochondrial lysine acetylation. *Mol Cell Biol*. 2007;27(24):8807–8814.
21. Yu J, et al. Metabolic characterization of a Sirt5 deficient mouse model. *Sci Rep*. 2013;3:2806.
22. Nakagawa T, Lomb DJ, Haigis MC, Guarente L. SIRT5 Deacetylates carbamoyl phosphate synthetase 1 and regulates the urea cycle. *Cell*. 2009;137(3):560–570.

23. Boersema PJ, Raijmakers R, Lemeer S, Mohammed S, Heck AJR. Multiplex peptide stable isotope dimethyl labeling for quantitative proteomics. *Nat Protoc.* 2009;4(4):484–494.
24. Huang W, Sherman BT, Lempicki RA. Systematic and integrative analysis of large gene lists using DAVID bioinformatics resources. *Nat Protoc.* 2009;4(1):44–57.
25. Huang W, Sherman BT, Lempicki RA. Bioinformatics enrichment tools: Paths toward the comprehensive functional analysis of large gene lists. *Nucleic Acids Res.* 2009;37(1):1–13.
26. Uchida Y, Izai K, Orii T, Hashimoto T. Novel fatty acid beta-oxidation enzymes in rat liver mitochondria. II. Purification and properties of enoyl-coenzyme A (CoA) hydratase/3-hydroxyacyl-CoA dehydrogenase/3-ketoacyl-CoA thiolase trifunctional protein. *J Biol Chem.* 1992;267(2):1034–1041.
27. Fong JC, Schulz H. Short-chain and long-chain enoyl-CoA hydratases from pig heart muscle. *Methods Enzymol.* 1981;71(Pt C):390–398.
28. Venkatesan R, Wierenga RK. Structure of mycobacterial β -oxidation trifunctional enzyme reveals its altered assembly and putative substrate channeling pathway. *ACS Chem Biol.* 2013;8(5):1063–1073.
29. Ingwall JS. *ATP and the Heart.* Kluwer; Boston: 2001.
30. Katz AM. Metabolism of the failing heart. *Cardioscience.* 1993;4(4):199–203.
31. Imai S, Armstrong CM, Kaeberlein M, Guarente L. Transcriptional silencing and longevity protein Sir2 is an NAD-dependent histone deacetylase. *Nature.* 2000;403(6771):795–800.
32. Nishida Y, et al. SIRT5 regulates both cytosolic and mitochondrial protein malonylation with glycolysis as a major target. *Mol Cell.* 2015;59(2):321–332.
33. Herrmann G, Decherd JGM. The chemical nature of heart failure. *Ann Intern Med.* 1939;12(8):1233–1244.
34. Antozzi C, Zeviani M. Cardiomyopathies in disorders of oxidative metabolism. *Cardiovasc Res.* 1997;35(2):184–199.
35. Guertl B, Noehammer C, Hoefler G. Metabolic cardiomyopathies. *Int J Exp Pathol.* 2000;81(6):349–372.
36. Neubauer S. The failing heart--an engine out of fuel. *N Engl J Med.* 2007;356(11):1140–1151.
37. den Boer MEJ, et al. Mitochondrial trifunctional protein deficiency: A severe fatty acid oxidation disorder with cardiac and neurologic involvement. *J Pediatr.* 2003;142(6):684–689.
38. Brackett JC, et al. Two alpha subunit donor splice site mutations cause human trifunctional protein deficiency. *J Clin Invest.* 1995;95(5):2076–2082.
39. Boylston JA, et al. Characterization of the cardiac succinylome and its role in ischemia-reperfusion injury. *J Mol Cell Cardiol.* 2015;88:73–81.
40. Gibson GE, et al. Alpha-ketoglutarate dehydrogenase complex-dependent succinylation of proteins in neurons and neuronal cell lines. *J Neurochem.* 2015;134(1):86–96.
41. Wagner GR, Payne RM. Widespread and enzyme-independent N ϵ -acetylation and N ϵ -succinylation of proteins in the chemical conditions of the mitochondrial matrix. *J Biol Chem.* 2013;288(40):29036–29045.
42. Dils R, Carey EM. Fatty acid synthase from rabbit mammary gland. *Methods Enzymol.* 1975;35:74–83.
43. Yang Y, et al. Evaluation of different multidimensional LC-MS/MS pipelines for isobaric tags for relative and absolute quantitation (iTRAQ)-based proteomic analysis of potato tubers in response to cold storage. *J Proteome Res.* 2011;10(10):4647–4660.

44. Srere PA, Kosicki GW. The purification of citrate-condensing enzyme. *J Biol Chem.* 1961;236(10):2557–2559.
45. Ryu D, et al. A SIRT7-dependent acetylation switch of GABP β 1 controls mitochondrial function. *Cell Metab.* 2014;20(5):856–869.
46. Madonna R, Wu H, Shelat H, Geng YJ. CD1d-associated expression of NF- κ B and cardiac dysfunction in diabetic and obese mice. *Int J Immunopathol Pharmacol.* 2013;26(1):59–73.
47. Longhurst JC, Kelly AR, Gonyea WJ, Mitchell JH. Cardiovascular responses to static exercise in distance runners and weight lifters. *J Appl Physiol.* 1980;49(4):676–683.
48. Kessler KM. Ejection fraction derived by M-mode echocardiography: A table and comments. *Cathet Cardiovasc Diagn.* 1979;5(3):295–299.
49. Gariani K, et al. Eliciting the mitochondrial unfolded protein response via NAD repletion reverses fatty liver disease. *Hepatology.* 2015 doi: 10.1002/hep.28245.
50. Perino A, et al. TGR5 reduces macrophage migration through mTOR-induced C/EBP β differential translation. *J Clin Invest.* 2014;124(12):5424–5436.
51. Boyle KE, Zheng D, Anderson EJ, Neuffer PD, Houmard JA. Mitochondrial lipid oxidation is impaired in cultured myotubes from obese humans. *Int J Obes.* 2012;36(8):1025–1031.
52. Lemieux H, Semsroth S, Antretter H, Höfer D, Gnaiger E. Mitochondrial respiratory control and early defects of oxidative phosphorylation in the failing human heart. *Int J Biochem Cell Biol.* 2011;43(12):1729–173

APPENDIX C

IDENTIFICATION OF PROTEINS CAPABLE OF METAL REDUCTION FROM THE PROTEOME OF THE GRAM-POSITIVE BACTERIUM *Desulfotomaculum reducens* MI-1 USING AN NADH-BASED ACTIVITY ASSAY²

Abstract

Understanding of microbial metal reduction is based almost solely on studies of Gram-negative organisms. In this study, we focus on *Desulfotomaculum reducens* MI-1, a Gram-positive metal reducer whose genome lacks genes with similarity to any characterized metal reductase. Using non-denaturing separations and mass spectrometry identification, in combination with a colorimetric screen for chelated Fe(III)-NTA reduction with NADH as electron donor, we have identified proteins from the *D. reducens* proteome not previously characterized as iron reductases. Their function was confirmed by heterologous expression in *E. coli*. Furthermore, we show that these proteins have the capability to reduce soluble Cr(VI) and U(VI) with NADH as electron donor. The proteins identified are NADH:flavin oxidoreductase (Dred_2421) and a protein complex composed of oxidoreductase FAD/NAD(P)-binding subunit (Dred_1685) and dihydroorotate dehydrogenase 1B (Dred_1686). Dred_2421 was identified in the soluble proteome and is predicted to be a cytoplasmic protein. Dred_1685 and Dred_1686 were identified in both the soluble as well as the insoluble protein fraction, suggesting a type of membrane-association, although PSORTb predicts both proteins are cytoplasmic. This study is the first functional proteomic analysis of *D. reducens* and one of the first analyses of metal and radionuclide reduction in an environmentally relevant Gram-positive bacterium.

^{2a} This appendix is modified from published work: Otwell, A. E., Sherwood, R. W., Zhang, S., Nelson, O. D., Li, Z., Lin, H., Callister, S. J., and Richardson, R. E. (2015), "Identification of proteins capable of metal reduction from the proteome of the Gram-positive bacterium *Desulfotomaculum reducens* MI-1 using an NADH-based activity assay", *Environ. Microbiol.* 17, 1977-1990.

^{2b} I constructed all plasmids for overexpression and purification in *E. coli* and performed activity assays for Dred_2421 and the Dred_1685-1686 complex.

Introduction

Microorganisms capable of dissimilatory iron reduction are of interest due to their integral ecological roles and applications for heavy metal and radionuclide bioremediation¹⁻³. Over two decades of research in model Gram-negative bacteria (i.e. species of *Geobacter* and *Shewanella*) focusing on electron transfer to Fe(III) and U(VI) has shaped understanding of microbial metal reduction. Common to model Gram-negative metal respirers is the abundance of annotated multiheme c-type cytochromes (MHCs), many of which are membrane-bound and predicted to be involved in iron and/or uranium reduction⁴⁻⁶.

Becoming increasingly apparent, however, is the diversity and environmental prevalence of Gram-positive organisms capable of dissimilatory metal reduction. Specifically, numerous Clostridia species have been detected commonly in subsurface environments with heavy metal contamination, and several of these species have been demonstrated to use various metals (including Fe(III) and U(VI)) as electron acceptors⁷⁻¹¹. Mechanisms of electron transfer to metals in these phylogenetically distinct organisms are far less elucidated. Recent studies in two thermophilic Firmicutes, *Carboxydotherrmus ferrireducens* and *Thermincola potens*, support the involvement of MHCs localized on the cell surface^{12,13}. These MHC-rich thermophiles may be exceptions, however, as MHCs are scarce across the genomes of sequenced mesophilic Firmicutes⁶.

The sulfate reducing bacterium (SRB) *Desulfotomaculum reducens* MI-1, isolated from heavy-metal contaminated sediment, serves as a useful and novel system for the study of Gram-positive dissimilatory metal reduction. *D. reducens* has been

shown to use a variety of metals including U(VI), Fe(III), Cr(VI), Mn(IV) as electron acceptors while oxidizing lactate or butyrate¹⁴. *D. reducens* also reduces metals when grown fermentatively with pyruvate, and some studies have focused on metal reduction during this growth condition^{15,16}. A recent study concluded that although *D. reducens* does not appear to gain energy directly from the reduction of Fe(III) during fermentative growth on pyruvate, the Fe(III) serves as an electron sink, relieving thermodynamic limitations of fermentation resulting from H₂-buildup. Furthermore, the study suggested that direct contact was not required for the reduction of insoluble Fe(III), and riboflavin and small amounts of FMN (flavin mononucleotide) in spent media were identified as potential electron shuttles¹⁶. However, no insights regarding enzymes involved in Fe(III) reduction were provided in that study. Another unique capability of *D. reducens* following growth with pyruvate is U(VI) and Fe(III)-citrate reduction in the sporulated state, relevant to particular environments where conditions may vary dramatically over time¹⁵.

The genome of *D. reducens* has been sequenced and contains only one operon annotated as a c-type cytochrome, encoded by the two genes Dred_0700 and Dred_0701¹⁷. However, all evidence to date suggests that this cytochrome is not involved in metal reduction. A transcriptomic study comparing gene expression in *D. reducens* when grown fermentatively with pyruvate versus pyruvate and U(VI) did not find differential expression of this c-type cytochrome¹⁸. Furthermore, qRT-PCR analysis targeting Dred_0700 and Dred_0701 found expression levels to be around two orders of magnitude lower during Fe(III) reduction as compared with pyruvate fermentation. This study also failed to detect any peptides corresponding to the c-type

cytochrome under Fe(III) reduction or fermentative conditions¹⁶. Studies in our lab support these findings. Isobaric tag for relative and absolute quantitation (iTRAQ) based proteomic analysis of duplicate cultures of *D. reducens* grown with Fe(III)-citrate, pyruvate, and sulfate identified over 22,000 unique peptides. None of the detected peptides correspond to either gene encoding the c-type cytochrome (unpublished data). A member of the Peptococcaceae family, *D. reducens* is a close relative of other environmentally relevant metal and radionuclide reducing Firmicutes, namely *Desulfosporosinus* and *Desulfitobacterium* species^{19,20}. No metal-reducing proteins have yet been described in any of these three genera. Our major objective of this study was to identify proteins capable of iron reduction from the proteome of *D. reducens*. Not only were iron reductases identified and confirmed through heterologous expression, but these reductases were also shown to reduce soluble Cr(VI) (in the form of sodium dichromate) and U(VI) (in the form of uranyl acetate). To the best of our knowledge, this is the first report identifying and validating metal reductases from a Gram-positive organism through heterologous expression.

Results

To accomplish our objective, we optimized and applied an efficient and high-resolution, non-denaturing protein separation workflow that allows for the purification of functional proteins and protein complexes. Resulting protein fractions were screened for iron reduction activity using a colorimetric assay for Fe(II), based on the reagent ferrozine, where the reduction of Fe(III)-NTA with NADH as electron donor was monitored. Subsequent LC-MS/MS analysis was performed, leading to the

identification of proteins/protein complexes capable of iron reduction from the proteome of *D. reducens*. An overview of our implemented workflow is summarized in **Fig. C.1**. Proteins/protein complexes identified by this technique were then selected for functional validation by heterologous expression and biochemical characterization.

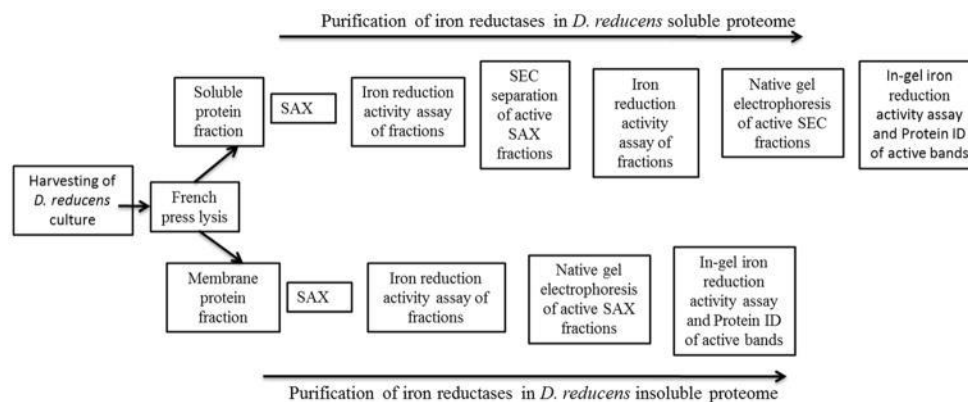


Figure C.1 Workflow implemented to identify iron reduction candidate proteins in *D. reducens*: A series of non-denaturing protein separation steps, with a screen for iron reduction activity following each step, was implemented in order to identify iron reductases from the proteome of *D. reducens*. SAX= strong anion exchange chromatography. SEC= size exclusion chromatography.

The *D. reducens* proteome under sulfate-reducing conditions confers an Fe(III) reducing phenotype

Initial proteomic separations were attempted with *D. reducens* cells grown with Fe(III)-citrate as electron acceptor and lactate as electron donor. However, attempts to extract active proteins from these cells were unsuccessful due to interference with Fe-precipitates. Therefore, cell culture conditions were modified to growth with sulfate as electron acceptor. Before protein separations were performed, cell suspension experiments were carried out to confirm Fe(III) reduction capability under these experimental culture conditions. Washed *D. reducens* cells grown with 28 mM sulfate

and 20 mM lactate were shown to reduce Fe(III)-NTA immediately (**Fig. C.2**), suggesting that the sulfate-grown *D. reducens* proteome is capable of Fe(III) reduction. Reduction was dependent on lactate, although controls without lactate displayed a small amount of reduction. A likely explanation for Fe(III)-NTA reduction by live *D. reducens* cells lacking added electron donor is utilization of stored electrons. *D. reducens* was recently predicted to contain a type of capacitor that stores reducing equivalents for later reduction of Fe(III)¹⁶.

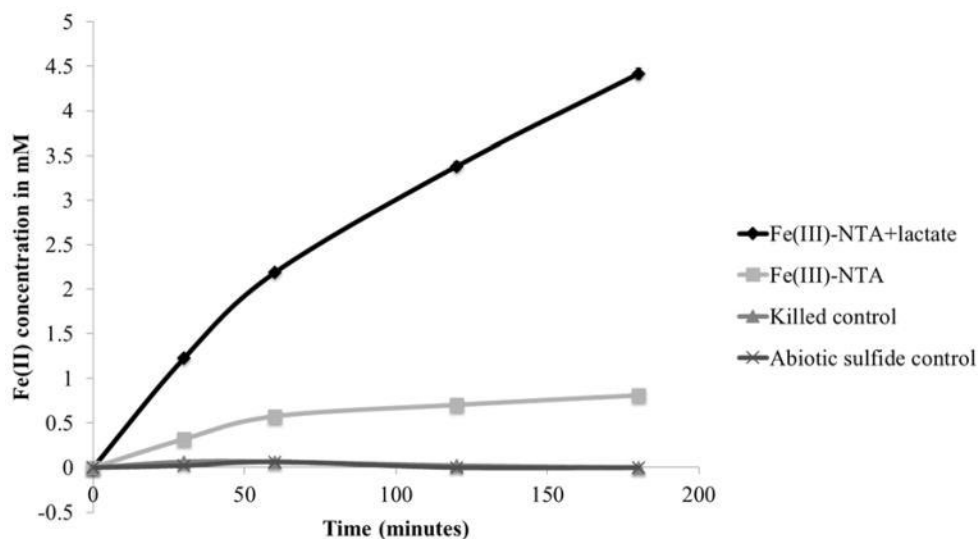


Figure C.2 Fe(III) reduction by *D. reducens* cell suspensions grown on sulfate reduction. Washed cell suspensions of *D. reducens* grown with 28 mM sulfate and 20 mM lactate were tested for iron reduction capability and shown to express the proteome necessary for immediate dissimilatory reduction of Fe(III)-NTA. Cells killed by boiling and an abiotic sulfide control determined by the concentration of sulfide measured following cell washing (0.25 mM) demonstrated lack of iron reduction capability. Cell concentration was 3×10^9 cells/mL, equal to a protein concentration of ~ 0.9 mg/mL of protein assuming 60% protein per cell dry mass. Error bars display standard error duplicate reactions.

Recovery of iron reduction activity in extracted proteins

Following protein extraction, the soluble and insoluble proteomes of *D. reducens* were analyzed through implementation of the workflow outlined in **Fig. C.1**. Iron reduction

activity obtained from the total soluble and insoluble fractions was quantified and is reported as nmol Fe(II) formed/min and specific activity (nmol Fe(II) formed/mg protein/min) (**Table C.1**). The specific activity in the insoluble fraction is nearly two times that of the soluble fraction (22.42 versus 12.64 nmol Fe(II) formed/mg protein/min).

Sample	Protein Concentration (mg/mL)	Iron Reduction Activity (nmol Fe(II) formed/min)	Specific Activity (nmol Fe(II) formed/mg protein/min)
Soluble (S) fraction	5.45	2.07	12.64
Insoluble (IS) fraction	1.21	0.81	22.42
S Peak 1: SAX 16'	<0.125	0.79	>210.82
S Peak 1: SAX 16' SEC 9.5'	<0.125	0.50	>132.14
S Peak 2: SAX 31–32'	<0.125	0.19	>50.09
S Peak 2: SAX 31–32' SEC 10.5'	<0.125	0.16	>43.94
IS Peak 1: SAX 31'	<0.125	0.08	>22.16

Table C.1. Recovery of iron reduction activity in protein fractions. Specific iron reduction activity is calculated for protein fractions using the iron reduction activity assay. Nearly twice the specific iron reduction activity was recovered in the total insoluble fraction versus the soluble fraction. Specific activities described as “>” values were limited in precision due to below detect protein concentrations as determined by Bradford assay. SAX= anion exchange chromatography. SEC= size exclusion chromatography.

Soluble protein fraction

The soluble proteome of *D. reducens* was separated using a series of three non-denaturing separation steps: strong anion exchange chromatography (SAX), size exclusion chromatography (SEC), and native gel electrophoresis. Iron reduction activity was screened for following each subsequent separation. Following SAX separation of the soluble protein fraction, peaks of iron reduction activity were recovered at 13', 16', 31–32', and 47–48', depicted by the gray line plotted in **Fig. C.3a**. These fractions were selected for high-resolution SEC separation, and iron reduction activity was retained following separation of both SAX 16' and 31–32' fractions, identified as Peak 1 and 2 respectively in **Fig. C.3a**, but not from the other fractions. The SEC-separated 16' SAX fraction produced a peak of iron reduction activity in the 9.5' SEC fraction, and the third dimension of separation (native gel electrophoresis followed by the in-gel activity assay) led to the identification of an iron reductase band (~280 kDa) visualized as a pink band due to the formation of the ferrozine-Fe(II) complex (**Fig. C.3b**). After analysis of in-gel digests of the active gel-band by LC-MS/MS and based on detection of at least two unique peptides, four proteins were identified including NADH:flavin oxidoreductase (Dred_2421), oligoendopeptidase F (Dred_2457), acetyl-CoA acetyltransferase (Dred_1784), and sulfate adenylyltransferase (Dred_0635) (**Table C.2a**).

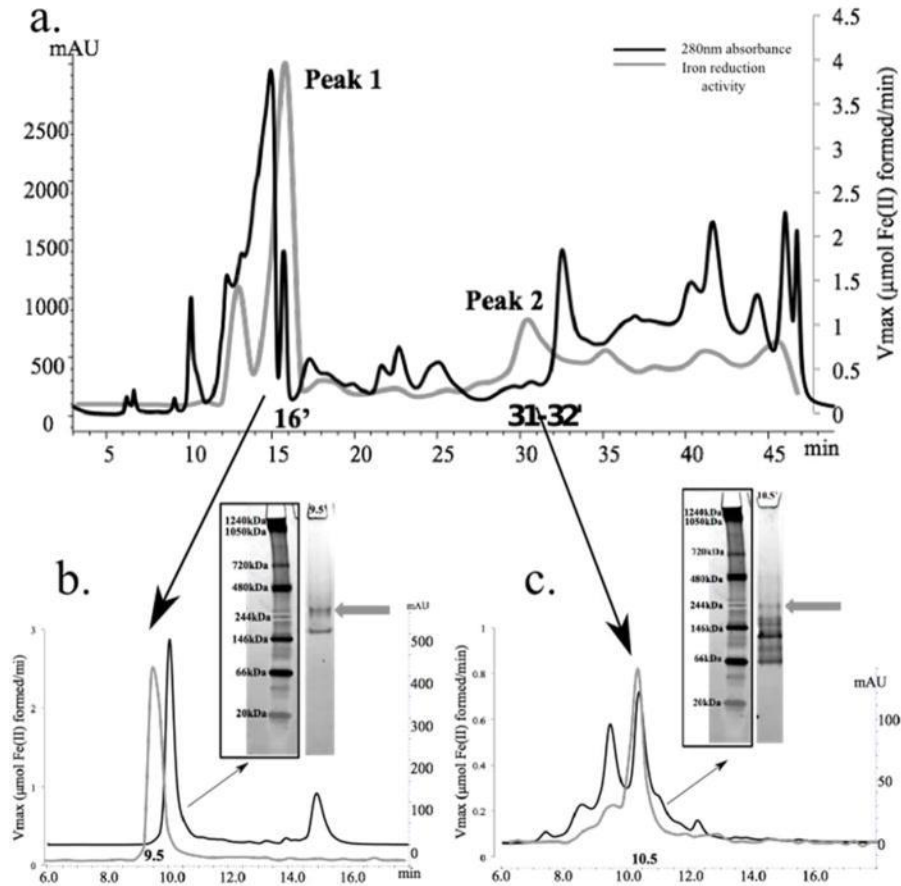


Figure C.3 Identification of iron reduction activity in the soluble proteome of *D. reducens*. Protein concentration (determined by absorbance at 280 nm and presented as mAU) is represented by the black chromatogram, while the gray line presents an overlay of iron reduction activity ($\mu\text{mol Fe(II) formed/min}$). **[a]** SAX separation of the soluble protein fraction led to the recovery of two dominant iron reduction peaks that are maintained through two subsequent dimensions of separation. **[b]** SEC separation of Peak 1 (SAX 16' fraction) led to the recovery of iron reduction activity in fraction 9.5'. Further separation with native gel electrophoresis recovered an active iron reductase band (visualized as a pink band at ~ 280 kDa, designated by gray arrow). **[c]** SEC separation of Peak 2 (SAX 31–32' fraction) led to the recovery of iron reduction activity in fraction 10.5'. Further separation with native gel electrophoresis recovered an active iron reductase band (visualized as a pink band at ~ 244 kDa, designated by gray arrow). SAX= strong anion exchange chromatography. SEC= size exclusion chromatography.

The SAX 31–32' fraction (Peak 2 in **Fig. C.3a**) was further separated with SEC and produced a peak of activity in the 10.5' SEC fraction. Native gel electrophoresis followed by the in-gel activity assay indicated an iron reductase band at ~244 kDa (**Fig. C.3c**), again visualized as a pink band. LC-MS/MS identified four proteins in the excised band by at least two unique peptides including oxidoreductase FAD/NAD(P)-binding subunit (Dred_1685), dihydroorotate dehydrogenase 1B (Dred_1686), 4Fe-4S ferredoxin (Dred_0137), and pyruvate flavodoxin/ferredoxin oxidoreductase domain-containing protein (Dred_0047) (**Table C.2b**). Specific iron reduction activity of active fractions identified following separation of the soluble proteome is reported in **Table C.1**. Due to protein concentrations below the detection limit of the Bradford assay, specific activities could only be approximated in separated fractions.

a.

Locus Tag	Annotation	Protein Score	Protein Mass	Unique peptides identified	emPAI	Expressed and purified?
Dred_2421	NADH:flavin oxidoreductase	1502	72319	35	3.72	Yes
Dred_2457	oligoendopeptidase F	478	69310	13	0.83	No
Dred_1784	acetyl-CoA acetyltransferase	412	41203	11	1.16	No
Dred_0635	sulfate adenylyltransferase	85	44129	4	0.33	No

b.

Locus Tag	Annotation	Protein Score	Protein Mass	Unique peptides identified	emPAI	Expressed and purified?
Dred_1685	oxidoreductase FAD/NAD(P)-binding subunit	431	28894	14	3.13	Yes
Dred_1686	dihydroorotate dehydrogenase 1B	259	32012	7	0.81	Yes
Dred_0137	4Fe-4S ferredoxin	150	111909	6	0.19	No *
Dred_0047	pyruvate flavodoxin/ferredoxin oxidoreductase domain-containing protein	78	40112	2	0.17	Yes

c.

Locus Tag	Name	Protein Score	Protein Mass	Unique peptides identified	emPAI	Expressed and purified?
Dred_3152	ATP synthase F1 subunit alpha	154	54403	5	0.34	No
Dred_1686	dihydroorotate dehydrogenase 1B	143	32012	3	0.35	Yes
Dred_0095	GntR family transcriptional regulator	141	25831	4	0.63	No
Dred_1685	oxidoreductase FAD/NAD(P)-binding subunit	130	28894	5	0.73	Yes
Dred_0637	adenylylsulfate reductase subunit alpha	66	69579	2	0.1	No

Table C.2: Proteins identified from excised iron-reduction active gel bands.

Following LC-MS/MS analysis, proteins identified by at least two unique peptides from excised iron-reduction active gel bands are reported. Potential iron reduction proteins, based on protein score and annotation, were heterologously expressed and purified in *E. coli* for further characterization. [a] is from separations involving *D. reducens* soluble fraction SAX Peak 1 (see Fig. 3b). [b] is from separations involving *D. reducens* soluble fraction SAX Peak 2 (see Fig C.3c). [c] is from separations involving *D. reducens* insoluble fraction (see Fig. C.4). Values in this table were derived from analysis with Mascot. Protein score is a relative number assigned to rank reported proteins within a single analysis, defined as the sum of the highest ions score for each distinct sequence. The Exponentially Modified Protein Abundance Index (emPAI) provides an approximate, label-free, relative quantitation of the proteins in the mixture based on protein coverage by the peptide matches in the database search result. The final column denotes whether the protein was heterologously expressed and purified in *E. coli*. *Dred_0137 was selected for expression, but mutations accumulated during the cloning process prevented creation of an expression vector.

Insoluble protein fraction

The insoluble proteome of *D. reducens*, which was extracted in the presence of the detergent n-Dodecyl β -D-maltoside (DDM), was separated using two non-denaturing separation steps, including SAX and native gel electrophoresis. Previous experiments with all three phases of separation led to a loss of Fe(III) reduction activity in the insoluble fraction, and for this reason the SEC step was excluded from this workflow. Following SAX, a dominant activity peak was recovered at 31' (**Fig. C.4**). Further separation of the 31' fraction with native gel electrophoresis led to the identification of an iron reductase band at ~244 kDa (**Fig. C.4**). The subsequent LC-MS/MS analysis of the gel band identified five proteins based on at least two unique peptides, including again the proteins Dred_1685 and Dred_1686. The other proteins identified were ATP synthase F1 subunit alpha (Dred_3152), GntR family transcriptional regulator (Dred_0095), and adenylylsulfate reductase subunit alpha (Dred_0637) (**Table C.2c**). Specific iron reduction activity of the active fraction identified following separation of the insoluble proteome is reported in **Table C.1**. Because protein concentration was below the detection limit of the Bradford assay, specific activity could only be approximated in this fraction.

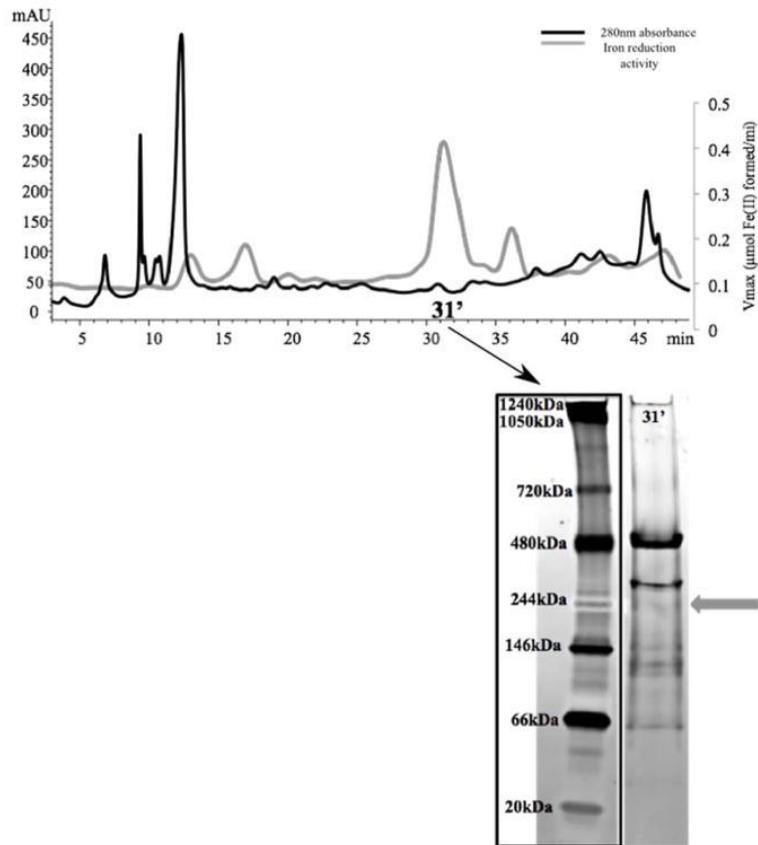


Figure C.4 Identification of iron reduction activity in the insoluble proteome of *D. reducens*. Protein concentration (determined by absorbance at 280 nm and presented as mAU), is represented by the black chromatogram, while the gray line presents an overlay of iron reduction activity ($\mu\text{mol Fe(II) formed/min}$). [a]. SAX separation of insoluble protein fraction led to the recovery of a dominant peak at 31'. Further separation with native gel electrophoresis recovered an active iron reductase band (visualized as a pink band at ~244 kDa, designated by gray arrow). SAX= strong anion exchange chromatography. SEC= size exclusion chromatography.

Heterologous expression and characterization of metal reductase capability

The workflow outlined in **Fig. C.1** led to short lists of potential iron reductases from the proteome of *D. reducens* (**Table C.2**). In order to confirm iron reductase activity, targets were selected for heterologous expression and affinity purification. Following tests for iron reduction activity, further characterization was performed.

Confirmation of iron reduction activity

From peak 1 of the soluble fraction, Dred_2421 (NADH: flavin oxidoreductase) was selected as the primary target for heterologous expression based on the highest protein score and its annotation as the sole oxidoreductase from the list (**Table C.2a**). An SDS gel of heterologously expressed and purified Dred_2421 confirmed its predicted molecular weight of ~72 kDa (**Fig. C.5a**). The purified protein was yellow in color due to bound flavin, and both FMN and FAD (flavin adenine dinucleotide) were detected with reversed-phase high performance liquid chromatography (**Fig. C.5b**). Tests for iron reduction activity were performed, and Dred_2421 was confirmed as an iron reductase (**Fig. C.6**). Activity was found to be NADH-dependent, as Dred_2421 does not use NADPH as an electron donor. The specific activity was calculated (based on the first 6 min of the iron reduction activity assay following Fe(III)-NTA injection) and is displayed in **Table C.3**. Based on recovery of the active band at ~280 kDa in the native gel (**Fig. C.3b**), we predict that Dred_2421 (~72 kDa) functions as a homotetramer.

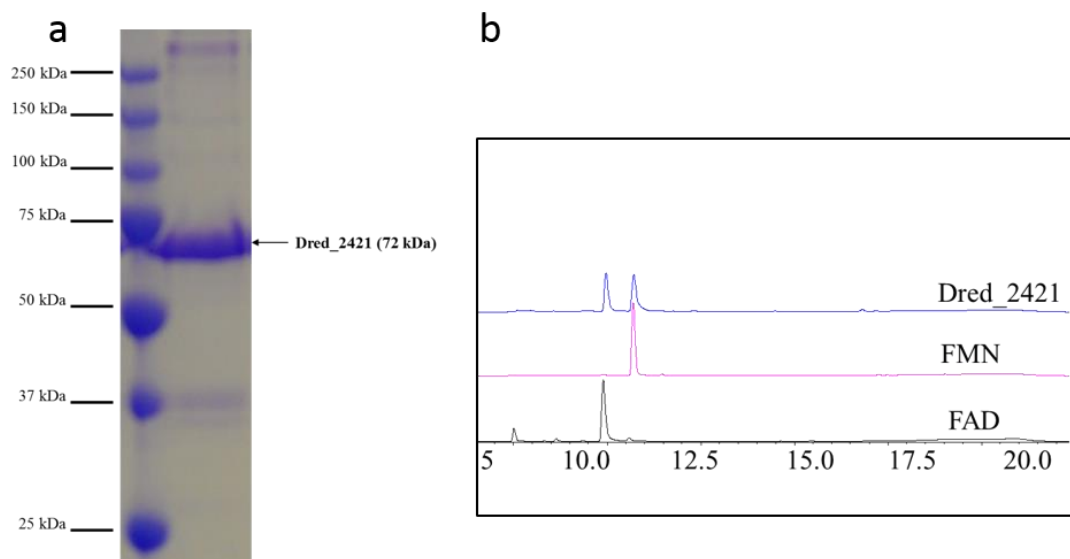


Figure C.5: Purification and Characterization of Dred_2421: [a] SDS-PAGE analysis of recombinant Dred_2421 following expression and affinity purification shows highly purified protein at expected size of 72 kDa. [b] Dred_2421 contains bound flavin in the form of FMN and FAD. To examine the cofactors bound to Dred_2421, the protein was boiled at 95°C for 5 min and then spun down to remove the precipitation. The supernatant was analyzed by reversed-phase HPLC at 260 nm and standards for FMN (flavin mononucleotide) and FAD (flavin adenine dinucleotide) were run. Elution time in minutes is displayed on the x-axis. Both flavins were identified in Dred_2421.

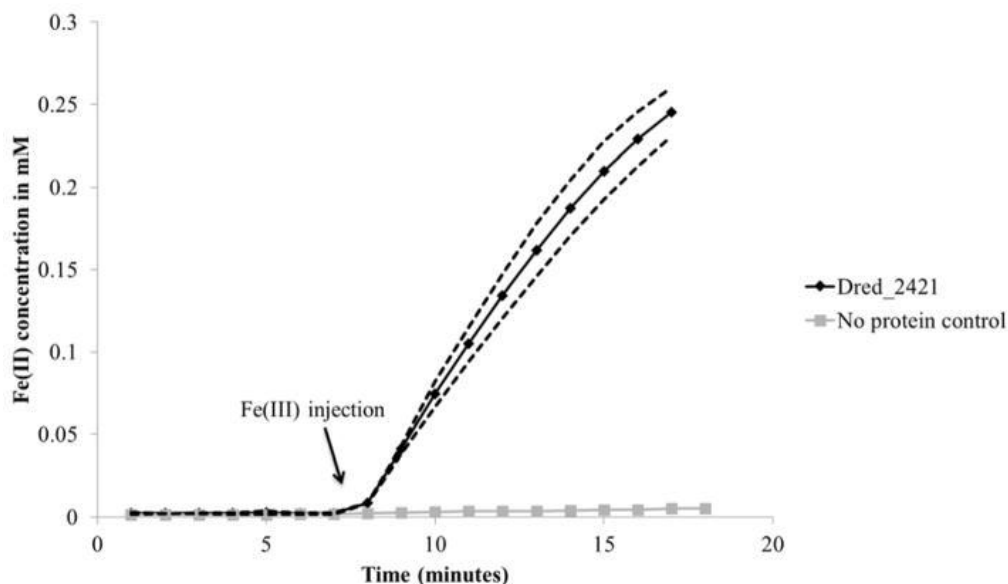


Figure C.6 Iron reduction by Dred_2421

Following heterologous expression and purification of Dred_2421, iron reduction capability was confirmed using the iron reduction activity assay. 0.5 mM Fe(III) was added at 7 min. The dotted lines display standard deviation across triplicate reactions. Reactions contained 1 μ M Dred_2421 and 0.2 mM NADH as electron donor.

Locus Tag	Peak identified from (corresponding to Table C.1)	Specific Activity (nmol Fe(II) formed/mg protein/min)
Dred_2421	S Peak 1	361.95
Dred_1685–1686	S Peak 2, IS Peak 1	627.68

Table C.3 Iron reduction activity in heterologously expressed proteins: Specific iron reduction activity is calculated for heterologously expressed and purified proteins identified in fractions described in **Table C.1**. Micromoles of Fe(II) formed per minute were calculated based on the first 6 min (following Fe(III) injection) of the reactions displayed in **Fig. C.6 and C.7**.

Dred_1685 and Dred_1686 were two other primary targets for heterologous expression based on their predicted annotations involving oxidoreductase activity as well as their identification in protein lists from Peak 2 of the soluble fraction as well as in the insoluble fraction peak (**Table C.2b-c**). Matching charge and size evidence leading to these protein lists (31–32' or 31' SAX fraction from the soluble and insoluble fractions respectively and ~244 kDa in both in-gel activity assays) supports that the same iron reductase was active in peak 2 of the soluble fraction and the insoluble fraction peak (**Fig. C.3 and C.5**). Both individual proteins were expressed successfully. Dred_1685 was brownish in color, consistent with its annotated 2 iron, 2 sulfur cluster binding activity (<https://img.jgi.doe.gov/>). Dred_1686 was yellow in color, suggesting the presence of bound flavin. The iron reduction activity assay was initially performed with purified Dred_1685 and Dred_1686 expressed separately, and no iron reduction activity for each individual protein was observed (**Fig. C.7**). However, upon mixing of the two purified proteins, iron reduction was observed, providing evidence that the two proteins form a complex. In order to confirm this prediction, Dred_1685 and Dred_1686 were co-expressed on a single plasmid with a His₆-tag only on Dred_1685. Nickel affinity column purification followed by SDS-PAGE electrophoresis resulted in the identification of two distinct protein bands of appropriate size (29 kDa for Dred_1685 and 32 kDa for Dred_1686), confirming the formation of a complex and suggesting a 1:1 stoichiometry (**Fig. C.8**). The iron reduction activity assay demonstrated iron reduction capability in this complex (**Fig. C.7**). The specific activity was calculated (based on the first 6 min of the iron reduction activity assay following Fe(III)-NTA injection) and is displayed in **Table C.3**. NADPH was also used as an electron donor

for Fe(III)-NTA reduction by the Dred_1685–1686 complex, but at a rate nearly 5 times slower over the first 6 min than that calculated with NADH as electron donor. Based on the predicted size of the active complex in native gels (~244 kDa), we predict the complex is a heterooctamer consisting of four molecules from each of the two proteins.

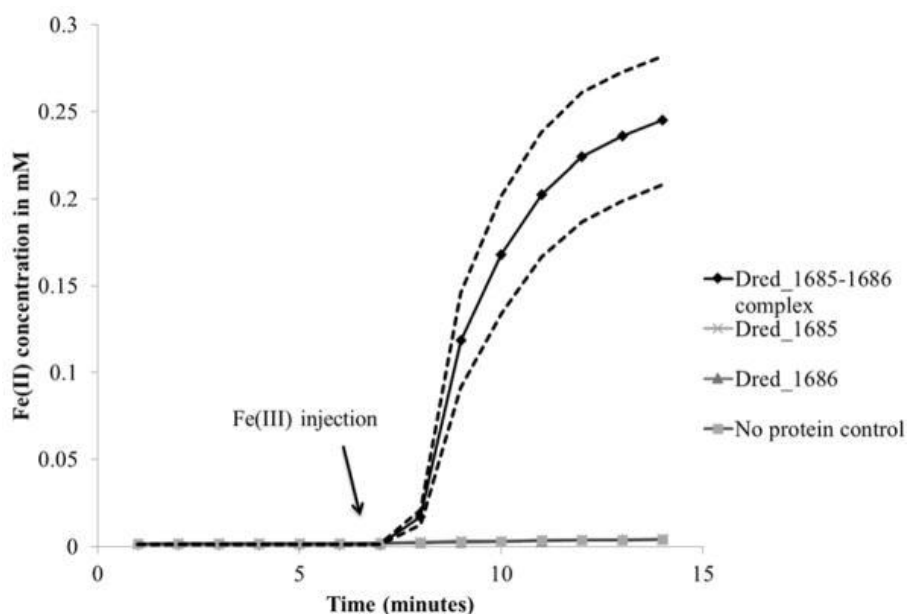


Figure C.7 Iron reduction by Dred_1685–1686 complex. Following heterologous expression and copurification of Dred_1685 and Dred_1686, iron reduction capability was confirmed using the iron reduction activity assay. 0.5mM Fe(III)-NTA was added at 7 min. The copurified complex is necessary for iron reduction, as Dred_1685 and Dred_1686 individually do not demonstrate iron reduction capability. The dotted black lines display the standard deviation across triplicate reactions. Reactions contained 1 μ M of purified proteins and 0.2 mM NADH as electron donor.

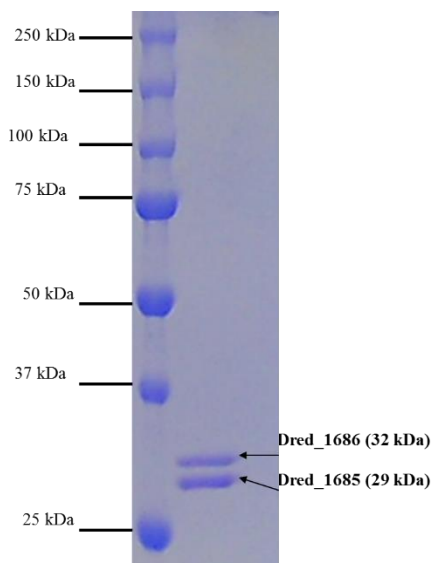


Figure C.8: Co-expression and purification of Dred_1685 and Dred_1686: SDS-PAGE analysis of recombinant Dred_1685-1686 complex following pETDuet co-expression, affinity purification, and size exclusion chromatography. The presence of two bands at predicted sizes for Dred_1685 and Dred_1686 provides evidence for the formation of the Dred_1685-1686 complex, as only Dred_1685 contained a His₆-tag

In order to thoroughly investigate proteins identified in the fractions with iron reduction activity, other proteins whose annotations suggested potential involvement were heterologously expressed. This included pyruvate flavodoxin/ferredoxin oxidoreductase domain-containing protein (Dred_0047), which was identified in peak 2 of the soluble fraction. Following heterologous expression and purification, Dred_0047 was found to not be able to reduce iron. Dred_0137, a 4Fe-4S ferredoxin, was also selected for heterologous expression, but multiple mutations throughout the cloning process have prevented expression, meaning Fe(III) reduction capability could not be tested. Although Dred_0637 was identified in the insoluble fraction peak and has an annotation as an oxidoreductase (adenylylsulfate reductase subunit alpha), it was not selected as it had a low protein score and its predicted involvement in the sulfate reduction pathway suggests that its presence in the active gel band was incidental.

Discovery of Cr(VI) and U(VI) reductase capability

As *D. reducens* is capable of reducing contaminant heavy metals and radionuclides, specifically Cr(VI) and U(VI), the discovered Fe(III) reductases were tested for soluble Cr(VI) (in the form of sodium dichromate) and U(VI) (in the form of uranyl acetate) reduction capability. For both metals, colorimetric assays were employed, and the disappearance of the +6-oxidation state was monitored. Both Dred_2421 and the Dred_1685–1686 complex were capable of Cr(VI) reduction with NADH as electron donor (**Fig. C.9**). As we found that NADH was capable of some abiotic Cr(VI) reduction, we added 1 mM NADH in two steps, first at time zero and then at 80 min, in order to best visualize enzymatic reduction. The individual proteins Dred_1685 and Dred_1686 resembled the no protein control, again providing evidence that Dred_1685 and Dred_1686 form a functional complex that is capable of metal reduction.

Discovered Fe(III) reductases were also tested for the capability to reduce U(VI) with NADH as electron donor. Both Dred_2421 and the Dred_1685–1686 complex displayed U(VI) reductase activity (**Fig. C.10**). As expected, the single proteins Dred_1685 and Dred_1686 were not capable of U(VI) reduction. As U(IV) can be oxidized back to U(VI) by oxygen, we exposed our reactions to air following the experiment. Re-oxidation of the reactions following U(VI) reduction provides further support that U(VI) was indeed being reduced, rather than simply disappearing from solution due to sorption (**Fig. C.11**).

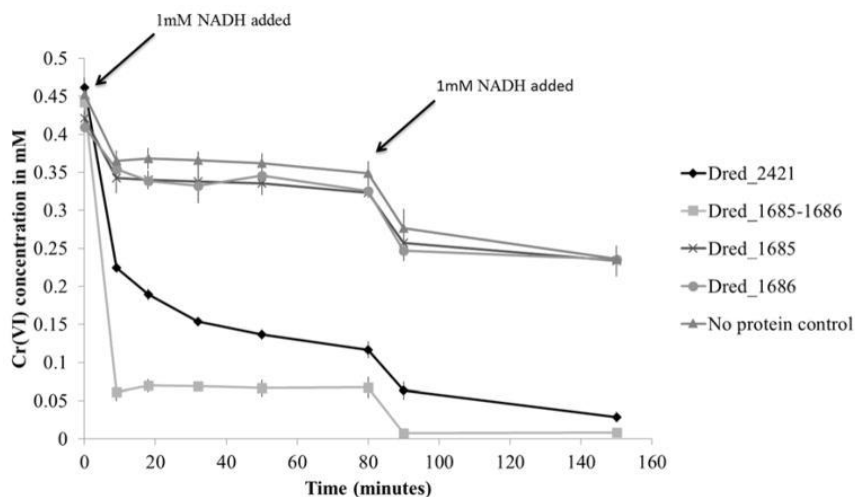


Figure C.9 Cr(VI) reduction by Dred_2421 and Dred_1685–1686 complex. The disappearance of Cr(VI) over time is monitored based on the diphenylcarbazide method. In order to reduce the effects of abiotic reduction by NADH, only 1mM NADH was added at time zero. After an additional 1mM NADH was added at 80 min, complete Cr(VI) reduction is observed for both Dred_2421 and the Dred_1685–1686 complex. Individual Dred_1685 and Dred_1686 proteins resembled the no protein control. Reactions contained 2 μ M purified proteins.

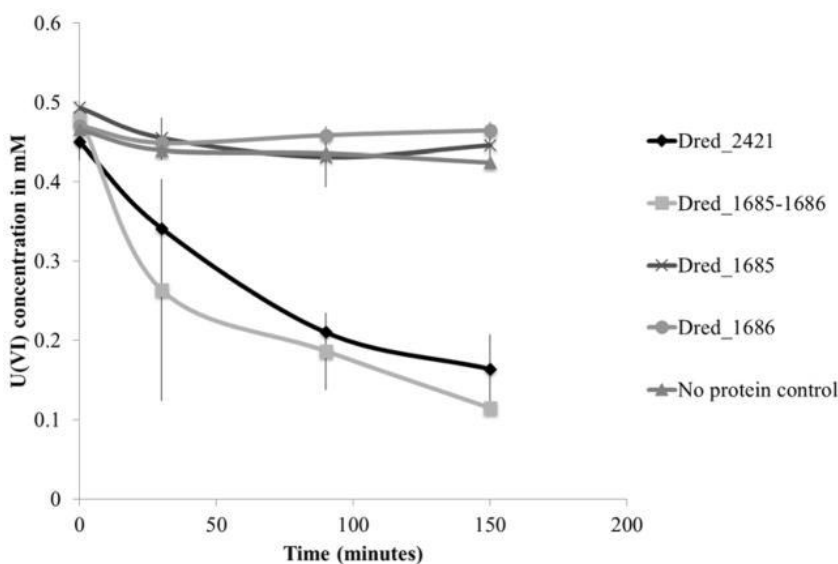


Figure C.10 U(VI) reduction by Dred_2421 and Dred_1685–1686 complex. The disappearance of U(VI) over time is monitored using a method dependent on the reagent Arsenazo-III. Individual Dred_1685 and Dred_1686 proteins resembled the no protein control. Reactions contained 10 μ M purified protein.

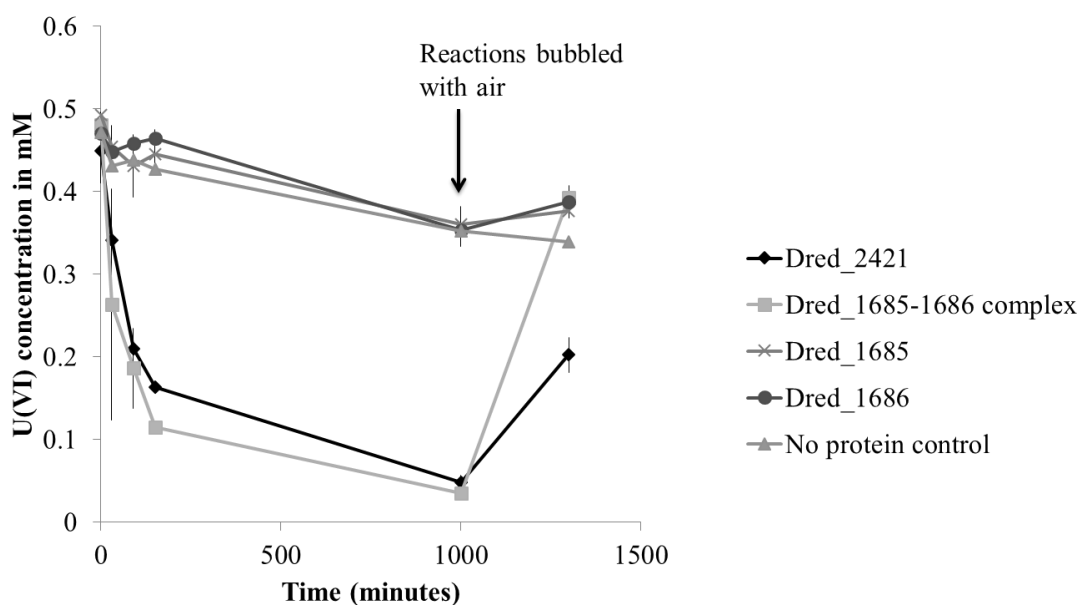


Figure C.11: Reoxidation of reduced U(VI) provides evidence for U(VI) reduction: Following reduction of U(VI) and anaerobic incubation overnight, reactions were bubbled with 150 mL ambient air and left in an aerobic environment for 5 hr. Subsequent measures of U(VI) show oxidation of the uranium back to U(VI) in the reactions containing discovered uranium reductases, Dred_2421 and Dred_1685-1686 complex. Individual Dred_1685 and Dred_1686 proteins resembled the no protein control.

Discussion

The field of microbial metal reduction is dominated by studies in Gram-negative bacteria whose genomes encode an abundance of multiheme c-type cytochromes. Our aim was to discover enzymes capable of iron reduction in *D. reducens*, an organism that encodes only a single c-type cytochrome in its genome and is phylogenetically distinct from the model metal reducers. This led to the identification of a protein and a protein complex that are not only capable of reducing Fe(III)-NTA but also Cr(VI) and U(VI) with NADH as electron donor. Proteomic studies combined with protein biochemistry, as seen here, are essential in order to validate existing genome annotations and/or

discover new functional annotations in uncharacterized organisms such as *D. reducens*, rather than relying on automated curation. Our separation methods were designed with the goal of maintaining the *D. reducens* proteome at a functional level. While it is possible that complexes or interacting complexes necessary for activity were broken up, the identification of two proteins that require the formation of a complex for iron reductase activity (Dred_1685 and Dred_1686) points towards the success of our methods. The non-denaturing separation workflow described allows rapid and high-resolution protein fractionation and can be employed for a diverse range of functional screens in a variety of organisms in the future.

Based on the lack of understanding of energy-producing processes in *D. reducens*, or the physiologically relevant electron donor for Fe(III) reduction, NADH was selected as an electron donor based on previous studies in model organisms^{21,22}. As such, the use of NADH as electron donor to screen for iron reduction activity leads to inherent selectivity towards NADH-dependent oxidoreductases, and thus it is uncertain whether the identified proteins have a physiologically relevant role in metal reduction. It is possible that these proteins are involved in the recently described thermodynamic relief mechanism when *D. reducens* is grown fermentatively with pyruvate, where Fe(III) reduction serves as an electron dump rather than an energy-deriving process¹⁶. It is unclear at this time whether this is also the case for Fe(III) reduction by *D. reducens* with lactate as electron donor, although the original isolation paper reports use of Fe(III) by *D. reducens* as a true electron acceptor under these conditions¹⁴. However, preliminary evidence suggests that *D. reducens* is not using its annotated Type 1 NADH dehydrogenase (Dred_2036–2046) in a classic respiration sense when grown on Fe(III)-

citrate and lactate. Under this growth condition, global proteomic analysis detected only one of the 11 subunits of the NADH dehydrogenase operon (unpublished data). Additional studies are required in order to elucidate catabolic processes in *D. reducens*, and genetic inactivation studies are necessary in order to provide a link between the proteins identified in this study and an *in vivo* role in metal reduction. However, without a genetic system currently available, our study serves as an initial functional survey of a poorly characterized proteome and has identified Fe(III)-NTA, Cr(VI), and U(VI) reductase activity in a protein and protein complex distinct from described metal reductases.

One of the proteins identified in this study, Dred_2421, is a soluble protein classified as an Old Yellow Enzyme (OYE). The first class of flavin-dependent enzymes identified, this group has been studied for many years, but physiological roles remain elusive²³. Previous reports have identified iron reduction capability in proteins annotated as flavin oxidoreductases, but these are described as assimilatory iron reductases and require the addition of exogenous flavin²⁴⁻²⁶. Dred_2421, however, contains tightly bound flavins (FMN and FAD, as shown in **Fig. C.5** and reduces Fe(III)-NTA without the addition of exogenous flavin. In fact, tests adding exogenous riboflavin did not increase rates of Fe(III)-NTA reduction by Dred_2421. Based on the annotation of Dred_2421 as an NADH:flavin oxidoreductase, as well as the predicted involvement of riboflavin and FMN in Fe(III) reduction in *D. reducens* when grown on pyruvate, Dred_2421 was tested for the ability to reduce riboflavin and FMN with NADH as electron donor¹⁶. Neither flavin was reduced by Dred_2421, further supporting the role of Dred_2421 as a metal reductase.

Dred_2421 is predicted to be in its own operon, and in fact on the genome falls in the middle of a region encoding genes predicted to be involved in flagella-related processes. This presumable genetic rearrangement is not conserved in any other sequenced *Desulfotomaculum* species (<https://img.jgi.doe.gov/>). Interestingly, the twelve proteins with highest sequence similarity to Dred_2421 (60–80% identity across 99% query coverage) are all from species of *Desulfosporosinus* and *Desulfitobacterium*, both genera of Gram-positive metal reducers (<http://blast.ncbi.nlm.nih.gov/>). No studies have investigated pathways of Fe(III) reduction in either of these two genera. Close relatives of *D. reducens*, we predict that similar metal reductase activity would be found in these *Desulfosporosinus* and *Desulfitobacterium* NADH:flavin oxidoreductases. *E. coli* species encode an orthologous protein to Dred_2421 (36% identity across 98% query coverage), and the crystal structure has been solved²⁷ (<http://blast.ncbi.nlm.nih.gov/>). This protein was heterologously expressed and purified by our group and found to lack Fe(III)-NTA reduction with both NADH and NADPH as electron donor (unpublished data). This finding supports the possibility that Dred_2421 has a specifically evolved physiological role as a metal reductase. Furthermore, a published transcriptomic study, with microarray data deposited at NCBI's Gene Expression Omnibus, compares conditions of *D. reducens* grown with pyruvate versus pyruvate and U(VI)¹⁸. Dred_2421 is increased in expression on U(VI) conditions by ~1.3 times during both mid and late exponential phase (<http://www.ncbi.nlm.nih.gov/geo/>).

Our studies also identified a complex capable of Fe(III), Cr(VI), and U(VI)

reduction, composed of Dred_1685 and Dred_1686. This complex was recovered from both the soluble as well as the insoluble (presumably membrane) protein fraction. These genes are predicted to be involved in the fourth step of pyrimidine biosynthesis, oxidizing dihydroorotate to orotate with NAD, and are in a predicted operon composed of Dred_1685–1689. This operon is conserved across five sequenced species of *Desulfotomaculum*. One of these is the only other known Fe(III) reducing species in the genus, *Desulfotomaculum hydrothermale*, while tests of Fe(III) reduction aren't reported in the literature for the other four species. This operon includes a lipoprotein signal peptidase, which is predicted to be localized to the cytoplasmic membrane according to PSORTb²⁸. This peptidase is missing in other sequenced *Desulfotomaculum* species including *Desulfotomaculum acetoxidans*, a species tested and unable to reduce Fe(III) based on a 1993 paper and confirmed in studies in our lab²⁹.

Other studies have found dihydroorotate dehydrogenase 1B (the annotation for Dred_1686) and homologs of Dred_1685 (annotations vary) to form a complex that is required for functionality. For instance, in the Gram-positive bacterial model for these proteins (*Lactococcus lactis*), a homolog of Dred_1686 (51% identity across 95% query coverage) and a homolog of Dred_1685 (34% identity across 93% query coverage) form a complex that is required for a functional enzyme (<http://blast.ncbi.nlm.nih.gov/>). However, in *L. lactis* this complex is predicted to be a heterotetramer, while our findings support the formation of a heterooctamer based on the molecular weight of the active complex in native gels³⁰. Furthermore, dihydroorotate dehydrogenase 1B in Gram-positive organisms like *L. lactis* and *D. reducens* are grouped into Type 1

dihydroorotate dehydrogenases, which are predicted to be localized to the cytosol. Type 2 dihydroorotate dehydrogenases, on the other hand, are associated with the inner membrane³¹. We recovered Dred_1685 and Dred_1686 in both the soluble and insoluble fractions. The insoluble protein fraction was thoroughly washed following separation from the soluble fraction, demonstrated by the lack of carryover of the most active soluble peak following SAX separation (peak 1 in **Fig. C.3a**) into the insoluble fraction. Therefore, we believe the localization of Dred_1685 and Dred_1686 to both the soluble and insoluble fraction is a true result and supports the claim that this complex is in some way associated with the membrane, in contrast to other Type 1 dihydroorotate dehydrogenases.

As with Dred_2421, the Dred_1685–1686 complex was found to not have riboflavin or FMN reduction capability with NADH as electron donor, nor was Fe(III)-NTA reduction enhanced with addition of exogenous riboflavin. A small increase was seen in the expression of Dred_1685 and Dred_1686 on pyruvate versus pyruvate and U(VI), based on the available transcriptomic data (<http://www.ncbi.nlm.nih.gov/geo/>). Furthermore, the Dred_1685–1686 complex is capable of using NADPH as an electron donor for Fe(III)-NTA reduction, although at a slower rate. These findings, along with the predicted role for Dred_1685 and Dred_1686 in pyrimidine biosynthesis, calls into question whether this complex is physiologically relevant to metal reduction. However, because it was identified as the most active fraction from the insoluble (presumably membrane) protein pool, it should not be discounted. In fact, in the study where a fraction containing OmcB, a characterized *in vivo* soluble and insoluble iron reductase, was originally purified from the membrane of *G. sulfurreducens*, specific activity was

reported as 17.1 nmol Fe(II) formed/mg protein/min³². The specific activity of the insoluble/membrane fraction where Dred_1685–1686 was identified is >22.16 nmol Fe(II) formed/mg protein/min (**Table C.1**). This specific activity is grossly underestimated, as protein concentration was below detection but is clearly much lower than other fractions where concentration was also below detection (**Fig. C.3 and C.4**). The calculated specific activity of the Dred_1685–1686 complex following heterologous expression and purification is much higher, 627.68 nmol Fe(II) formed/mg protein/min (**Table C.3**).

In conclusion, our studies employing functional screens of fractions of the *D. reducens* proteome have uncovered metal and radionuclide reductases that are quite distinct from the multiheme c-type cytochromes described in Gram-negative iron reducers. Further studies combining proteomic and biochemical techniques are essential for better elucidation of key functional enzymes in the proteome of *D. reducens* and other poorly characterized organisms.

Methods and Materials

Culturing

Desulfotomaculum reducens MI-1 was obtained from ATCC and cultured anaerobically with an 80/20 N₂/CO₂ headspace at 30° C on Widdel Low Phosphate (WLP) media minus pyruvic acid¹⁵. Twenty mM sodium lactate (Fisher Scientific, Pittsburgh, PA USA) was added as electron donor with 25 mM Fe(III)-citrate (Santa Cruz Biotechnology, Inc., Dallas, TX USA) or 28 mM sodium sulfate (Fisher Scientific) as electron acceptor. Iron reduction activity assay.

Iron reduction activity assay

Iron reduction activity of crude extracts and protein fractions was determined and screened for using a 96-well plate ferrozine-based assay described previously²², where the reduction of Fe(III)-NTA with NADH as electron donor was monitored at 562 nm. The reaction mixture contained 160 μ L of assay buffer (40 mM MgCl₂ (Sigma-Aldrich, St. Louis, MO USA) 0.2 mM NADH (Thermo Fisher Scientific Across Organics, Pittsburgh, PA USA) and 0.5 mM Ferrozine[®] Iron Reagent (J.T. Baker/Avantor Performance Materials, Inc., Center Valley, PA USA) in 100 mM HEPES (EMD Chemicals, Inc., San Diego, CA USA) (pH 7.0) with 10% (v/v) glycerol (Sigma-Aldrich) and 30 μ L of sample. Ten μ L of 10mM Fe(III)-NTA (FeCl₃ X 6H₂O (Fisher Scientific), Nitrilotriacetic acid (Sigma-Aldrich), NaHCO₃(Fisher Scientific)) was added to commence the reaction. Absorbance of the ferrozine-Fe(II) complex was measured every 60 seconds over a 20 min reaction time in a Spectra MAX plus spectrophotometer (Molecular Devices LLC, Sunnyvale, CA USA). The assay was also implemented for confirmation of iron reduction activity in purified proteins following heterologous expression (Tecan Infinite 200 series microplate reader, Tecan Group Ltd, Männedorf, Switzerland), and an N₂ headspace was used. Reactions were incubated in this N₂ atmosphere for 7 min prior to Fe(III)-NTA injection.

Whole cell experiments

The capability for sulfate-grown *D. reducens* cells to reduce Fe(III) was tested. Late exponential phase *D. reducens* cells grown with sulfate and lactate were harvested anaerobically, washed 3 times with HEPES buffer (100 mM HEPES (EMD Chemicals), 40 mM MgCl₂ (Sigma-Aldrich), 10% (v/v) glycerol (Sigma-Aldrich), pH 7.0) and

resuspended in 3 mL of the buffer to a concentration of 3×10^9 cells/mL. Residual sulfide was quantified using the Cline Assay in order to take into account any potential abiotic Fe(III) reduction³³. Ten mM Fe(III)-NTA and 10 mM lactate was added to the cell suspension, and the accumulation of Fe(II) over time was monitored using the ferrozine assay³⁴.

Soluble and insoluble protein fraction preparation

The soluble and insoluble proteome was prepared with modifications to a previously described protocol³². Late exponential phase cells were harvested anaerobically at 4°C, washed, and resuspended in 5 mL of Tris-HCl extraction buffer (50 mM Tris-HCl (J.T. Baker/Avantor), 2 mM MgCl₂(Sigma-Aldrich) in 10% (v/v) glycerol (Sigma-Aldrich), pH 7) with protease inhibitor (cOmplete, Mini Protease Inhibitor Cocktail Tablets, Roche Applied Science, Indianapolis, IN USA). Following disruption with a French pressure cell at 8000 psi, unlysed cells were removed through centrifugation for 20 min at 7000g. Total protein extract in the supernatant was ultracentrifuged in a tabletop ultracentrifuge (Beckman Coulter, Brea, CA USA) at 100,000g for 60 min, the soluble fraction was removed to a separate tube, and the insoluble pellet was washed three times with Tris-HCl buffer and resuspended in 2 mL of Tris-HCl buffer with 0.5% wt/wt n-Dodecyl-β-D-maltoside (DDM) (Thermo Fisher Scientific Acros Organics). The insoluble protein fraction was extracted (solubilized) by stirring anaerobically at 4°C overnight and separated from unextracted protein by ultracentrifugation at 100,000g. Protein concentrations were quantified using the Bradford Assay (Thermo Scientific™ Pierce™ Coomassie (Bradford) Protein Assay, Fisher Scientific).

Strong anion exchange chromatography (SAX) separation

The soluble and extracted insoluble proteins were fractionated separately using strong anion exchange (SAX). SAX was performed on an Agilent 1100 Binary Solvent HPLC (Agilent Technologies, Inc., Wilmington, DE USA) using a Mono Q HR 5/5 column (GE Healthcare Bio-sciences, Pittsburgh, PA USA). All buffers were vacuum filtered through a 0.22 μm Durapore GV membrane (EMD Millipore Corporation, Billerica, MA USA) and stored at 4°C until use. A linear gradient (0-2-2.5-42-42.5-47.5-48-58 min, 0-0-5-50-75-75-0-0 % B) was employed using Buffer A (20 mM bis-tris (Sigma-Aldrich)/10% (w/v) glycerol (Fisher Scientific) pH = 6.9) and Buffer B (20 mM bis-Tris/1M sodium chloride (Fisher Scientific)/10% (w/v) glycerol pH = 6.9). The flow rate was set to 0.5 mL/min and 100 μL injections were performed. All samples were filtered through a Costar Spin-X 0.22 μm cellulose acetate centrifuge tube filter (Corning Incorporated, Corning, NY USA) prior to injection. Column effluent was monitored by UV absorbance at 280 nm. Manual fraction collection was performed at 1-min intervals beginning at 2 min and ending at 49 min post-injection for a total of 48 fractions. Fractions were stored on ice until the assay for iron reduction activity, and active fractions were selected for subsequent separation.

Size exclusion chromatography (SEC) separation

Fractions from the soluble protein fraction that retained activity after SAX were filtered through a Costar Spin-X 0.22 μm cellulose acetate centrifuge tube filter and concentrated using an Amicon Ultra 0.5 mL 10K MWCO Ultracel regenerated cellulose centrifugal filter (EMD Millipore) to a final volume of <100 μL . Concentrates were diluted to ~200 μL with SEC running buffer prior to injection. SEC fractionations were

carried out using a Dionex UltiMate 3000 HPLC (Dionex Corporation, Sunnyvale, CA USA) outfitted with the fraction collection option and operated in isocratic mode. A high-resolution aqueous SEC Yarra SEC-2000 column (3 μm , 4.6 X 250mm) with column-appropriate guard cartridges (Phenomenex, Inc., Torrance, CA USA) was used for sample fractionation. Column performance was checked periodically by injecting Aqueous SEC 1 Standard (Phenomenex). SEC running buffer contained 20 mM Tris-base (PlusOne, GE Healthcare Bio-sciences, Pittsburgh, PA USA), 2 mM MgCl_2 (Fisher Scientific), 150 mM NaCl (Fisher Scientific), and 10% (w/v) glycerol (Fisher Scientific) at pH = 6.8. Buffer was filtered as above and refrigerated prior to use. The maximum sample injection volume of 230 μL was used, the flow rate was set to 0.75 mL/min, and column effluent was monitored by dual wavelength UV absorbance at 230 nm and 280 nm. Fractions were collected in 0.5 mL 96-well microplates (Thermo Fisher Scientific Nunc A/S, Roskilde Denmark) at 15-second intervals beginning at 6 min and ending at 18 min and fractions were maintained at 4°C until the iron reduction activity assay. Active SEC fractions were selected for subsequent separation.

Native gel electrophoresis and in-gel activity assay

Active protein fractions selected following SAX or SEC separation were separated further with native gel electrophoresis using a discontinuous buffer system. For the native gel, the upper (cathode) buffer was 43 mM Tris-base (Fisher Scientific), 52 mM glycine (Fisher Scientific) adjusted to pH = 8.9 with hydrochloric acid (VWR International, West Chester, PA USA) in Milli-Q water (Millipore Corporation, Bedford, MA USA). The lower (anode) buffer was 120 mM Tris-base, 60 mM hydrochloric acid in Milli-Q water, pH = 8.1. The indicator running dye was

bromophenol blue (Bio-Rad, Hercules, CA USA) saturated in water. The electrophoresis apparatus consisted of a Novex Mini-cell XCell Sure Lock PAGE unit (Life Technologies, Carlsbad, CA USA) connected to a PowerPac 300 power supply (Bio-Rad). Precast Tris-glycine gradient mini-gels, Novex 4–12% 1.5mm x 10 well or Novex 8–16% 1.0mm x 10 well were purchased from Life Technologies. Novex NativeMark Unstained Protein Standard (Life Technologies, Carlsbad, CA USA) was used as the molecular weight standard. Active fractions from SAX or SEC preparative runs (38 μ L sample + 2 mL bromophenol blue solution) were loaded directly into the wells and 5 μ L of molecular weight standard was used. Electrophoresis was performed at ambient temperature under constant voltage of 50V for 10 min, to allow the proteins to enter the gel and salts to dissipate, followed by separation at 125V for ~2 hr or until the dye front reached the bottom of the gel cassette. The developed gels were removed from the cassette, rinsed briefly in deionized water, and then an in-gel iron reduction activity assay was subsequently performed, designed by modifying an existing protocol³⁵. Gels were submerged in the iron reduction activity assay buffer (described above) with 0.5 mM Fe(III)-NTA for 40 min. Protein bands with enzymes/enzyme complexes capable of Fe(III)-NTA reduction stained pink and were excised and transferred to a 0.6 mL microcentrifuge tube (low retention polypropylene, Fisher Scientific). Gel-fixing solution (200 mL) consisting of 50% methanol/7% glacial acetic acid (Fisher Scientific) in Milli-Q water was added to each gel slice followed by incubation at room temperature for a minimum of 45 min with occasional vortexing. The fixing solution was removed and gel storage solution (10% methanol/7% glacial acetic acid in Milli-Q water) was added to submerge the gel bands and then stored at

4°C until in-gel reduction/alkylation/digestion. To visualize banding patterns, gels were fixed as above, rinsed with deionized water and stained overnight in Invitrogen SYPRO Ruby protein gel stain (Life Technologies). Stained gels were destained following manufacturer's recommended protocol and gel images were captured by a Typhoon 9400 Variable Mode Imager (GE Healthcare).

Protein identification by GeLC-MS/MS analysis

In-gel digestion (using modified trypsin from Promega (Madison, WI)) and tryptic peptide extraction were performed following a protocol from Shevchenko *et al.* 1996³⁶ and modified as described by Zhang *et al.* 2003³⁷. All gel-extracted supernatants were combined and evaporated to dryness in a Speedvac SC110 (Thermo Savant, Milford, MA). Protein identification was carried out using nanoLC-MS/MS analysis with a Dionex UltiMate3000 system (Dionex, Sunnyvale, CA) and a hybrid triple quadrupole linear ion trap mass spectrometer, 4000 Q Trap from ABSciex (Framingham, MA). The gel-extracted peptides (5–10 µL) were injected onto a PepMap100 C18 trap column (5 µm, 100 Å, Dionex) at a flow rate of 20 µL/min for on-line desalting. They were then separated on a PepMap C18 RP nano column (3 µm, 75 µm x 15 cm, Dionex) and eluted in a 90-min gradient of 5% to 40% acetonitrile in 0.1% formic acid at 300 nL/min. The 4000 Q Trap was equipped with Micro Ion Spray ion source II. MS data acquisition was performed using Analyst 1.4.2 software (Applied Biosystems) in the positive ion mode for information dependant acquisition (IDA) analysis. The nanospray voltage was 1.6 kV for all experiments in positive ion mode. Nitrogen was used as the curtain (value of 10) and collision gas (set to high) with heated interface on. The declustering potential was set at 50 eV and Gas1 was 20 (arbitrary

unit). In IDA analysis, after each survey scan for m/z 400 to m/z 1550 and an enhanced resolution scan, the three highest intensity ions with multiple charge states were selected for tandem MS (MS/MS) with rolling collision energy applied for detected ions based on different charge states and m/z values. The exclusion time was set to 45 sec.

MS/MS data generated from LC/ESI-based IDA analysis was submitted to Mascot 2.3 for database searching using an in-house licensed Mascot local server and the search was performed using the *D. reducens* MI-1 protein database (downloaded from NCBI on September 20th, 2012 with 3276 entries) with one missed cleavage site by trypsin allowed. The peptide tolerance was set to 1.5 Da and MS/MS tolerance was set to 0.6 Da. Carbobamidomethyl modification of cysteine and a methionine oxidation were set as variable modifications. Peptides with significant scores, defined with >95% identity based on Mascot probability analysis, were considered (Mascot server, Matrix Science).

Heterologous expression of predicted iron reductases

Single protein heterologous expression

Locus tag Dred_2421, Dred_1685 and Dred_1686 from *D. reducens* MI-1 were amplified from genomic DNA by PCR and cloned into NdeI/XhoI, BamHI/SalI and BamHI/XhoI restriction sites of pET28a, respectively. The plasmids were transformed into 10G *Escherichia coli* cells selecting for kanamycin resistance. Based on colony PCR results, colonies containing the desired genes were selected, and plasmid DNA was isolated and sequenced using T7 primers. Sequence-confirmed plasmids were then transformed and expressed in BL-21 Rosetta cells. Cells were cultured at 37°C in 2 L of Luria Broth (LB) media (VWR) with 50 µg/mL kanamycin and 20µg/mL

chloramphenicol. At an OD₆₀₀ of 0.7, 200 µM IPTG was used to induce expression and cells were further incubated at 16°C for 24 hr. Cells were harvested at 8000 rpm for 5 min and the cell pellet was stored in 30 mL of lysis buffer (20 mM Tris pH 8.0, 5 mM imidazole, 500 mM NaCl, 2% (v/v) glycerol) at -80°C until use. Cells were lysed using a cell disruptor and lysate was centrifuged at 20,000 rpm for 30 min. The soluble fraction was loaded onto a column containing 2.4 ml of Ni-NTA agarose resin (Qiagen), as each target protein contained a N-terminus His₆ tag. The column was first washed with wash buffer (20 mM Tris pH 8.0, 30 mM imidazole, 500 mM NaCl) and then a linear gradient of 50–250 mM imidazole in wash buffer was used to elute the proteins. Fractions containing pure target protein were collected and the buffer was changed to 20 mM Tris pH 8.0, 150 mM NaCl using either dialysis or a desalting column (Econo-Pac, Bio-Rad).

Duet plasmid copurification

To co-express the predicted complex, Dred_1685 and Dred_1686 were cloned into BamHI/SalI and BglII/XhoI restriction sites in pETDuet vector, respectively. The co-expressed plasmid was transformed into 10G *Escherichia coli* cells selecting for ampicillin resistance. Based on colony PCR results, colonies containing the desired genes were selected and the plasmids were obtained and sequenced. The obtained plasmids were then transformed into BL-21 Rosetta cells for protein expression. Cells harboring the expression plasmid were cultured at 37°C in LB media with 100 µg/mL ampicillin and 20 µg/mL chloramphenicol. Induction, expression, and protein purification were performed as described above. In this expression construct, only Dred_1685 contained a N-terminus His₆ tag. Following affinity purification, the

Dred_1685–1686 complex was separated from excess Dred_1685 using size exclusion chromatography.

Cr(VI) reduction assay

Cr(VI) reduction was tested in anaerobic serum vials (N₂ headspace) with 2 mL reaction volumes containing 1 mM NADH (Thermo Fisher Scientific Acros Organics), 0.5 mM sodium dichromate (Alfa Aesar, Ward Hill, MA USA) and 1 μM in HEPES buffer. Following the 80 min timepoint, an additional 1 mM NADH was added in order to allow for complete reduction of the 0.5 mM Cr(VI) to presumably Cr(III). The disappearance of Cr(VI) was monitored at 540 nm using the diphenylcarbazide method³⁸. At each timepoint, the concentration of Cr(VI) in a reaction subsample was measured using an anaerobic plate reader (Tecan) at 540 nm. The reaction included 20 μL sample, 13 μL diphenylcarbazide solution (6 mM 1,5-diphenylcarbazide (Sigma-Aldrich) in acetone (Fisher-Scientific)), and 167 μL 0.12M H₂SO₄ (Fisher-Scientific).

U(VI) reduction assay

U(VI) reduction was tested in anaerobic serum vials (N₂ headspace) with 2 mL reaction volumes containing 1 mM NADH (Thermo Fisher Scientific Acros Organics), 0.5 mM uranyl acetate, (J.T. Baker/Avantor Performance Materials) and 10 μM protein in HEPES buffer. The disappearance of U(VI) was monitored over time with the reagent Arsenazo (III) based on an updated Arsenazo protocol³⁹. At each timepoint, the concentration of U(VI) in a reaction subsample was measured using an anaerobic plate reader (Tecan) at 651 nm. The reaction included 8 μL of sample, 8 μL DTPA solution (2.5% diethylenetriaminepenta-acetic acid (Sigma-Aldrich)), 4 μL 10% L-tartaric acid (Sigma-Aldrich), 4 μL Arsenazo Solution (3.2 mM Arsenazo-III (Sigma-Aldrich), 0.5

N NaOH (Sigma-Aldrich)), and 176 μL of dilute H_2SO_4 (Fisher-Scientific) (pH 2). U(VI) oxidation experiments were performed following reduction of U(VI) and anaerobic incubation overnight. Following bubbling with 150 mL ambient air and aerobic incubation for 5 hr, U(VI) concentration was measured.

REFERENCE

1. Weber, K. A., Achenbach, L. A. & Coates, J. D. Microorganisms pumping iron: anaerobic microbial iron oxidation and reduction. *Nat. Rev.* **4**, 752–764 (2006).
2. Mohapatra, B. R., Dinardo, O., Gould, W. D. & Koren, D. W. Biochemical and genomic facets on the dissimilatory reduction of radionuclides by microorganisms - A review. *Minerals Engineering* **23**, 591–599 (2010).
3. Bird, L. J., Bonnefoy, V. & Newman, D. K. Bioenergetic challenges of microbial iron metabolisms. *Trends in Microbiology* **19**, 330–340 (2011).
4. Wall, J. D. & Krumholz, L. R. Uranium Reduction. *Annu. Rev. Microbiol.* **60**, 149–166 (2006).
5. Shi, L. *et al.* The roles of outer membrane cytochromes of *Shewanella* and *Geobacter* in extracellular electron transfer. *Environmental Microbiology Reports* **1**, 220–227 (2009).
6. Sharma, S., Cavallaro, G. & Rosato, A. A systematic investigation of multiheme c-type cytochromes in prokaryotes. *J. Biol. Inorg. Chem.* **15**, 559–571 (2010).
7. Petrie, L., North, N. N., Dollhopf, S. L., Balkwill, D. L. & Kostka, J. E. Enumeration and characterization of iron (III)-reducing microbial communities from acidic subsurface sediments contaminated with uranium (VI). *Appl. Environ. Microbiol.* **69**, 7467–7479 (2003).
8. Suzuki, Y., Kelly, S. D., Kemner, K. M. & Banfield, J. F. Microbial populations stimulated for hexavalent uranium reduction in uranium mine sediment. *Appl. Environ. Microbiol.* **69**, 1337–1346 (2003).
9. Cardenas, E. *et al.* A combined massively parallel sequencing - indicator species approach revealed significant association between sulfate-reducing bacteria and uranium-reducing microbial communities. *Appl. Environ. Microbiol.* **76**, 6778–6786 (2010).
10. Williamson, A. J. *et al.* Microbial reduction of Fe(III) under alkaline conditions relevant to geological disposal. *Appl. Environ. Microbiol.* **79**, 3320–3326 (2013).
11. Newsome, L., Morris, K. & Lloyd, J. R. The biogeochemistry and bioremediation of uranium and other priority radionuclides. *Chemical Geology* **363**, 164–184 (2014).
12. Carlson, H. K. *et al.* Surface multiheme c-type cytochromes from *Thermincola potens* and implications for respiratory metal reduction by Gram-positive bacteria. *Proc. Natl. Acad. Sci.* **109**, 1702–1707 (2012).
13. Gavrilov, S. N., Lloyd, J. R., Kostrikina, N. A. & Slobodkin, A. I. Fe(III) Oxide Reduction by a Gram-positive Thermophile: Physiological Mechanisms for Dissimilatory Reduction of Poorly Crystalline Fe(III) Oxide by a Thermophilic Gram-positive Bacterium *Carboxydothemus ferrireducens*. *Geomicrobiol. J.* **29**, 804–819 (2012).
14. Tebo, B. M. & Obraztsova, A. Y. Sulfate-reducing bacterium grows with Cr(VI), U(VI), Mn(IV), and Fe(III) as electron acceptors. *FEMS Microbiol. Lett.* **162**, 193–198 (1998).

15. Junier, P. *et al.* Metal reduction by spores of *Desulfotomaculum reducens*. *Environ. Microbiol.* **11**, 3007–3017 (2009).
16. Dalla Vecchia, E., Suvorova, E. I., Maillard, J. & Bernier-Latmani, R. Fe(III) reduction during pyruvate fermentation by *Desulfotomaculum reducens* strain MI-1. *Geobiology* **12**, 48–61 (2014).
17. Junier, P. *et al.* The genome of the Gram-positive metal- and sulfate-reducing bacterium *Desulfotomaculum reducens* strain MI-1. *Environ. Microbiol.* **12**, 2738–2754 (2010).
18. Junier, P., Vecchia, E. D. & Bernier-Latmani, R. The response of *desulfotomaculum reducens* MI-1 to U(VI) exposure: A transcriptomic study. *Geomicrobiol. J.* **28**, 483–496 (2011).
19. Suzuki, Y., Kelly, S. D., Kemner, K. M. & Banfield, J. F. Enzymatic U(VI) reduction by *Desulfosporosinus* species. *Radiochim. Acta* **92**, 11–16 (2004).
20. Kim, S. H. *et al.* Genome sequence of *Desulfitobacterium hafniense* DCB-2, a Gram-positive anaerobe capable of dehalogenation and metal reduction. *BMC Microbiol.* **12**, (2012).
21. MAGNUSON, T. S. *et al.* Isolation, characterization and gene sequence analysis of a membrane-associated 89 kDa Fe(III) reducing cytochrome c from *Geobacter sulfurreducens*. *Biochem. J.* **359**, 147 (2001).
22. Dwayne A. Elias Feng Yang Heather M. Mottaz Alexander S. Beliaev Mary. Enrichment of functional redox reactive proteins and identification by mass spectrometry results in several terminal Fe(III)-reducing candidate proteins in *Shewanella oneidensis* MR-1. *J. Microbiol. Methods* **68**, 367–375 (2007).
23. Williams, R. E. & Bruce, N. C. ‘New uses for an old enzyme’ - The Old Yellow Enzyme family of flavoenzymes. *Microbiology* **148**, 1607–1614 (2002).
24. Fontecave, M., Covès, J. & Pierre, J. L. Ferric reductases or flavin reductases? *Biometals* **7**, 3–8 (1994).
25. Vadas, A., Monbouquette, H. G., Johnson, E. & Schröder, I. Identification and characterization of a novel ferric reductase from the hyperthermophilic Archaeon *Archaeoglobus fulgidus*. *J. Biol. Chem.* **274**, 36715–36721 (1999).
26. Mazoch, J., Tesařík, R., Sedláček, V., Kučera, I. & Turánek, J. Isolation and biochemical characterization of two soluble iron(III) reductases from *Paracoccus denitrificans*. *Eur. J. Biochem.* **271**, 553–562 (2004).
27. Hubbard, P. a, Liang, X., Schulz, H. & Kim, J.-J. P. The crystal structure and reaction mechanism of *Escherichia coli* 2,4-dienoyl-CoA reductase. *J. Biol. Chem.* **278**, 37553–37560 (2003).
28. Yu, N. Y. *et al.* PSORTb 3.0: Improved protein subcellular localization prediction with refined localization subcategories and predictive capabilities for all prokaryotes. *Bioinformatics* **26**, 1608–1615 (2010).
29. Lovley, D. R., Roden, E. E., Phillips, E. J. P. & Woodward, J. C. Enzymatic iron and uranium reduction by sulfate-reducing bacteria. *Mar. Geol.* **113**, 41–53 (1993).
30. Nielsen, F. S., Andersen, P. S. & Jensen, K. F. The B form of dihydroorotate dehydrogenase from *Lactococcus lactis* consists of two different subunits, encoded by the *pyrDb* and *pyrK* genes, and contains FMN, FAD, and [FeS]

- redox centers. *J. Biol. Chem.* **271**, 29359–29365 (1996).
31. Norager, S., Jensen, K. F., Björnberg, O. & Larsen, S. E. coli dihydroorotate dehydrogenase reveals structural and functional distinctions between different classes of dihydroorotate dehydrogenases. *Structure* **10**, 1211–1223 (2002).
 32. Magnuson, T. S., Hodges-myerson, A. L. & Lovley, D. R. Characterization of a membrane-bound NADH-dependent Fe³⁺ reductase from the dissimilatory Fe³⁺-reducing bacterium *Geobacter sulfurreducens*. *FEMS Microbiol. Lett.* **185**, (2000).
 33. Strocchi, A., Furne, J. K. & Levitt, M. D. A modification of the methylene blue method to measure bacterial sulfide production in feces. *J. Microbiol. Methods* **15**, 75–82 (1992).
 34. Lovley, D. R. & Phillips, E. J. P. Rapid assay for microbially reducible ferric iron in aquatic sediments. *Appl. Environ. Microbiol.* **53**, 1536–1540 (1987).
 35. Gaspard, S., Vazquez, F. & Holliger, C. Localization and solubilization of the iron(III) reductase of *Geobacter sulfurreducens*. *Appl. Environ. Microbiol.* **64**, 3188–3194 (1998).
 36. Shevchenko, A., Wilm, M., Vorm, O. & Mann, M. Mass Spectrometric Sequencing of Proteins from Silver-Stained Polyacrylamide Gels Mass Spectrometric Sequencing of Proteins from Silver-Stained Polyacrylamide Gels. *Anal. Chem.* **68**, 850–858 (1996).
 37. Zhang, S., Van Pelt, C. K. & Henion, J. D. Automated chip-based nanoelectrospray-mass spectrometry for rapid identification of proteins separated by two-dimensional gel electrophoresis. *Electrophoresis* **24**, 3620–3632 (2003).
 38. Urone, P. F. Stability of Colorimetric Reagent for Chromium, s-Diphenylcarbazide, in Various Solvents. *Anal. Chem.* **27**, 1354–1355 (1955).
 39. Golmohammadi, H., Rashidi, A. & Safdari, S. J. Simple and rapid spectrophotometric method for determination of uranium (vi) in low grade uranium ores using arsenazo (III). *Chem. Chem. Technol.* **6**, 245–249 (2012).

**JOHN WILEY AND SONS LICENSE
TERMS AND CONDITIONS**

Jun 26, 2018

This Agreement between Ms. Ornella Nelson ("You") and John Wiley and Sons ("John Wiley and Sons") consists of your license details and the terms and conditions provided by John Wiley and Sons and Copyright Clearance Center.

License Number	4376580338363
License date	Jun 26, 2018
Licensed Content Publisher	John Wiley and Sons
Licensed Content Publication	Environmental Microbiology
Licensed Content Title	Identification of proteins capable of metal reduction from the proteome of the Gram-positive bacterium <i>Desulfotomaculum reducens</i> MI-1 using an NADH-based activity assay
Licensed Content Author	Anne Elyse Otwell, Robert W. Sherwood, Sheng Zhang, et al
Licensed Content Date	Jan 27, 2015
Licensed Content Volume	17
Licensed Content Issue	6
Licensed Content Pages	14
Type of use	Dissertation/Thesis
Requestor type	Author of this Wiley article
Format	Print and electronic
Portion	Full article
Will you be translating?	No
Title of your thesis / dissertation	A Chemoproteomic Technique for the Identification of Proteins Regulated by Coenzyme A
Expected completion date	Dec 2018
Expected size (number of pages)	150
Requestor Location	Ms. Ornella Nelson 259 East Ave, Baker lab ITHACA, NY 14853 United States Attn: Ms. Ornella Nelson
Publisher Tax ID	EU26007151
Total	0.00 USD